COMPTON CAMERA IMAGING AND THE CONE TRANSFORM

A Dissertation

by

FATMA TERZIOGLU

Submitted to the Office of Graduate and Professional Studies of
Texas A&M University
in partial fulfillment of the requirements for the degree of

DOCTOR OF PHILOSOPHY

Chair of Committee,	Peter Kuchment
Committee Members,	Raytcho Lazarov
	Raffaella Righetti
	William Rundell
Head of Department,	Emil Straube

May 2018

Major Subject: Mathematics

ABSTRACT

In this dissertation, we focus on analytic and numerical inversion of an integral transform (*cone* or *Compton* transform) that maps a function to its integrals over conical surfaces with a weight equal to some power of the distance from the cone's vertex. It arises in various imaging techniques, most prominently, in modeling of the data provided by the so-called Compton camera, which has novel applications in various fields, including biomedical and industrial imaging, homeland security, and gamma ray astronomy.

In the case of pure surface measure on the cone, an integral identity relating cone, Radon and cosine transforms is presented, which enables us to derive an inversion formula for the cone transform in any dimension. The image reconstruction algorithms, based on the inversion formulas, and their numerical implementation results in dimensions two and three are provided. In 3D, the implementation of the inversion algorithms is challenging due to the high dimensionality of the forward data, and the fact that the application of a fourth order differential operator on the unit sphere to a singular integral is required. We thus develop and apply three different inversion algorithms and study their feasibility.

The weighted divergent beam transform, which integrates a function over rays with a weight equal to some power of the distance to the starting point (source) of the ray, is closely intertwined with the weighted cone transform. We study it in some details, which leads eventually to other weighted cone transform inversions. The image reconstruction algorithm, based on one of the inversion formulas, and its numerical implementation results for various weight factors in dimensions two and three are also provided.

All inversion formulas presented in this dissertation are applicable for a wide variety of detector geometries in any dimension.

To my brilliant and loving husband Tevfik Terzioglu, and my precious son Ekin Ozan who has been a constant source of happiness and joy since the day he came into my life

ACKNOWLEDGMENTS

First and the foremost, I would like to express my deepest gratitude to my advisor Dist. Prof. Peter Kuchment, for all his encouragement, patience and constant support during my graduate studies. This dissertation would have never been possible without his invaluable guidance, help and inspiration. I feel very lucky to have him as my advisor, and cannot say enough to thank him for always being there for me.

I would like to express my sincere gratitude to Professors Raytcho Lazarov, Raffaella Righetti and William Rundell for serving in my dissertation committee.

I am grateful to Prof. Andrea Bonito for numerous discussions and suggestions concerning numerical implementation of some of the algorithms in this dissertation as well as for his excellent instruction of partial differential equations courses. I also thank the Numerical Analysis and Scientific Computing group for letting me use their computing resources.

I thank Prof. Boris Rubin for many useful comments and written materials provided.

I thank Prof. Dean Baskin for his wonderful lectures on microlocal analysis.

I would like to thank the faculty and staff at the Mathematics Department of Texas A&M University for providing an effective yet enjoyable learning environment. Special thanks go to Prof. Peter Howard for being an excellent graduate advisor.

I would like to express my gratitude to all my teachers who put their faith in me and urged me to do better.

I am thankful to all my friends and colleagues in College Station who have been with me all these years and made my experience here an enjoyable and memorable one.

Special thanks go to my best friend and dear husband Tevfik Terzioglu who always believed in me and has been a constant source of support and encouragement during the

challenges of graduate school and life.

I would like to express my heartfelt gratitude to my parents, Habibe and Ibrahim Yilmaz, and my sister Nursah Yilmaz. None of this would have been possible without their unconditional love and continuous support.

Finally, I acknowledge the financial support provided by the Department of Mathematics and the National Science Foundation through the grant DMS 1211463.

CONTRIBUTORS AND FUNDING SOURCES

Contributors

This work was supervised by a dissertation committee consisting of Professors Peter Kuchment, Raytcho Lazarov and William Rundell of the Department of Mathematics and Professor Raffaella Righetti of the Department of Electrical and Computer Engineering.

All work for the dissertation was completed by the student, in collaboration with Professor Peter Kuchment of the Department of Mathematics.

Funding Sources

Graduate study was supported by Texas A&M University Department of Mathematics in the form of teaching assistantship. This work was partially supported by the National Science Foundation through the grant DMS 1211463.

TABLE OF CONTENTS

Page

ABSTRACT ii

DEDICATION iii

ACKNOWLEDGMENTS iv

CONTRIBUTORS AND FUNDING SOURCES vi

TABLE OF CONTENTS vii

LIST OF FIGURES ix

LIST OF TABLES xiii

1. INTRODUCTION 1

2. ORIGINS AND SOME APPLICATIONS OF THE CONE TRANSFORM . . . 5

2.1 Optical Tomography and Broken Ray Transform 5
2.2 Compton Camera Imaging 6

3. SOME INVERSION FORMULAS FOR THE CONE TRANSFORM 8

3.1 The Cone Transform 8
3.2 Inversion of the Cone Transform 11
3.3 An Alternative Inversion Formula 15
3.4 Other Inversion Formulas 18
3.5 Reconstructions in Dimension Two 21
3.6 Reconstructions in Dimension Three 24
3.6.1 Method 1: Reconstruction Using Spherical Harmonics Expansions 24
3.6.2 Method 2: Reconstruction by Direct Implementation of Theorem 3.4.5 29
3.6.3 Method 3: Reconstruction via a Mollified Inversion of the Cosine Transform 32
3.6.4 Comparison of the Three Methods 34

4. INVERSION OF WEIGHTED DIVERGENT BEAM AND CONE TRANSFORMS 40

4.1 The Weighted Cone and Divergent Beam Transforms 40
4.2 Inversion of the Weighted Divergent Beam Transform 43
4.3 Inversion of the Weighted Cone Transform 48
4.4 Relations with the Radon Transform: Other Inversion Formulas 51
4.5 Reconstruction Algorithms and Numerical Implementation Results 54
4.5.1 2D Image Reconstruction from Weighted Cone Data 56
4.5.2 3D Image Reconstruction from Weighted Cone Data 60
4.5.3 3D Image Reconstruction from Weighted Divergent Beam Data . 64

5. FURTHER PROPERTIES OF THE WEIGHTED CONE TRANSFORM 67

5.1 Spherical Harmonic Expansions 67
5.2 A Range Condition 71
5.3 Dual Operator 73
5.4 A Microlocal Property 74

6. CONCLUSION AND REMARKS 78

REFERENCES 80

APPENDIX A. AN ALTERNATIVE PROOF OF THEOREM 3.3.1 87

APPENDIX B. SOME SPECIAL FUNCTIONS, OPERATORS AND INTEGRAL TRANSFORMS 100

B.1 Special Functions 100
B.1.1 The Gamma Function 100
B.1.2 Gegenbauer Poynomials 101
B.1.3 Spherical Harmonics 101
B.2 The Radon Transform 103
B.3 Funk, Sine and Cosine Transforms 105

LIST OF FIGURES

FIGURE Page

2.1 Left: Collimation. Right: Compton Scattering. 6

2.2 Schematic representation of a Compton camera. 7

3.1 A Cone in 2-dimensions. 10

3.2 Left: The phantom is the characteristic function of a circle having density 1 unit, radius 0.5 unit and centered at $(0, 0)$. Right: 256x256 image reconstructed from the simulated Compton data using 257 detectors per side and 200 counts for the angles β and ψ each (see Fig. 3.1). 23

3.3 Left: The phantom is the sum of the characteristic functions of two intersecting circles having densities 0.3 and 0.7 units, radii 0.5 and 0.3 units, and centered at $(0, 0)$ and $(0.5, 0)$. Right: 256x256 image reconstructed from the simulated Compton data using 257 detectors per side and 200 counts for the angles β and ψ each (see Fig. 3.1). 23

3.4 The analytically computed Radon transform of the phantom (shown in red) vs. its reconstruction from the Compton data using (3.28). The reconstructions shown correspond to three different mesh sizes: the number of points on the sphere being 1806, 7446, and 30054, from left to right. 29

3.5 The Radon transform of the phantom recovered using (3.21) and (3.29). The reconstructions shown corresponds to three different mesh sizes: the number of points on the sphere being 1806, 7446, and 30054, from left to right. 32

3.6 The Radon transform of the phantom using the method of mollified inverse for the cosine transform. The reconstructions shown corresponds to three different mesh sizes: the number of points on the sphere being 1806, 7446, and 30054, from left to right. 34

3.7 Comparison of the three reconstruction methods. The cross-sections by the coordinate planes are shown. (a) The phantom is the characteristic function of 3d ball having radius 0.5 and center at the origin. (b) Reconstruction via Method 1. (c) Reconstruction via Method 2. (d) Reconstruction via Method 3. 36

3.8 x-profiles of the phantom and the reconstructions in Figure 3.7, (a) method 1, (b) method 2 and (c) method 3. 37

3.9 Comparison of the three reconstruction methods. The cross-sections by the coordinate planes are shown. (a) The phantom is the characteristic function of 3d ball having radius 0.5 and center at the origin. (b) Reconstruction via Method 1 from data contaminated with 20% Gaussian white noise. (c) Reconstruction via Method 2 from data contaminated with 10% Gaussian white noise. (d) Reconstruction via Method 3 from noisy data contaminated with 20% Gaussian white noise. 38

3.10 Comparison of x-profiles of central slices of phantom and the reconstructions from noisy data shown in Figure 3.9. 39

4.1 A cone with vertex $u \in \mathbb{R}^n$, central axis direction vector $\beta \in \mathbb{S}^{n-1}$ and opening angle $\psi \in (0, \pi)$. 41

4.2 The density plot (left) and surface plot (right) of the phantom f that consists of two concentric disks centered at $(0, 0.4)$ with radii 0.25 and 0.5, and densities 1 and -0.5 units, respectively. 57

4.3 The density plot of 256×256 image reconstructed from the simulated cone data using 256 counts for vertices u (represented by white dots on the unit circle), 400 counts for directions β and 90 counts for opening angles ψ (left), and the comparison of y-axis profiles of the phantom and the reconstruction (right). 57

4.4 The density plot of 256×256 image reconstructed from cone data contaminated with 5% Gaussian noise (left), and the comparison of y-axis profiles of the phantom and the reconstruction (right). The dimensions of the cone data are taken as in Fig. 4.3. 58

4.5 The density plot of 256×256 image reconstructed from the simulated cone data using 256 counts for vertices u (represented by white dots around the square), 400 counts for directions β and 90 counts for opening angles ψ (left), and the comparison of y-axis profiles of the phantom and the reconstruction (right). 59

4.6 The density plot of 256×256 image reconstructed from cone data contaminated with 5% Gaussian noise (left), and the comparison of y-axis profiles of the phantom and the reconstruction (right). The dimensions of the cone data are taken as in Fig. 4.5. 59

4.7 Comparison of the profiles of the reconstruction along the diagonal of the square region for the circular (left) and square (right) locations of the vertices (detectors). 60

4.8 The 3D ball phantom with radius 0.5, center (0,0,0.25) and unit density (left), and 90×90 image reconstructed via (4.30) from weighted cone data simulated using 1800 counts for vertices u on the unit sphere, 1800 counts for directions β and 200 counts for opening angles ψ (right). The cross sections by the planes $x = 0, y = 0$ and $z = 0.25$ are shown. 61

4.9 Comparison of the x-axis (left), y-axis (center) and z-axis (right) profiles of the reconstruction and the phantom given in Fig. 4.8. 62

4.10 The 3D ball phantom with radius 0.5, center (0,0,0.25) and unit density (left), and 90×90 image reconstructed via (4.31) from weighted cone data simulated using 1800 counts for vertices u on the unit sphere, 1800 counts for directions β and 200 counts for opening angles ψ (right). The cross sections by the planes $x = 0, y = 0$ and $z = 0.25$ are shown. 62

4.11 Comparison of the x-axis (left), y-axis (center) and z-axis (right) profiles of the reconstruction and the phantom given in Fig. 4.10. 63

4.12 The 3D ball phantom with radius 0.5, center (0,0,0.25) and unit density (left), and 90×90 image reconstructed via (4.31) from weighted cone data contaminated with 5% Gaussian white noise (right). The dimensions of the cone projections are taken as in Fig. 4.10. The cross sections by the planes $x = 0, y = 0$ and $z = 0.25$ are shown. 63

4.13 Comparison of the x-axis (left), y-axis (center) and z-axis (right) profiles of the reconstruction and the phantom given in Fig. 4.12. 64

4.14 The 3D ball phantom with radius 0.5, center (0,0,0.25) and unit density (left), and 90×90 image reconstructed via (4.32) from weighted divergent beam data simulated using 1800 counts for sources u on the unit sphere and 30K counts for unit directions σ (right). The cross sections by the planes $x = 0, y = 0$ and $z = 0.25$ are shown. 65

4.15 Comparison of the x-axis (left), y-axis (center) and z-axis (right) profiles of the phantom and the reconstruction given in Fig. 4.14. 65

4.16 The 3D ball phantom with radius 0.5, center (0,0,0.25) and unit density (left), and 90×90 image reconstructed via (4.33) from weighted divergent beam data simulated using 1800 counts for sources u on the unit sphere and 30K counts for unit directions σ (right). The cross sections by the planes $x = 0, y = 0$ and $z = 0.25$ are shown. 66

4.17 Comparison of the x-axis (left), y-axis (center) and z-axis (right) profiles of the reconstruction and the phantom given in Fig. 4.16. 66

A.1 Geometry of Lemma A.0.4. 91

LIST OF TABLES

TABLE Page

3.1 The normalized L^2 and H^1 errors for the Radon data for each of the three methods. 35

1. INTRODUCTION[1]

In this dissertation, we focus on analytic and numerical inversion of an integral transform (*cone* or *Compton* transform) that maps a function to its integrals over conical surfaces with a weight equal to some power of the distance from the cone's[2] vertex. It arises in various imaging techniques, most prominently in modeling of the data provided by the so-called Compton camera, which has novel applications in various fields including medical and industrial imaging, homeland security, and gamma ray astronomy [1, 6, 9, 48, 56, 65]. In Compton camera setting, the vertices of the cones correspond to the locations of the detection sites on the scattering detector. More information on the working principle of a Compton camera can be found in Section 2.2.

Several works, e.g. [2, 3, 6, 8, 11, 18, 21, 27, 47, 57, 62, and references therein], concentrated on the case of pure surface measure on the cone. Probably, the first known analytical reconstruction formula in 3D was given in [8], where the authors considered only the cones having central axis orthogonal to detector plane. The papers [6, 30] contain spherical harmonics expansion solutions. Another inversion formula for cone transforms on cones having fixed central axis and variable opening angle is provided in [47]. The paper [57] presents two reconstruction methods for two Compton data models. Inversion formulas using the full set of Compton projections are presented in [42, 43]. Inversion formulas for n-dimensional cone transform over the cones having central axis orthogonal

[1]Portions of this chapter have been adapted from:

[2]The word "cone" in this text always means a surface, rather than solid cone.

to detector plane are provided in [20, 24]. All these works only addressed the cones with the vertex on the scattering detector. Inversion algorithms for various 2D cone transforms are given in [2–4, 6, 11, 18, 21, 27–29, 34, 35, 44, 54, 61, 62].

The problem of inverting the cone transform is over-determined (e.g. the space of cones in 3D with vertices on a detector surface is five-dimensional, three-dimensional in 2D. Without the restriction on the vertex, the dimensions are correspondingly six and four.) One thus is tempted to restrict the set of cones, in order to get a non-over-determined problem (e.g. [2, 3, 6, 8, 18, 21, 24, 27, 30, 31, 47, 57, 62, and references therein]). In most of these considerations only a subset of cones with vertex at a given scattering detector is used. This means that most of the information already collected by the Compton camera is discarded. However, when the signals are weak (e.g. in homeland security applications [1]), restricting the data would lead to essential elimination of the signal. We thus intend to use the over-determined data coming from all cones with vertices on the scattering detector. This improves the stability, but makes the problem more complicated due to the high dimensionality.

In the Compton camera imaging applications mentioned above, the vertex of the cone is located on the detector plane, while in other applications vertices are not restricted, although some other conditions might be imposed on the cones. We thus find it useful to understand first analytic properties of a more general cone transform, where no restriction on the vertex location or parameters of the cone is imposed. This is the transform addressed in this text with the hope that it can be useful for more restricted versions. As our reconstructions in Chapters 3 and 4 show, this hope does materialize, as one indeed arrives at flexible applications to the Compton imaging [37, 60].

It has been mentioned in various papers, e.g. [6, 43, 57] that, depending upon the engineering of the detector, various power weights can appear in the surface integral. However, more work needs to be done to determine the weight factor that accurately represents the

projections obtained from a Compton camera. Here, we consider a weight that is equal to some power of the distance to the vertex (detection site), which covers all weights arising in various works. An alternative inversion formula for such transform assuming that the vertices of the cones are located on a given straight line is provided in [31]. A reconstruction formula for such transform defined on the cones having vertices on a hyperplane and a central axis orthogonal to this hyperplane is derived in [24]. In comparison, the formulas we derive allow for a wide variety of cone vertex (a.k.a. detector, or source) geometries, which do not allow for harmonic analysis, but satisfy what we call in this paper Tuy's condition (Definition 4.2.3).

A closely intertwined with the weighted cone transform is what is called *weighted divergent beam transform*, which integrates a function over rays with a weight equal to some power of the distance to the starting point (source) of the ray. When the weight factor is not present, this is the well studied and important for the 3D X-ray CT divergent (or cone) beam transform (see e.g. [16, 22, 25, 32, 33, 58, 63, 64, and references therein]). We study it in some details, which eventually leads to the desired weighted cone transform inversions [38].

In order to avoid being distracted from the main purpose of this text, we assume that the functions in question belong to the Schwartz space $\mathcal{S}$ of smooth fast decaying functions. This allows us to skip discussions of applicability of various transforms. However, as in the case of Radon transform (see, e.g. [36, 46]), the results have a much wider area of applicability, since the derived formulas can be extended by continuity (although we do not do this in the current text) to some wider functional spaces. This is confirmed, in particular, by our successful numerical implementations for discontinuous (piecewise continuous) phantoms. The issues of appropriate functional spaces will be addressed elsewhere.

We also adopt the standard abuse of notations, writing the action of a distribution T on a test function φ, $\langle T, \varphi \rangle$, as $\int T(x)\varphi(x)dx$.

The dissertation is organized as follows. In Chapter 2, origins and some applications of the cone transform are discussed. In Chapter 3, the cone transform in the case of the pure surface measure on the cone is considered, and various inversion formulas for the full data cone transform in $\mathbb{R}^n$ are derived. The formulas are applicable for a wide variety of detector geometries in any dimension. The results of numerical simulations in dimensions two and three are also provided. In Chapter 4, the weighted cone transform, mapping a function to its integrals over conical surfaces with a weight equal to an integer power of the distance from the cone's vertex, is considered. The relations between the Radon and the weighted divergent beam and cone transforms are investigated, and novel inversion formulas in $\mathbb{R}^n$ are derived for the latter two. The formulas are applicable for a wide variety of detector geometries in any dimension. The image reconstruction algorithm based on one of the inversion formulas and its numerical implementation results for various weight factors in dimensions two and three are also provided. Chapter 5 contains some further properties of the (weighted) cone transform. Conclusions and remarks can be found in Chapter 6. Appendix A contains an alternative proof of a relation between cone, Radon and cosine transforms that is instrumental in deriving an inversion formula for the cone transform in Chapter 3. In Appendix B, we collect some facts about well known special functions, operators and integral transforms including Radon, Funk, sine and cosine transforms.

2. ORIGINS AND SOME APPLICATIONS OF THE CONE TRANSFORM

2.1 Optical Tomography and Broken Ray Transform

Optical tomography is an important biomedical imaging technique that is used to determine the optical properties of a medium of interest [5]. In a typical experiment, a light source and an array of detectors are placed around the medium, the light illuminated from the source propagates through the medium, and is collected by the detectors. The inverse problem of optical tomography is to reconstruct the optical parameters (absorption and scattering coefficients) of the medium of interest from boundary measurements [53].

When the medium of interest is of intermediate thickness (varying between the size of a molecule and micrometers), the propagation of light in the medium is modeled by the radiative transport equation. The first-order scattering approximation to the radiative transport equation enables the derivation of a relationship between the extinction coefficient (the sum of absorption and scattering coefficients) of the medium and the single-scattered light intensity, which is referred to as single-scattering optical tomography (SSOT) [12]. The path of a single-scattered photon consists of two rays with a common vertex, which is called a broken ray. Thus, the measured data is related to the integrals of the extinction coefficient over broken rays, which is called the *broken ray transform* (BRT). It is also called *V-line Radon transform* in the literature, and it corresponds to two-dimensional cone transform (see (3.4) and Fig. 3.1).

Inversion of broken ray transform allows the recovery of the scattering and absorption coefficients of the radiative transport equation in the single scattering regime, and thus enable image reconstruction in SSOT [12]. The interested reader is referred to the pioneering works [10–12] for a thorough explanation of the physics of SSOT. More results on BRT can be found in [2–4, 27–29, 34, 35, 44, 54, 61, 62, and references therein].

2.2 Compton Camera Imaging[1]

The conventional gamma cameras used in medical Single Photon Emission Computed Tomography (SPECT) imaging determine the direction of an incoming γ-photon by "collimating" the detector (see Fig. 2.1(left)). This considerably decreases the efficiency, because only a small portion of the incoming γ-rays passes through the collimator [6]. Thus, the acquired signal is weak and statistically noisy. The situation is similar in astronomy and even more severe in homeland security applications [1, 36, 48, 65].

On the other hand, Compton cameras utilize Compton scattering (see Fig. 2.1(right)) and use electronic rather than mechanical collimation to provide simultaneous multiple views of the object and dramatic increase in sensitivity [56].

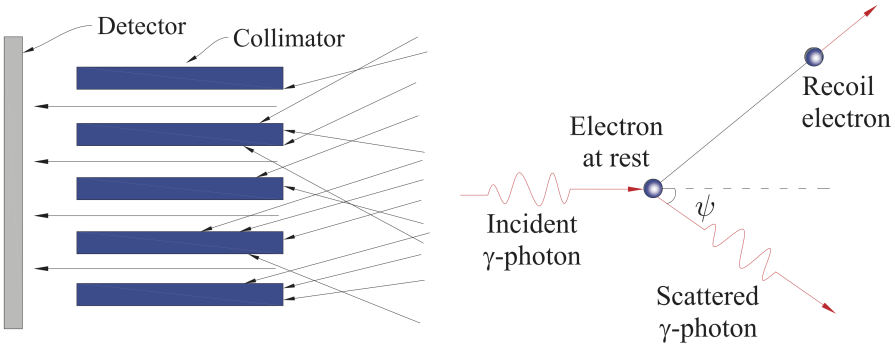

Figure 2.1: Left: Collimation. Right: Compton Scattering.

A Compton camera consists of two parallel detectors (see Fig. 2.2). When the photon hits the first detector, where its position u and energy E_1 are recorded, it undergoes Compton scattering. Then, it is absorbed in the second detector where its position v and energy

[1]Portions of this section have been adapted from: Some inversion formulas for the cone transform, by F. Terzioglu, Inverse Problems, Volume 31, 2015, Copyright © by IOP Publishing Ltd. Reprinted with the permission of IOP Publishing Ltd.

E_2 are again measured. The scattering angle ψ and a unit vector β are calculated from the data as follows (see e.g. [9]):

$$\cos\psi = 1 - \frac{mc^2 E_1}{(E_1 + E_2)E_2} \qquad \beta = \frac{u - v}{|u - v|}. \tag{2.1}$$

Here, m is the mass of the electron and c is the speed of light.

From the knowledge of the scattering angle ψ and the vector β, we conclude that the photon originated from the surface of the cone with central axis β, vertex u and opening angle ψ (see Fig. 2.2). Therefore, although the exact incoming direction of the detected particle is not available, one knows a surface cone of such possible directions. One can argue that the data provided by Compton camera are integrals of the distribution of the radiation sources over conical surfaces having vertex at the detector. The operator that maps source intensity distribution function $f(x)$ to its integrals over these cones is called the *cone* or *Compton transform*. The goal of Compton camera imaging is to recover the source distribution from this data [1].

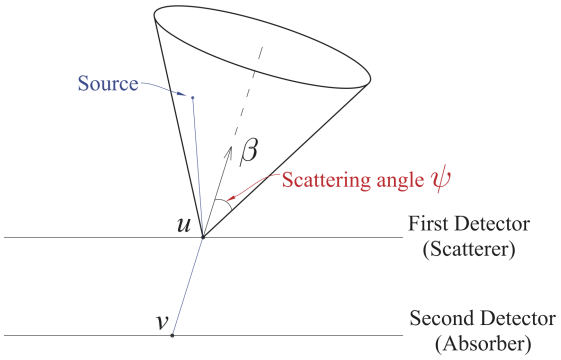

Figure 2.2: Schematic representation of a Compton camera.

3. SOME INVERSION FORMULAS FOR THE CONE TRANSFORM[1]

In this chapter, we focus on the case of the pure surface measure on the cone and derive various inversion formulas[2] for the full data cone transform in $\mathbb{R}^n$. In Section 3.2, we obtain an integral relation between the cone and Radon transforms in $\mathbb{R}^n$ and deduce from it an inversion formula for the cone transform. In Section 3.3, we provide a different inversion formula derived from another integral relation between the cone and Radon transforms in $\mathbb{R}^n$. Both of these formulas require the vertices of the cones to be available throughout the whole space, which is clearly impossible in Compton imaging, although is suitable for SSOT. However, the integral relation provided in Section 3.3 also enables us to associate the cone transform with the cosine transform, and through this relation, we obtain the Radon transform explicitly in terms of the cone transform, which leads in turn to a variety of inversion algorithms from Compton data in Section 3.4. The results of numerical simulations in dimension two are provided in Section 3.5. Section 3.6 contains several procedures that convert the cone data to Radon data of the same function and the results of numerical implementation of these approaches in dimension three.

3.1 The Cone Transform

A round cone in $\mathbb{R}^n$ can be parametrized by a tuple (u, β, ψ), where $u \in \mathbb{R}^n$ is the cone vertex, vector $\beta \in \mathbb{S}^{n-1}$ is directed along the cone's central axis, and $\psi \in (0, \pi)$ is the

[1]Portions of this chapter have been adapted from:

[2]The reader should recall that it is common to have a variety of different inversion formulas for Radon type transforms, which are all the same for perfect data, but react differently to unavoidable errors in data [36, 46]. Having such a variety is even more important when dealing with overdetermined data, as in Compton imaging.

opening angle of the cone (see Fig. 2.2). Then, a point $x \in \mathbb{R}^n$ lies on the cone iff

$$(x-u)\cdot\beta = |x-u|\cos\psi. \tag{3.1}$$

The *n-dimensional cone transform* C maps a function f into the set of its integrals over the circular cones in $\mathbb{R}^n$. Explicitly,

$$Cf(u,\beta,\psi) = \int\limits_{(x-u)\cdot\beta=|x-u|\cos\psi} f(x)dx \tag{3.2}$$

where dx is the surface measure on the cone.

The *n-dimensional vertical cone transform* maps a function f into the set of its integrals over the cones having central axis parallel to the x_n-axis, and thus the vector β is equal to $e_n = (0,...,0,1) \in \mathbb{R}^n$. It can be written in terms of the spherical coordinates. Namely,

$$Cf(u,e_n,\psi) = \int\limits_0^\infty \int\limits_{\mathbb{S}^{n-2}} f(u+\rho((\sin\psi)\omega,\cos\psi))(\rho\sin\psi)^{n-2}d\omega d\rho. \tag{3.3}$$

In two dimensions, the equation (3.1) describes two rays with a common vertex (see Fig. 3.1). A cone in two dimensions can be parametrized by a point $u \in \mathbb{R}^2$ that serves as its vertex, an opening angle $\psi \in (0,\pi)$ and a vector $\beta = \beta(\phi) = (\sin\phi,\cos\phi) \in \mathbb{S}^1$ directed along the central axis.

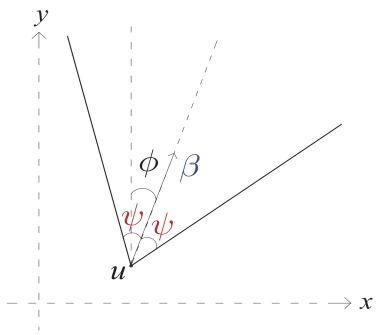

Figure 3.1: A Cone in 2-dimensions.

Then, the 2D cone transform of a function $f \in \mathcal{S}(\mathbb{R}^2)$ is given by

$$\begin{aligned} Cf(u,\beta,\psi) = Cf(u,\beta(\phi),\psi) = &\int_0^\infty f(u + r(\sin(\psi+\phi),\cos(\psi+\phi)))dr \\ &+ \int_0^\infty f(u + r(-\sin(\psi-\phi),\cos(\psi-\phi)))dr. \end{aligned} \tag{3.4}$$

As a straightforward calculation shows, analogously to the Radon transform, cone transform has an evenness property, and is shift and rotation invariant:

Lemma 3.1.1. *Let $f \in \mathcal{S}(\mathbb{R}^n)$, $u \in \mathbb{R}^n$, $\beta \in \mathbb{S}^{n-1}$ and $\psi \in (0,\pi)$. Then,*

1.

$$Cf(u,-\beta,\psi) = Cf(u,\beta,\pi-\psi). \tag{3.5}$$

2. *Let T_a be the translation operator in $\mathbb{R}^n$, defined as $T_a f(x) = f(x+a)$ for $a \in \mathbb{R}^n$. We define*

$$T_a(Cf)(u,\beta,\psi) := Cf(u+a,\beta,\psi).$$

Then,

$$T_a C = C T_a.$$

3. *Let A be an $n \times n$ rotation matrix and $M_A f(x) = f(Ax)$ be the corresponding rotation operator. We define*

$$M_A(Cf)(u, \beta, \psi) := Cf(Au, A\beta, \psi).$$

Then,

$$M_A C = C M_A.$$

3.2 Inversion of the Cone Transform

In the following, we investigate the relation between the cone and Radon transforms and provide various analytic inversion formulas for the n-dimensional cone transform.

Theorem 3.2.1. *Let $f \in \mathcal{S}(\mathbb{R}^n)$. Then,*

1. *For any $u \in \mathbb{R}^n$ and $\beta \in \mathbb{S}^{n-1}$, we have*

$$\int_0^\pi Cf(u, \beta, \psi) d\psi = \frac{\Gamma(\frac{n-1}{2})}{2\pi^{(n-1)/2}} \int_{\mathbb{S}^{n-1}} Rf(\omega, u \cdot \omega) d\omega = \frac{\Gamma(\frac{n-1}{2})}{2\pi^{(n-1)/2}} R^{\#} Rf(u), \quad (3.6)$$

where $R^{\#}$, the dual operator to the Radon transform, is defined in Section B.2.

2. *Let a function $\mu : \mathbb{S}^{n-1} \to \mathbb{R}$ be such that $\int_{\mathbb{S}^{n-1}} \mu(\beta) d\beta = 1$. Then,*

$$f(x) = \frac{\pi^{-n/2} \Gamma(\frac{n}{2})}{2\Gamma(n-1)} \int_{\mathbb{S}^{n-1}} \int_0^\pi I_{u \to x}^{1-n} Cf(u, \beta, \psi) \mu(\beta) d\psi d\beta, \quad (3.7)$$

where I^α is the Riesz potential defined in Section B.2.

Remark 3.2.2.

1. One notices that according to (3.6), the inversion formula (3.7) consists of a back-projecting of the cone data, followed by a filtration (i.e., is what is called a FBP type formula).

2. One can choose $\mu(\beta)$ to be equal to a delta-function, which would eliminate integration with respect to β in (3.7). However, if the signal is very week, eliminating almost all values of β would lead to elimination of the signal. Thus weighted integration with respect to β allows for accounting for all data collected.

Proof. We first prove the theorem for dimensions $n \geq 3$.

$$\int_0^\pi Cf(u, e_n, \psi)d\psi = \int_0^\pi \int_0^\infty \int_{\mathbb{S}^{n-2}} f(u + \rho((\sin\psi)\omega, \cos\psi))(\rho\sin\psi)^{n-2}d\omega d\rho d\psi$$

$$= \int_{\mathbb{S}^{n-1}} \int_0^\infty f(u + \rho\sigma)\rho^{n-2}d\rho d\sigma = \int_{\mathbb{R}^n} f(u + x)|x|^{-1}dx = \frac{1}{|\mathbb{S}^{n-2}|}R^\# Rf(u),$$

The last equality is due to [46, Chapter 2, Theorem 1.5] (see also (A.3)). As both R and $R^\#$ commute with rigid motions in $\mathbb{R}^n$, we obtain for any $\beta \in \mathbb{S}^{n-1}$,

$$\int_0^\pi Cf(u, \beta, \psi)d\psi = \frac{1}{|\mathbb{S}^{n-2}|}R^\# Rf(u).$$

Thus, for any function μ on S^{n-1} such that $\int_{\mathbb{S}^{n-1}} \mu(\beta)d\beta = 1$, we have

$$\int_{\mathbb{S}^{n-1}} \int_0^\pi Cf(u, \beta, \psi)\mu(\beta)d\psi d\beta = \frac{1}{|\mathbb{S}^{n-2}|}R^\# Rf(u) = \frac{\Gamma(\frac{n-1}{2})}{2\pi^{(n-1)/2}}R^\# Rf(u).$$

Note that the last equality follows from the area formula for the n-sphere, that is

$$|S^{n-1}| = \frac{2\pi^{n/2}}{\Gamma(\frac{n}{2})}. \tag{3.8}$$

Using (B.16) with $\alpha = n-1$, and utilizing the gamma-function duplication formula (see B.1.1)

$$\Gamma(z)\Gamma(z+\frac{1}{2}) = 2^{1-2z}\sqrt{\pi}\Gamma(2z), \tag{3.9}$$

we conclude that

$$f(u) = \frac{\pi^{n/2}\Gamma(\frac{n}{2})}{2\Gamma(n-1)} \int\limits_{\mathbb{S}^{n-1}} \int\limits_{0}^{\pi} I_{u\to x}^{1-n} Cf(u,\beta,\psi)\mu(\beta)d\psi d\beta.$$

For the 2-dimensional case, we only need to provide the proof of (3.6), since the rest of the proof stays the same. Assume for now that $u = 0$. By definition of the 2D cone transform, we have

$$\begin{aligned}\int\limits_0^{\pi} Cf(0,\beta(\phi),\psi)d\psi = &\int\limits_0^{\pi}\int\limits_0^{\infty} f(r\sin(\psi+\phi), r\cos(\psi+\phi))drd\psi \\ &+ \int\limits_0^{\pi}\int\limits_0^{\infty} f(-r\sin(\psi-\phi), r\cos(\psi-\phi))drd\psi.\end{aligned}$$

Changing variables, we obtain

$$\int\limits_0^{\pi} f(r\sin(\psi+\phi), r\cos(\psi+\phi))d\psi = \int\limits_{\phi}^{\pi+\phi} f(r\sin\psi, r\cos\psi)d\psi,$$

and

$$\int_0^{\pi} f(-r\sin(\psi-\phi), r\cos(\psi-\phi))d\psi = \int_{-\pi+\phi}^{\phi} f(r\sin\psi, r\cos\psi)d\psi.$$

Thus,

$$\int_0^{\pi} Cf(0,\beta(\phi),\psi)d\psi = \int_0^{\infty}\int_{-\pi+\phi}^{\pi+\phi} f(r\sin\psi, r\cos\psi)d\psi dr.$$

Changing variables by letting $\theta = \dfrac{\pi}{2} - \psi$ and using 2π-periodicity of sine and cosine functions, we get

$$\int_{-\pi+\phi}^{\pi+\phi} f(r\sin\psi, r\cos\psi)d\psi = \int_{-\frac{\pi}{2}-\phi}^{\frac{3\pi}{2}-\phi} f(r\cos\theta, r\sin\theta)d\theta = \int_0^{2\pi} f(r\cos\theta, r\sin\theta)d\theta.$$

Therefore,

$$\int_0^{\pi} Cf(0,\beta(\phi),\psi)d\psi = \int_0^{2\pi}\int_0^{\infty} f(r\cos\theta, r\sin\theta)drd\theta = \frac{1}{2}\int_0^{2\pi} Rf(\theta,0)d\theta,$$

where the last equality follows by letting $n = 2$ and $p = 0$ in (A.2). Now, using the shift invariance of both cone and Radon transforms, we conclude that

$$\int_0^{\pi} Cf(u,\beta,\psi)d\psi = \frac{1}{2}\int_{\mathbb{S}^1} Rf(\omega, u\cdot\omega)d\omega = \frac{1}{2}R^{\#}Rf(u),$$

which is (3.6) with $n = 2$, so we are done. □

Corollary 3.2.3. *For $n = 3$, the formula* (3.7) *becomes*

$$f(u) = -\frac{1}{4\pi}\int_{\mathbb{S}^{n-1}}\int_0^{\pi} \Delta Cf(u,\beta,\psi)\mu(\beta)d\psi d\beta,$$

where the Laplace operator Δ acts in the variable u.

3.3 An Alternative Inversion Formula

For the derivation of an alternative inversion formula, we need the following relation between the cone and Radon transforms.

Theorem 3.3.1. *Let $f \in \mathcal{S}(\mathbb{R}^n)$. For any $u \in \mathbb{R}^n$ and $\beta \in \mathbb{S}^{n-1}$, we have*

$$\frac{1}{\pi}\int_0^\pi Cf(u,\beta,\psi)\sin\psi d\psi = \frac{1}{|\mathbb{S}^{n-1}|}\int_{\mathbb{S}^{n-1}} Rf(\omega,\omega\cdot u)|\omega\cdot\beta|d\omega = \mathfrak{C}(R(T_u f))(\beta), \quad (3.10)$$

where $|\mathbb{S}^{n-1}|$ denotes the area of the sphere $\mathbb{S}^{n-1}$ and $\mathfrak{C}$ is the cosine transform whose definition is given in (B.26).

Proof. We first observe that if $D_u f(\sigma) := \int_0^\infty f(u+\rho\sigma)\rho^{n-2}d\rho$, then

$$F(D_u f)(\omega) = \int_{\mathbb{S}^{n-1}} D_u f(\sigma)\delta(\omega\cdot\sigma)d\sigma = Rf(\omega, u\cdot\omega), \quad (3.11)$$

where F denotes the Funk transform (see (B.21)). Indeed,

$$\begin{aligned} F(D_u f)(\omega) &= \int_{\mathbb{S}^{n-1}} D_u f(\sigma)\delta(\omega\cdot\sigma)d\sigma \\ &= \int_{\mathbb{S}^{n-1}}\int_0^\infty f(u+\rho\sigma)\rho^{n-2}d\rho\delta(\omega\cdot\sigma)d\sigma \\ &= \int_{\mathbb{S}^{n-1}}\int_0^\infty f(u+\rho\sigma)\delta(\omega\cdot\rho\sigma)\rho^{n-1}d\rho d\sigma \\ &= \int_{\mathbb{R}^n} f(x)\delta(\omega\cdot(x-u))dx = Rf(\omega,u\cdot\omega). \end{aligned}$$

It is known that $\mathcal{S} = \frac{\pi}{|\mathbb{S}^{n-1}|}\mathfrak{C}F$ where $\mathcal{S}, \mathfrak{C}$ and F are the sine, cosine and Funk transforms, respectively (see Appendix B.3 and [52, p. 284, (5.1.17)]). Applying cosine transform and multiplying with $\frac{\pi}{|\mathbb{S}^{n-1}|}$ in both sides of (3.11), we obtain

$$\mathcal{S}(D_u f) = \frac{\pi}{|\mathbb{S}^{n-1}|}\mathfrak{C}F(D_u f) = \frac{\pi}{|\mathbb{S}^{n-1}|}\mathfrak{C}(R(T_u f)).$$

That is,

$$\int_{\mathbb{S}^{n-1}} D_u f(\sigma)(1-(\beta\cdot\sigma)^2)^{1/2} d\sigma = \frac{\pi}{|\mathbb{S}^{n-1}|}\int_{\mathbb{S}^{n-1}} Rf(\omega, u\cdot\omega)|\beta\cdot\omega| d\omega. \tag{3.12}$$

It remains to show that

$$\int_{\mathbb{S}^{n-1}} D_u f(\sigma)(1-(\beta\cdot\sigma)^2)^{1/2} d\sigma = \int_0^{\pi} Cf(u,\beta,\psi)\sin\psi d\psi. \tag{3.13}$$

Since all $\mathcal{S}, \mathfrak{C}, D$ and R commute with rotations, it suffices to take $\beta = e_n$.

$$\begin{aligned}
\int_{\mathbb{S}^{n-1}} D_u f(\sigma)(1-(e_n\cdot\sigma)^2)^{1/2} d\sigma &= \int_{\mathbb{S}^{n-2}}\int_0^{\pi} D_u f((\sin\psi)\omega, \cos\psi)(\sin\psi)^{n-1} d\psi d\omega \\
&= \int_0^{\pi}\int_{\mathbb{S}^{n-2}}\int_0^{\infty} f(u+\rho(\sin\psi)\omega, \cos\psi))(\rho\sin\psi)^{n-2} d\rho d\omega \sin\psi d\psi \\
&= \int_0^{\pi} Cf(u, e_n, \psi)\sin\psi d\psi.
\end{aligned}$$

□

An alternative proof of Theorem 3.3.1 is given in Appendix A.

The equality (3.10) enables us to invert the cone transform by utilizing the inversion formulas for the Radon transform.

Theorem 3.3.2. *Let $f \in \mathcal{S}(\mathbb{R}^n)$. For any $u \in \mathbb{R}^n$, we have*

$$f(x) = \frac{\Gamma^2(\frac{n+1}{2})}{2\pi^n \Gamma(n)} \int\limits_{\mathbb{S}^{n-1}} \int\limits_0^\pi I_{u\to x}^{1-n} Cf(u,\beta,\psi) \sin\psi d\psi d\beta. \tag{3.14}$$

Proof. Integrating both sides of (3.10) with respect to β over S^{n-1}, we obtain

$$\int\limits_{\mathbb{S}^{n-1}} \int\limits_0^\pi Cf(u,\beta,\psi) \sin\psi d\psi d\beta = \frac{\pi}{|S^{n-1}|} \int\limits_{\mathbb{S}^{n-1}} Rf(\omega, \omega\cdot u) \int\limits_{\mathbb{S}^{n-1}} |\omega\cdot\beta| d\beta d\omega.$$

Using the rotation invariance of the Lebesgue measure on the sphere, for any $\omega \in \mathbb{S}^{n-1}$, we compute

$$\int\limits_{\mathbb{S}^{n-1}} |\omega\cdot\beta| d\beta = \int\limits_{\mathbb{S}^{n-2}} \int\limits_0^\pi |\cos\phi| (\sin\phi)^{n-2} d\phi d\theta = \frac{2|\mathbb{S}^{n-2}|}{n-1}.$$

Thus, we get

$$\begin{aligned} \int\limits_{\mathbb{S}^{n-1}} \int\limits_0^\pi Cf(u,\beta,\psi) \sin\psi d\psi d\beta &= \frac{\pi}{|S^{n-1}|} \frac{2|\mathbb{S}^{n-2}|}{n-1} \int\limits_{\mathbb{S}^{n-1}} Rf(\omega,\omega\cdot u) d\omega \\ &= \frac{2\pi}{n-1} \frac{|\mathbb{S}^{n-2}|}{|S^{n-1}|} \int\limits_{\mathbb{S}^{n-1}} R^\# Rf(u) = \frac{\pi\Gamma(n)}{2^{n-1}\Gamma^2(\frac{n+1}{2})} R^\# Rf(u). \end{aligned} \tag{3.15}$$

Note that, for the evaluation of the constant, we have used the area formula for the n-sphere, (3.8) and the duplication formula (3.9). Now, using formula (B.16) with $\alpha = n-1$, we obtain the result. □

Corollary 3.3.3. *For $n = 3$, the formula* (3.14) *reads as*

$$f(u) = \frac{-1}{4\pi^3} \int\limits_{\mathbb{S}^{n-1}} \int\limits_0^\pi \Delta Cf(u,\beta,\psi) \sin\psi d\psi d\beta,$$

where the Laplacian Δ acts in the variable u.

3.4 Other Inversion Formulas

The main goal of this section is to derive a formula that is applicable in Compton imaging (i.e., only uses the cone vertices located outside the object). The cosine transform is a continuous bijection of $C^{\infty}_{even}(S^{n-1})$ to itself (see e.g. [14], [52]). Since, for any $f \in \mathcal{S}(\mathbb{R}^n)$, $Rf(\omega, 0)$ is an even function in $C^{\infty}(S^{n-1})$, we can recover the function $R(T_u f)$ explicitly for all $u \in \mathbb{R}^n$ by inverting the cosine transform according to the Theorem B.3.5.

Theorem 3.4.1. *Let $f \in \mathcal{S}(\mathbb{R}^n)$. For any $u \in \mathbb{R}^n$ and $\omega \in \mathbb{S}^{n-1}$, if n is even,*

$$Rf(\omega, \omega \cdot u) = \frac{-2^{n-1}}{\Gamma(n-1)} \int_0^{\pi} P_{n/2}(\Delta_{\mathbb{S}}) F(Cf)(u, \omega, \psi) \sin\psi d\psi, \tag{3.16}$$

and if n is odd,

$$\begin{aligned} Rf(\omega, \omega \cdot u) = {} & \frac{\Gamma(\frac{n+1}{2})}{\pi^{(n+1)/2}} \int_{\mathbb{S}^{n-1}} \int_0^{\pi} Cf(u, \beta, \psi) \sin\psi d\psi d\beta \\ & - \frac{2\pi^{-n/2}}{\Gamma(\frac{n}{2})} P_{(n+1)/2}(\Delta_{\mathbb{S}}) \left\{ \int_{\mathbb{S}^{n-1}} \int_0^{\pi} Cf(u, \beta, \psi) \log \frac{1}{|\omega \cdot \beta|} \sin\psi d\psi d\beta \right\}, \end{aligned} \tag{3.17}$$

where F is the Funk transform (B.21) *and the operator $P_r(\Delta_{\mathbb{S}})$ is given in Theorem B.3.5, both of them acting in the spherical variable ω.*

Proof. The result follows by applying inverse cosine transform (B.27) and (B.28) to equality (3.10). □

This result, in particular, answers the question of what geometries of Compton detectors are sufficient for (stable) reconstruction of the function f. Indeed, formulas (3.17) and (3.16) show that it is sufficient to have for any $\omega \in \mathbb{S}^{n-1}$ and $s \in \mathbb{R}$ a detector location u such that $\omega \cdot u = s$. This can be rephrased in a nice geometric way:

Definition 3.4.2 (*Compton Admissibility Condition*)**.** We will call an array of Compton detectors *admissible* (for a given region of space), if any hyperplane intersecting this region, intersects a detection site of the scattering detector.

So, if a set U of detectors is admissible for a region $D \in \mathbb{R}^n$, then the formulas (3.17) and (3.16) enable one to reconstruct the Radon transform of any function f supported inside D, and thus f itself.

Here is a useful example of an application of the admissibility:

Proposition 3.4.3. *Suppose that $n = 3$ and the detectors are placed on a sphere S_r of radius r. We assume that the region for placing the object to be imaged is the concentric sphere $S_{r'}$ of radius $r' = r - \delta$ for some $\delta > 0$. Then, any curve U on S_r that satisfies the condition below is admissible:*

$$\textit{Any circle on } S_r \textit{ of radius } \rho \geq \sqrt{\delta(2r - \delta)} \textit{ intersects } U.$$

Proof. Indeed, every plane intersecting the interior of the sphere $S_{r'}$ intersect S_r over a circle of radius $\rho \geq \sqrt{\delta(2r - \delta)}$ and thus contains at least one detector. □

Remark 3.4.4.

1. The experience of Radon transform shows that uniqueness of reconstruction should hold for some non-admissible sets of detectors as well, although some (“invisible") sharp details will get blurred in the reconstruction (see, e.g. [36, Ch. 7]). The corresponding microlocal analysis of this issue will be done elsewhere.

2. The admissibility condition is not the minimal one. For instance, in the situation of Proposition 3.4.3, the set of Compton data will still be 4-dimensional, and thus somewhat overdetermined.

3. In the cases of low signal-to-noise ratio (e.g. SPECT and especially homeland security imaging), one would prefer to use larger admissible sets of detectors (e.g. 2D rather than 1D arrays considered in Proposition 3.4.3), which would allow introducing additional (weighted, if needed) averaging, in order to reduce the effects of the noise.

4. As it has been mentioned before, for all the reconstruction algorithms we develop in this text, the geometry of detectors is irrelevant, as long as it satisfies the generous Admissibility Condition 3.4.2 in section 2. If this condition is violated, one can still use the algorithms, but then familiar limited data blurring artifacts [36, 46] will appear.

A different approach to recovery of the Radon data from the Compton data comes from the following known relation (see [19]) between the cosine and Funk transforms:

$$(\Delta_{\mathbb{S}} + n - 1)\mathfrak{C} = F, \tag{3.18}$$

where $\Delta_{\mathbb{S}}$ is the Laplace-Beltrami operator on the unit sphere.

Indeed, applying $(\Delta_{\mathbb{S}} + n - 1)$ to (3.10), we obtain

$$\Phi(u, \beta) := F(R(T_u f))(\beta) = \frac{(\Delta_{\mathbb{S}} + n - 1)}{\pi} \int_0^{\pi} Cf(u, \beta, \psi) \sin \psi d\psi, \tag{3.19}$$

where $\Delta_{\mathbb{S}}$ acts in variable β.

We now use the inversion formula for the Funk transform given in Theorem B.3.3 (see also [52, Chapter 5, Theorem 5.37]), whose application to (3.19) leads to the following result.

Theorem 3.4.5. *Let $f \in \mathcal{S}(\mathbb{R}^n)$, $n \geq 3$. For any $u \in \mathbb{R}^n$ and $\omega \in \mathbb{S}^{n-1}$,*

$$Rf(\omega, \omega \cdot u) = \frac{\Gamma(n/2)}{2\pi^{n/2}} \int\limits_{\mathbb{S}^{n-1}} \Phi(u, \beta) d\beta + \frac{2^{n-1}}{(n-2)!} Q(\Delta_{\mathbb{S}}) \left\{ \int\limits_{\mathbb{S}^{n-1}} \Phi(u, \beta) \log \frac{1}{|\omega \cdot \beta|} d\beta \right\}, \tag{3.20}$$

where

$$Q(\Delta_{\mathbb{S}}) = 4^{(1-n)/2} \prod_{k=0}^{(n-3)/2} \left[-\Delta_{\mathbb{S}} + (2k+1)(n-3-2k) \right].$$

In particular, in 3D one arrives to

Corollary 3.4.6. *For any $u \in \mathbb{R}^3$ and $\omega \in S^2$,*

$$Rf(\omega, \omega \cdot u) = \frac{1}{4\pi} \int\limits_{\mathbb{S}^2} \Phi(u, \beta) d\beta - \frac{\Delta_{\mathbb{S}}}{2\pi} \left\{ \int\limits_{\mathbb{S}^2} \Phi(u, \beta) \log \frac{1}{|\omega \cdot \beta|} d\beta \right\}. \tag{3.21}$$

3.5 Reconstructions in Dimension Two

In 2D, for $\omega = (\cos\theta, \sin\theta)$, $\Delta_S = \dfrac{\partial^2}{\partial\theta^2}$. Then the formula (3.16) reads as

$$Rf(\omega, \omega \cdot u) = \frac{1}{2} \left(\frac{\partial^2}{\partial\theta^2} + 1 \right) \int\limits_0^{\pi} Cf(u, \omega^{\perp}, \psi) \sin\psi d\psi. \tag{3.22}$$

We applied this approach to some 2D examples. Figures 3.2 and 3.3 show the reconstructions of some phantoms from their projections collected by four Compton cameras placed along the sides of a square. We simulate analytically the Compton projection data of the phantoms and then use formula (3.16) to convert them to Radon projections. Finally, the filtered back-projection is applied to invert the Radon transform and obtain the reconstructions.

ALGORITHM Numerical Implementation of (3.22)

Data: $c_{i,j,k} = Cf(u_i, \theta_j, \psi_k)$, $i = 1, ..., U$, $j = 1, ..., T$, $k = 1, ..., P$.

1: For $i = 1, ..., U$, $j = 1, ..., T$ compute

$$G(u_i, \theta_j) := \sum_{k=1}^{P} c_{i,j+T/2,k} \sin \psi_k \Delta\psi \sim \int_0^{\pi} Cf(u, \omega(\theta)^{\perp}, \psi) \sin \psi d\psi.$$

2: For $i = 1, ..., U$, $j = 1, ..., T$, differentiate $G(u_i, \theta_j)$ with respect to θ twice using finite difference method.

3: For $i = 1, ..., U$, $j = 1, ..., T$ compute

$$Rf(\omega_j, \omega_j \cdot u_i) = \frac{1}{2}(\frac{\partial^2}{\partial\theta^2} + 1)G(u_i, \theta_j).$$

4: Carry out 1D interpolation to obtain $Rf(\omega_j, s_k)$ for a uniform mesh $\{s_k\}$ on $[-1, 1]$.

5: Apply filtered backprojection algorithm for the Radon transform to obtain $f_{i,j}$ from $Rf(\omega_j, s_k)$ where i, j runs over the reconstruction grid $[-1, 1]^2$.

Result: $f_{i,j}$ is an approximation to the phantom f which is supported on the unit circle.

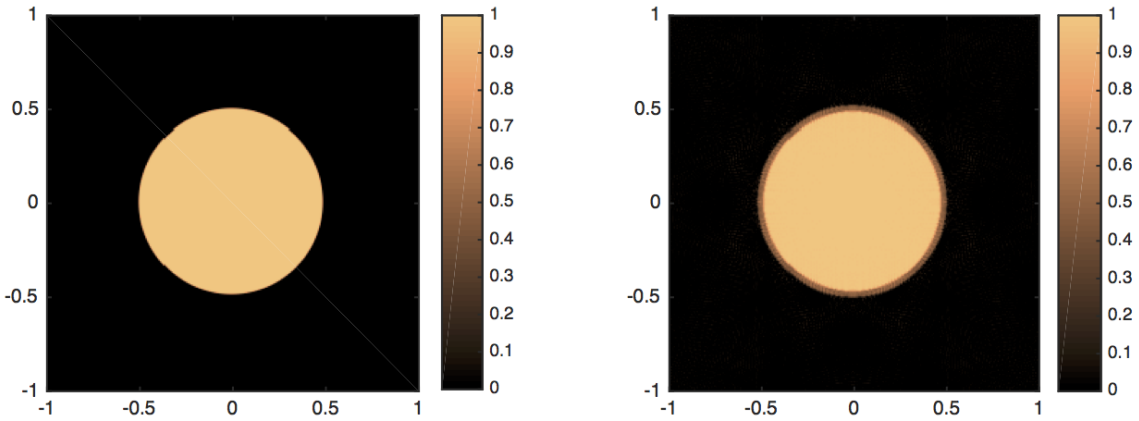

Figure 3.2: Left: The phantom is the characteristic function of a circle having density 1 unit, radius 0.5 unit and centered at $(0, 0)$. Right: 256x256 image reconstructed from the simulated Compton data using 257 detectors per side and 200 counts for the angles β and ψ each (see Fig. 3.1).

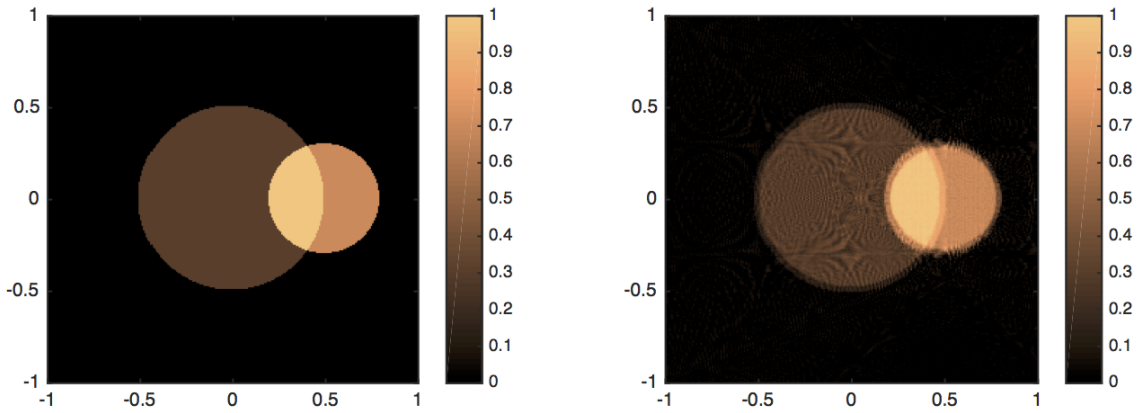

Figure 3.3: Left: The phantom is the sum of the characteristic functions of two intersecting circles having densities 0.3 and 0.7 units, radii 0.5 and 0.3 units, and centered at $(0, 0)$ and $(0.5, 0)$. Right: 256x256 image reconstructed from the simulated Compton data using 257 detectors per side and 200 counts for the angles β and ψ each (see Fig. 3.1).

3.6 Reconstructions in Dimension Three

In this section, we address the numerical implementation in the 3-dimensional case, where we develop and apply three different inversion algorithms and study their feasibility.

Our first attempt has been to implement numerically the inversion formula (3.17) from Theorem 3.4.1. The results were discouraging. The reason for this failure was that (3.17) requires numerical computation of some singular integrals, followed then by applying to the results a fourth order differential operator on the sphere.

Thus we had to resort to different inversion techniques, the description of which one finds below.

In all examples below, the two-layer detectors cover the unit sphere $\mathbb{S}^2$ in $\mathbb{R}^3$ and the object is located inside of this sphere and at some positive distance from it[3]. The algorithm given in [50] is used to generate the triangular mesh on $\mathbb{S}^2$. The forward simulations of Compton camera data were done numerically rather than analytically and thus involved errors, which is in fact better for checking the validity and stability of the reconstruction algorithms.

3.6.1 Method 1: Reconstruction Using Spherical Harmonics Expansions

In this section, we derive a series formula that recovers the Radon data from cone data. Let us introduce the function

$$G(u,\beta) := \int_0^\pi Cf(u,\beta,\psi)\sin\psi d\psi.$$

[3]The spherical geometry of the detector and of most of the phantoms we consider does not constitute any inverse crime. This particular geometry is used to reduce immense computations of the synthetic *forward* data, which run for a long time even on multi-core machines. The inversion algorithms are not aware of the symmetry of the detectors and/or phantoms.

For each fixed detector location $u \in \mathbb{R}^n$, we can expand the function $G(u, \beta)$ of $\beta \in \mathbb{S}^{n-1}$ into spherical harmonics Y_l^m (see Appendix B.1.3):

$$G(u, \beta) = \sum_{l=0}^{\infty} \sum_{m=1}^{N(n,l)} g_l^m(u) Y_l^m(\beta), \tag{3.23}$$

where

$$g_l^m(u) = \int_{\mathbb{S}^{n-1}} G(u, \beta) \overline{Y_l^m(\beta)} d\beta$$

and

$$N(n, l) = (n + 2l - 2) \frac{(n + l - 3)!}{l!(n - 2)!}$$

(see e.g. [6, 45, 59]). Using (3.17), one obtains the following series inversion formula:

Theorem 3.6.1. *For any $u \in \mathbb{R}^n$ and $\omega \in \mathbb{S}^{n-1}$,*

$$Rf(\omega, \omega \cdot u) = \frac{\Gamma(\frac{n+1}{2})}{\pi^{n/2}} g_0^1(u) - \frac{2\pi^{-n/2}}{\Gamma(\frac{n}{2})} \sum_{l=1}^{\infty} d_l q_{n,l} \sum_{m=1}^{N(n,l)} g_l^m(u) Y_l^m(\omega), \tag{3.24}$$

where

$$q_{n,l} = 4^{-(n+1)/2} \prod_{k=0}^{(n-1)/2} [l(l + n - 2) + (2k - 1)(n - 1 - 2k)] \tag{3.25}$$

and

$$d_l = |\mathbb{S}^{n-2}| \int_{-1}^{1} \log \frac{1}{|t|} p_l^{(n-2)/2}(t)(1 - t^2)^{(n-3)/2} dt, \tag{3.26}$$

with $p_l^{(n-2)/2}$ being the l-th degree Gegenbauer polynomial (see Appendix B.1.2).

Proof. Plugging (3.23) into the second term in the right hand side of (3.17), we obtain

$$Rf(\omega,\omega\cdot u)=\frac{\Gamma(\frac{n+1}{2})}{2\pi^{(n+1)/2}}\int\limits_{\mathbb{S}^{n-1}}G(u,\beta)d\beta \tag{3.27}$$
$$-\frac{2P_{(n+1)/2}(\Delta_{\mathbb{S}})}{\pi^{n/2}\Gamma(\frac{n}{2})}\sum_{l=0}^{\infty}\sum_{m=1}^{N(n,l)}g_l^m(u)\int\limits_{\mathbb{S}^{n-1}}\log\frac{1}{|\omega\cdot\beta|}Y_l^m(\beta)d\beta.$$

We note that $\int\limits_{\mathbb{S}^{n-1}}G(u,\beta)d\beta=2\sqrt{\pi}g_0^1(u)$. Then Funk-Hecke formula (see Theorem B.1.1) implies that

$$\int\limits_{\mathbb{S}^{n-1}}\log\frac{1}{|\omega\cdot\beta|}Y_l^m(\beta)d\beta=d_lY_l^m(\omega),$$

where d_l is as in (3.26). Also, since $\Delta_{\mathbb{S}}Y_l=-l(l+n-2)Y_l$, $l=0,1,2,...$, we have $P_{(n+1)/2}(\Delta_{\mathbb{S}})Y_l=q_{n,l}Y_l$, where $q_{n,l}$ is given in (3.25). Hence, we get the result. □

In particular, for $n=3$, we get

Corollary 3.6.2. *For any $u\in\mathbb{R}^3$ and $\omega\in S^2$,*

$$Rf(\omega,\omega\cdot u)=\pi^{-3/2}g_0^1(u)-\frac{1}{4\pi^2}\sum_{l=1}^{\infty}d_lq_l\sum_{m=1}^{2l+1}g_l^m(u)Y_l^m(\omega), \tag{3.28}$$

where $q_l=(l-1)l(l+1)(l+2)$ and $d_l=2\pi\int\limits_{-1}^{1}\log\frac{1}{|t|}p_l^{(n-2)/2}(t)dt$ with $p_l^{(n-2)/2}$ being the l-th degree Gegenbauer polynomial (see Appendix B.1.2).

Remark 3.6.3. The coefficients q_l in (3.28) are fourth order polynomials in l and account for fourth order differentiation. Thus, it is expected to face an instability issue in the numerical implementation of (3.28) when considering high degree spherical harmonics.

In our numerical tests, the phantom was the characteristic function of the 3D ball of radius 0.5 centered at the origin, while the Compton detectors covered the concentric unit

sphere. The reason for considering a radial phantom is that its Radon transform can easily be computed analytically. On the other hand, the Compton data was simulated numerically and then used to numerically reconstruct the Radon data via (3.28). The results can then be compared with the exact (analytically computed) Radon transforms[4].

Figure 3.4 shows the comparison of the analytically computed Radon transform of the phantom (shown in red) with its reconstructions, using (3.28). The results are illustrated for the direction $\omega = [-0.2342, -0.1844, -0.9545]$. In obtaining the Radon data $Rf(\omega, s)$ for uniformly sampled $s \in [-1, 1]$ from $Rf(\omega, u \cdot \omega)$, we used MATLAB® toolbox `cftool` with spline fitting having a smoothing parameter 0.99. The cone data is numerically simulated for 1806 detector points on the sphere and 90 opening angles ψ. For the cone axis direction vectors, we used varying discretization of the sphere corresponding to 1806, 7446, and 30054 points. We have considered spherical harmonics up to degree $l = L = 30$ in the expansion (3.23). In order to reduce the effect of instability, we only used $l = L_t$ in the computation of the Radon transform via (3.28) equal to 18.

[4]Tests on non-radial phantoms have lead to similar results.

ALGORITHM Numerical Implementation of (3.28)

Data: $c_{i,j,k} = Cf(u_i, \beta_j, \psi_k)$, $i = 1, ..., U$, $j = 1, ..., B$, $k = 1, ..., P$.

1: For $l = 1, ..., L$, pre-compute

$$q_l = (l-1)l(l+1)(l+2) \text{ and } d_l \sim \sum_{i=1}^{T} p_l^{(n-2)/2}(t_i)\Delta t$$

with $p_l^{(n-2)/2}$ being the l-th degree Gegenbauer polynomial.

2: For $i = 1, ..., U$, $j = 1, ..., B$ compute

$$G(u_i, \beta_j) := \sum_{k=1}^{P} c_{i,j,k} \sin\psi_k \Delta\psi \sim \int_0^{\pi} Cf(u, \beta, \psi) \sin\psi d\psi.$$

3: For $i = 1, ..., U$, and $l = 1, ..., L$, carry out the integral

$$g_l^m(u_i) = \sum_{\tau \in K} \frac{Area(\tau)}{3} \sum_{v \in V(\tau)} G(u_i, v)\overline{Y_l^m(v)} \sim \int_{\mathbb{S}^{n-1}} G(u, \beta)\overline{Y_l^m(\beta)} d\beta,$$

where $m = 1, ..., 2l+1$, τ is a face of the triangular mesh K on $\mathbb{S}^2$, and $V(\tau)$ is the set of vertices of τ.

4: For $i = 1, ..., U$, $j = 1, ..., T$, and $\omega_j \in K$, a triangular mesh on $\mathbb{S}^2$, compute

$$Rf(\omega_j, \omega_j \cdot u_i) = \pi^{-3/2} g_0^1(u) - \frac{1}{4\pi^2} \sum_{l=1}^{Lt} d_l q_l \sum_{m=1}^{2l+1} g_l^m(u_i) Y_l^m(\omega_j).$$

5: Carry out 1D interpolation to obtain $Rf(\omega_j, s_k)$ for a uniform mesh $\{s_k\}$ on $[-1, 1]$.

6: Apply filtered backprojection algorithm for the Radon transform to obtain $f_{i,j,l}$ from $Rf(\omega_j, s_k)$ where i, j, l runs over the reconstruction grid $[-1, 1]^3$.

Result: $f_{i,j,l}$ is an approximation to the phantom f which is supported on the unit sphere.

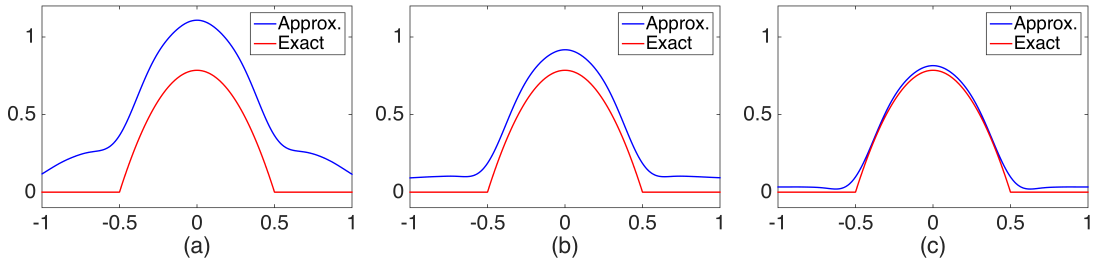

Figure 3.4: The analytically computed Radon transform of the phantom (shown in red) vs. its reconstruction from the Compton data using (3.28). The reconstructions shown correspond to three different mesh sizes: the number of points on the sphere being 1806, 7446, and 30054, from left to right.

3.6.2 Method 2: Reconstruction by Direct Implementation of Theorem 3.4.5

As we have mentioned before, the direct numerical implementation of the formula (3.17) in 3D required the application of the fourth order differential operator $\Delta_{\mathbb{S}}(\Delta_{\mathbb{S}}+2)$ on the sphere to the result of numerical implementation of a singular integral. The dissertant could not make it work well. The advantage of using (3.21) is that one needs to apply two second order operators acting in different variables and with a smoothing operator sandwiched in between. This makes such a calculation more feasible.

In our numerical implementations, we used the algorithm for the discrete Laplace-Beltrami operator given in [7], which comprises heat equation based smoothing used to create a point-wise convergent approximation for the Laplace-Beltrami operator on a surface. For a function f given at the set V of vertices of a mesh K on the 2-sphere, it is computed, for any $v \in V$, as follows:

$$\Delta_K^h f(v) = \frac{1}{4\pi h^2} \sum_{t \in K} \frac{Area(t)}{\#t} \sum_{p \in V(t)} e^{-\frac{\|p-v\|^2}{4h}} (f(p) - f(v)). \tag{3.29}$$

Here, for any face $t \in K$, the number of vertices in t is denoted by $\#t$, and $V(t)$ is the set of vertices of t. The parameter h is a positive quantity (akin to the time in the heat equation), which intuitively corresponds to the size of the neighborhood considered at each point. The authors of [7] suggest that h can be taken to be a function of v, which allows the algorithm to adapt to the local mesh size.

In our experiments, we used the adaptive parameter $h(v) = 0.0156\times$(the average edge length at v). We used the same phantom as in the previous section. Figure 3.5 shows the comparison of the analytically computed Radon transform of the phantom (shown in red) with its reconstructions. The results are illustrated for the direction $\omega = [-0.2363, -0.2484, -0.9394]$. In obtaining the Radon data for uniformly sampled $s \in [-1, 1]$ from $Rf(\omega, u \cdot \omega)$, we used the same MATLAB® toolbox `cftool` with spline fitting having a smoothing parameter 0.995. The cone data is numerically simulated for 1806 detector points on the sphere and 90 opening angles ψ. For the cone axis direction vectors, we used varying discretization of the sphere corresponding to 1806, 7446, and 30054 points.

ALGORITHM Numerical Implementation of (3.20)

Data: $c_{i,j,k} = Cf(u_i, \beta_j, \psi_k)$, $i = 1, ..., U$, $j = 1, ..., B$, $k = 1, ..., P$.

1: For $i = 1, ..., U$, $j = 1, ..., B$ compute

$$G(u_i, \beta_j) := \sum_{k=1}^{P} c_{i,j,k} \sin \psi_k \Delta\psi \sim \int_0^{\pi} Cf(u, \beta, \psi) \sin \psi d\psi.$$

2: For $i = 1, ..., U$, and $l = 1, ..., L$, apply discrete Laplace-Beltrami operator (3.29) in β to $G(u_i, \beta_j)$.

3: For $i = 1, ..., U$, $j = 1, ..., T$, compute $\Phi(u_i, \beta_j)$ as in (3.19).

4: For $i = 1, ..., U$, and $l = 1, ..., L$, carry out the integrals

$$\int_{\mathbb{S}^{n-1}} \Phi(u, \beta) d\beta \sim \sum_{\tau \in K} \frac{Area(\tau)}{3} \sum_{v \in V(\tau)} \Phi(u_i, v)$$

and, for $\omega_j \in K$, a triangular mesh on $\mathbb{S}^2$,

$$\int_{\mathbb{S}^{n-1}} \Phi(u, \beta) \log \frac{1}{|\omega \cdot \beta|} d\beta \sim \sum_{\tau \in K} \frac{Area(\tau)}{3} \sum_{v \in V(\tau)} \Phi(u_i, v) \log \frac{1}{|\omega_j \cdot v|}.$$

where τ is a face of the triangular mesh K on $\mathbb{S}^2$, and $V(\tau)$ is the set of vertices of τ.

5: Using the results of the previous step, compute $Rf(\omega_j, \omega_j \cdot u_i)$ as in (3.20).

6: Carry out 1D interpolation to obtain $Rf(\omega_j, s_k)$ for a uniform mesh $\{s_k\}$ on $[-1, 1]$.

7: Apply filtered backprojection algorithm for the Radon transform to obtain $f_{i,j,l}$ from $Rf(\omega_j, s_k)$ where i, j, l runs over the reconstruction grid $[-1, 1]^3$.

Result: $f_{i,j,l}$ is an approximation to the phantom f which is supported on the unit sphere.

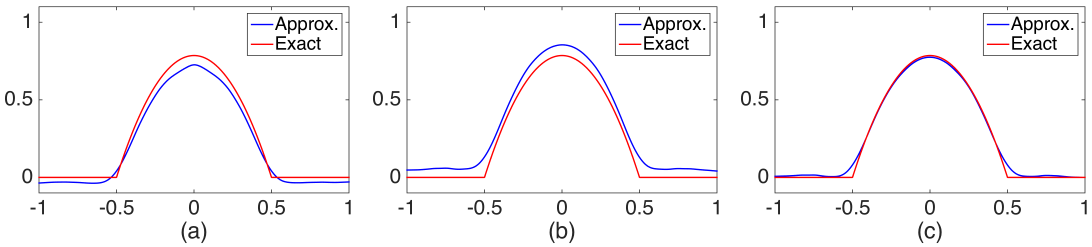

Figure 3.5: The Radon transform of the phantom recovered using (3.21) and (3.29). The reconstructions shown corresponds to three different mesh sizes: the number of points on the sphere being 1806, 7446, and 30054, from left to right.

3.6.3 Method 3: Reconstruction via a Mollified Inversion of the Cosine Transform

The formula (3.10) shows that availability of any cosine transform inversion would also lead to an inversion of the cone transform, and such approximate and exact inversions of $\mathfrak{C}$ indeed exist [40,51,52]. We apply here the method of approximate inverse developed in [39, 40, 51], which is an incarnation of a general approach to solving inverse problems numerically. Namely, for a given data h, the aim is to find g satisfying $\mathfrak{C}g = h$. If we find a 'Green's function' ψ such that $\mathfrak{C}\psi = \delta$, then the spherical convolution $h * \psi$ of h and ψ solves the equation $\mathfrak{C}g = h$. Now, if one picks a 'mollifier' (an approximation to the δ-function) δ_γ and "approximate Greens function" ψ_γ, such that $\mathfrak{C}\psi_\gamma = \delta_\gamma$, then one finds the approximate solution $g_\gamma = g * \delta_\gamma$.

In our numerical tests, we used the reconstruction kernel ψ_γ that was analytically computed in [51] for a special class of mollifiers (see [51, (4.1) and (4.10)]). We used the same phantom as in the previous sections. Figure 3.6 shows the comparison of the analytically computed Radon transform of the phantom (shown in red) with its reconstructions, using (3.28). The results are illustrated for the direction $\omega = [-0.2342, -0.1844, -0.9545]$. The MATLAB® toolbox `cftool` was used with the smoothing parameter 0.99999999. The

cone data is numerically simulated for 1806 detector points on the sphere and 90 opening angles ψ. For the cone axis direction vectors, we used varying discretization of the sphere corresponding to 1806, 7446, and 30054 points.

ALGORITHM Reconstruction via a mollified inversion of the Cosine Transform

Data: $c_{i,j,k} = Cf(u_i, \beta_j, \psi_k)$, $i = 1, ..., U$, $j = 1, ..., B$, $k = 1, ..., P$.

1: For $i = 1, ..., U$, $j = 1, ..., B$ compute

$$G(u_i, \beta_j) := \sum_{k=1}^{P} c_{i,j,k} \sin \psi_k \Delta\psi \sim \int_0^{\pi} Cf(u, \beta, \psi) \sin \psi d\psi.$$

2: For $i = 1, ..., U$, and for $\omega_l \in K$, a triangular mesh on $\mathbb{S}^2$, compute

$$Rf(\omega_l, \omega_l \cdot u_i) = 4 \sum_{\tau \in K} \frac{Area(\tau)}{3} \sum_{v \in V(\tau)} G(u_i, v) \psi^{\gamma}(\omega_l \cdot v) \sim 4 \int_{\mathbb{S}^{n-1}} G(u, \beta) \psi^{\gamma}(\omega \cdot \beta) d\beta.$$

where ψ^{γ} is given as in [51, Theorem 4.7], and τ is a face of the triangular mesh K on $\mathbb{S}^2$, and $V(\tau)$ is the set of vertices of τ.

3: Carry out 1D interpolation to obtain $Rf(\omega_l, s_k)$ for a uniform mesh $\{s_k\}$ on $[-1, 1]$.

4: Apply filtered backprojection algorithm for the Radon transform to obtain $f_{i,j,l}$ from $Rf(\omega_l, s_k)$ where i, j, l runs over the reconstruction grid $[-1, 1]^3$.

Result: $f_{i,j,l}$ is an approximation to the phantom f which is supported on the unit sphere.

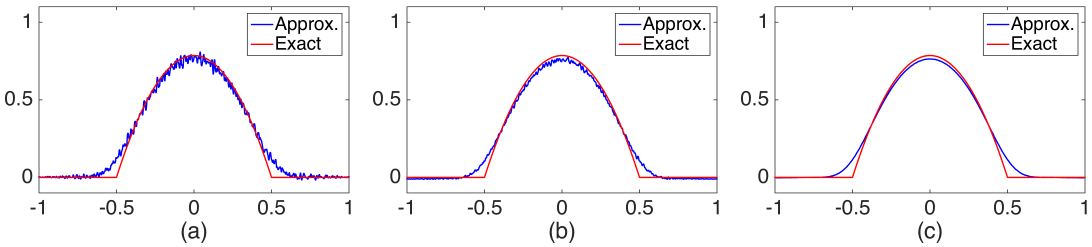

Figure 3.6: The Radon transform of the phantom using the method of mollified inverse for the cosine transform. The reconstructions shown corresponds to three different mesh sizes: the number of points on the sphere being 1806, 7446, and 30054, from left to right.

One notices insufficient resolution of singularity, which is due to the insufficiently fine approximation of δ-function by δ_γ chosen in [40, 51].

3.6.4 Comparison of the Three Methods

While above we only addressed reconstructing the Radon transform of the function in question, here we show how the three methods perform after taking the final step of inverting the Radon transform and reconstructing the characteristic function of the ball.

The inversion of Radon transform from the reconstructed values $Rf(\omega, s)$ was done according to the formula (B.16) with $\alpha = 0$. We used 128 values of s and 480 directions ω in methods 1 and 3, and 1806 directions in method 2. We used the filtered backprojection formula with the filter given in [41]. The normalized L^2 and H^1 errors for the Radon transforms obtained in each of the methods are summarized in Table 3.1. The reason for considering the H^1-error is the fact that H^1-norm control of the 3D Radon transform data Rf corresponds to the L^2-norm control of the tomogram f [46].

Method	L^2 Error	H^1 Error
1	0.0986	0.3231
2	0.1046	0.3767
3	0.0896	0.3660

Table 3.1: The normalized L^2 and H^1 errors for the Radon data for each of the three methods.

Figure 3.7 shows the three cross-sections of the spherical phantom and of its reconstructions from the Radon data obtained via the three methods above. The finest mesh on the sphere (30054 points) was used.

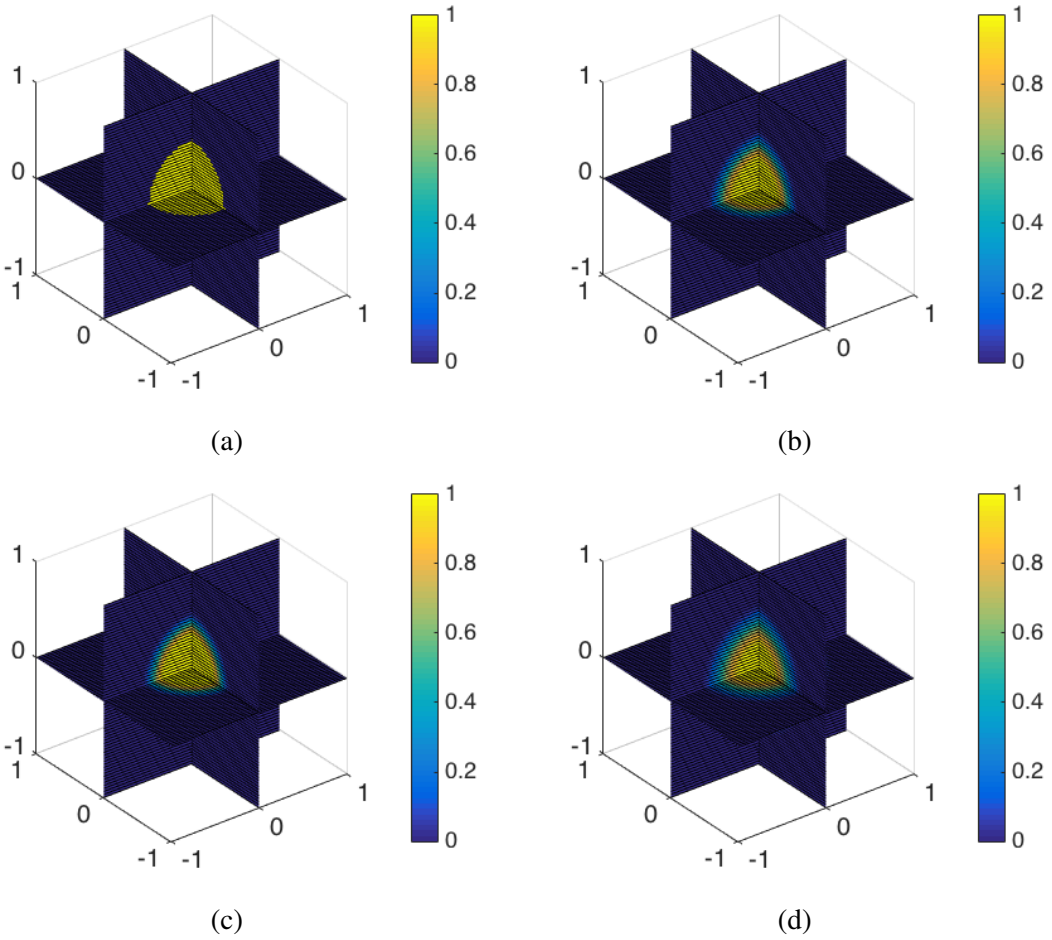

Figure 3.7: Comparison of the three reconstruction methods. The cross-sections by the coordinate planes are shown. (a) The phantom is the characteristic function of 3d ball having radius 0.5 and center at the origin. (b) Reconstruction via Method 1. (c) Reconstruction via Method 2. (d) Reconstruction via Method 3.

Figure 3.8 shows x-profiles of the central cross-sections of the spherical phantom and of its reconstructions shown in Figure 3.7.

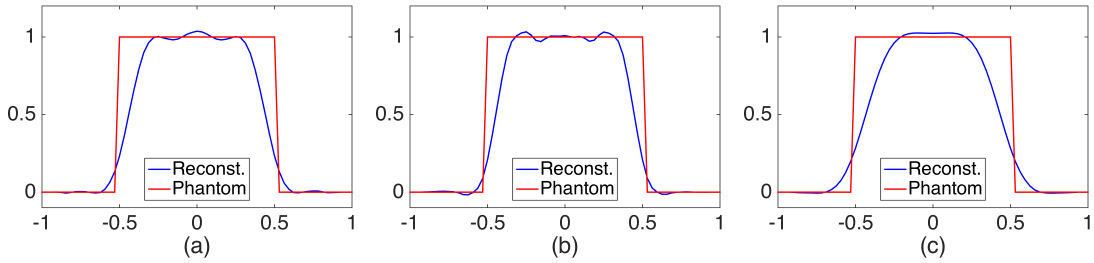

Figure 3.8: x-profiles of the phantom and the reconstructions in Figure 3.7, (a) method 1, (b) method 2 and (c) method 3.

It is important to note that in all of the methods, there are parameters that can still be optimized, namely L and L_t in Method 1, h in Method 2, and γ and ν in Method 3 (see [51]).

We have also tested the reaction of our algorithms to random noise. The 20% Gaussian white noise added to the cone data for Methods 1 and 2. For Method 2, we added 10% noise to the cone data. Figure 3.9 shows the three cross-sections of the spherical phantom and of its reconstructions from the Radon data obtained via the three methods above. The finest mesh on the sphere (30054 points) was used.

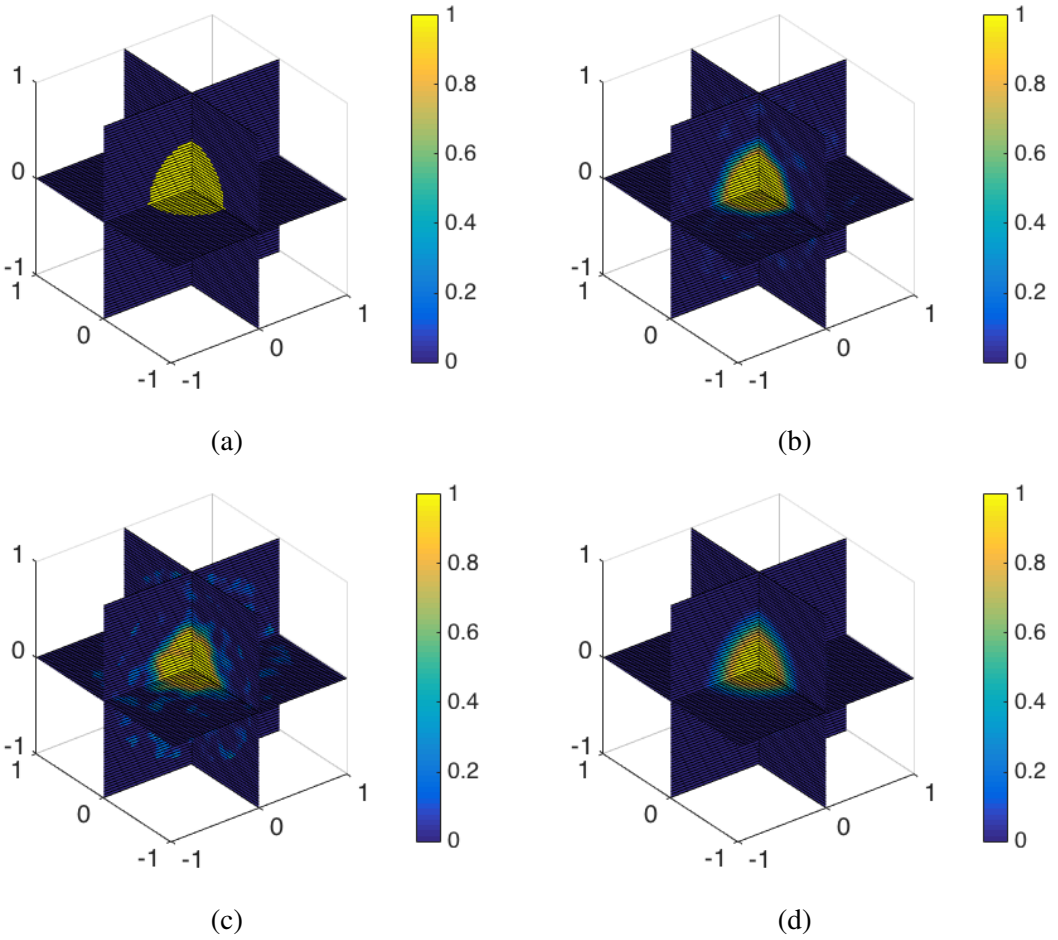

Figure 3.9: Comparison of the three reconstruction methods. The cross-sections by the coordinate planes are shown. (a) The phantom is the characteristic function of 3d ball having radius 0.5 and center at the origin. (b) Reconstruction via Method 1 from data contaminated with 20% Gaussian white noise. (c) Reconstruction via Method 2 from data contaminated with 10% Gaussian white noise. (d) Reconstruction via Method 3 from noisy data contaminated with 20% Gaussian white noise.

Figure 3.10 shows x-profiles of the central cross-sections of the spherical phantom and of its reconstructions shown in Figure 3.9.

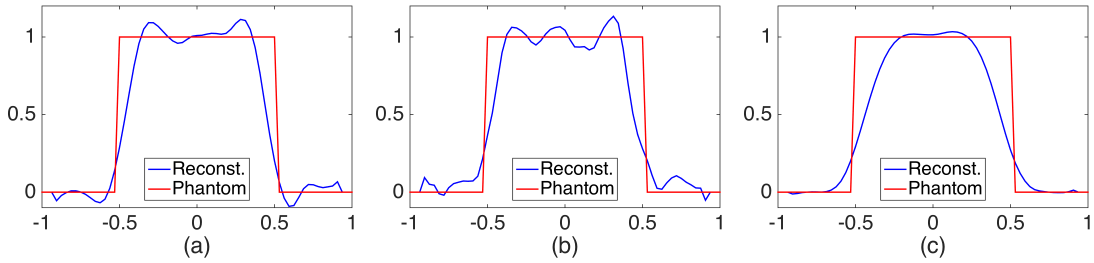

Figure 3.10: Comparison of x-profiles of central slices of phantom and the reconstructions from noisy data shown in Figure 3.9.

4. INVERSION OF WEIGHTED DIVERGENT BEAM AND CONE TRANSFORMS[1]

In this chapter, we consider the weighted divergent beam and cone transforms, and discuss their inversion. In Section 4.1, we define the weighted divergent beam and cone transforms and describe a simple relation between them. In Section 4.2, we present a variety of inversion formulas for the weighted divergent beam transform (Theorems 4.2.5 and 4.2.7). We then derive an integral relation between the weighted divergent beam and cone transforms in Section 4.3, which leads to new inversion formulas for the n-dimensional weighted cone transform (Theorem 4.3.6). In Section 4.4, we investigate the relation between the Radon and weighted divergent beam and cone transforms. This enables us to derive other inversion formulas for the latter two (Theorem 4.4.4). Section 4.5 contains the results of numerical implementation of some of the inversion formulas for the weighted cone transform in dimensions two and three for two different vertex geometries, as well as examples of numerical inversion of two weighted divergent beam transforms in dimension three.

4.1 The Weighted Cone and Divergent Beam Transforms

In this section, we define the closely related weighted divergent beam and cone transforms.

Definition 4.1.1. For $k > -1$, the *k-weighted divergent beam transform* of a function

[1]Reprinted from: Inversion of weighted divergent beam and cone transforms, by P. Kuchment and F. Terzioglu, Inverse Problems & Imaging, Volume 11, 2017. Copyright © by AIMS. Reprinted with the permission of AIMS.

$f \in \mathcal{S}(\mathbb{R}^n)$ is defined by

$$D^k f(u,\sigma) = D_u^k f(\sigma) := \int_0^\infty f(u+\rho\sigma)\rho^k d\rho, \tag{4.1}$$

where $u \in \mathbb{R}^n$ is the *source* of the beam $\{u+\rho\sigma\}|_{\rho\geq 0}$ and $\sigma \in \mathbb{S}^{n-1}$ is the unit vector in the direction of the beam.

Consider now a circular cone[2] $\mathfrak{S}$ in $\mathbb{R}^n$. The set of such cones can be parametrized by a triple (u,β,ψ), where $u \in \mathbb{R}^n$ is the cone's *vertex (apex)*[3], the unit vector $\beta \in \mathbb{S}^{n-1}$ is directed toward cone's interior along the cone's axis, and $\psi \in (0,\pi)$ is the opening angle (see Fig. 4.1). A point $x \in \mathbb{R}^n$ lies on $\mathfrak{S}(u,\beta,\psi)$ iff $(x-u)\cdot\beta = |x-u|\cos\psi$.

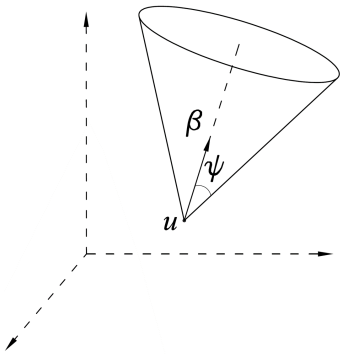

Figure 4.1: A cone with vertex $u \in \mathbb{R}^n$, central axis direction vector $\beta \in \mathbb{S}^{n-1}$ and opening angle $\psi \in (0,\pi)$.

Definition 4.1.2. Let $k \in \mathbb{Z}_+ = \{0,1,2,...\}$, and suppose that $f \in \mathcal{S}(\mathbb{R}^n)$. We define *the*

[2]The word "cone" in this paper always means a surface, rather than solid cone.

[3]In the Compton camera imaging, cone's vertex corresponds to a detection location.

k-weighted cone transform $C^k f$ of f as

$$C^k f(u,\beta,\psi) := \int_{\mathfrak{S}(u,\beta,\psi)} f(x)|x-u|^{k-n+2} dS(x), \tag{4.2}$$

where dS is the surface measure on the cone $\mathfrak{S}$. In other words,

$$C^k f(u,\beta,\psi) = \sin\psi \int_{\mathbb{R}^n} f(x)\delta((x-u)\cdot\beta - |x-u|\cos\psi)|x-u|^{k-n+2} dx, \tag{4.3}$$

where dx is the Lebesgue measure on $\mathbb{R}^n$.

Remark 4.1.3.

- To avoid confusion, note that the power in the integral weight in the definition of $C^k f$ is not equal to k, but rather also depends on the spatial dimension n.
- At this step, one can allow all real values $k > -1$, while later on, $k \in \mathbb{Z}_+ := \{0, 1, 2, \dots\}$ will be important.
- We note that $k = n-2$ corresponds to the case of pure surface measure on the cone.

Remark 4.1.4. We will say just "weighted" cone or divergent beam transform, when no confusion about the value of k can arise.

Changing variables in (4.3) as $x = u + \rho\sigma$ for $\rho \in [0,\infty)$ and $\sigma \in \mathbb{S}^{n-1}$, and using the fact that δ is homogeneous of degree -1, we make the following simple observation:

Proposition 4.1.5. *Let $u \in \mathbb{R}^n, \beta \in \mathbb{S}^{n-1}$ and $\psi \in (0,\pi)$. Then,*

$$\begin{aligned} C^k f(u,\beta,\psi) &= \sin\psi \int_{\mathbb{S}^{n-1}} \int_0^\infty f(u+\rho\sigma)\rho^k d\rho\, \delta(\sigma\cdot\beta - \cos\psi) d\sigma \\ &= \sin\psi \int_{\mathbb{S}^{n-1}} D_u^k f(\sigma)\delta(\sigma\cdot\beta - \cos\psi) d\sigma. \end{aligned} \tag{4.4}$$

By letting $t = \cos\psi$, we can rewrite (with an abuse of notation) $C^k f$ as

$$C^k f(u,\beta,t) := \begin{cases} \sqrt{1-t^2}\displaystyle\int_{\mathbb{S}^{n-1}} D_u^k f(\sigma)\delta(\sigma\cdot\beta - t)d\sigma, & \text{if } |t|\le 1 \\ 0, & \text{otherwise.} \end{cases} \tag{4.5}$$

4.2 Inversion of the Weighted Divergent Beam Transform

If $f \in \mathcal{S}(\mathbb{R}^n)$, for each $u \in \mathbb{R}^n$, $D_u^k f(\sigma)$ can be uniquely extended to a smooth function on $\mathbb{R}^n\backslash\{0\}$ homogeneous of degree $-(k+1)$:

$$D_u^k f(x) = \frac{1}{|x|^{k+1}} D_u^k f(\frac{x}{|x|}). \tag{4.6}$$

This function is locally integrable with respect to $x \in \mathbb{R}^n$, provided $k < n-1$, and has a well-defined Fourier transform as a tempered distribution (see e.g. [17]), i.e., for each $\varphi \in \mathcal{S}(\mathbb{R}^n)$,

$$\langle \widehat{D_u^k f}(\xi), \varphi(\xi)\rangle = \int_{\mathbb{R}^n} D_u^k f(y)\hat{\varphi}(y)dy. \tag{4.7}$$

In the following, we derive inversion formulas for the divergent beam transform that are analogs of the well known [63,64] Tuy's inversion formula, which addresses the case when $k = 0$ in dimension three, and the sources (detectors in the Compton camera case) move along a curve.

In the rest of the paper, the shorthand notations ∂_{u_j} and ∂_u will be used for the partial derivatives $\partial/\partial u_j$ and gradient ∇_u with respect to the variables u.

Theorem 4.2.1. *Let $k \in \mathbb{Z}_+$, $f \in \mathcal{S}(\mathbb{R}^n)$, and all source locations u are accessible. Then,*

$$f(x) = \frac{(-i)^{k+1}}{(2\pi)^n}\int_{\mathbb{S}^{n-1}} \left(\Delta_u^{(k+1)/2}\widehat{D_u^k f}(\theta)\right)\Big|_{u=x} d\theta, \tag{4.8}$$

where $\Delta_u := \sum_j \partial_{u_j}^2$ is the Laplace operator with respect to the variable u, and its power when k is not an odd integer is understood as the corresponding Riesz potential (see, e.g. [46]).

Proof. Let $f \in \mathcal{S}(\mathbb{R}^n)$. For any $\theta \in \mathbb{S}^{n-1}$, the Fourier transform of $D_u^k f$ satisfies

$$\widehat{D_u^k f}(\theta) = \int_0^\infty e^{i\rho\theta\cdot u} \hat{f}(\rho\theta)\rho^{n-k-2} d\rho. \tag{4.9}$$

Indeed, for any $\varphi \in \mathcal{S}(\mathbb{R}^n)$, due to $D_u^k f$ being homogeneous of degree $-(k+1)$ and changing to polar variables $y = s\omega$, we have

$$\begin{aligned}
\langle \widehat{D_u^k f}, \varphi\rangle = \langle D_u^k f, \hat{\varphi}\rangle &= \int_{\mathbb{R}^n} D_u^k f(y)\hat{\varphi}(y) dy \\
&= \int_{\mathbb{S}^{n-1}} \int_0^\infty D_u^k f(\omega)\hat{\varphi}(s\omega) s^{n-k-2} ds d\omega \\
&= \int_{\mathbb{R}^n} \varphi(x) \int_{\mathbb{S}^{n-1}} \int_0^\infty \int_0^\infty e^{-ix\cdot s\omega} f(u+r\omega) s^{n-k-2} ds\ r^k dr d\omega\ dx.
\end{aligned}$$

Now, changing variables in s to $\rho = s/r$, and then letting $y = u + r\omega$, we get

$$\begin{aligned}
\langle \widehat{D_u^k f}, \varphi\rangle &= \int_{\mathbb{R}^n} \varphi(x) \int_0^\infty \int_{\mathbb{S}^{n-1}} \int_0^\infty e^{-ix\cdot r\rho\omega} f(u+r\omega) r^{n-1} dr d\omega \rho^{n-k-2} d\rho\ dx \\
&= \int_{\mathbb{R}^n} \varphi(x) \int_0^\infty \int_{\mathbb{R}^n} e^{-i\rho x\cdot(y-u)} f(y) dy \rho^{n-k-2} d\rho\ dx,
\end{aligned}$$

which implies (4.9).

The following simple formula holds for any unit vector θ:

$$\Delta_u^{(k+1)/2} e^{i\rho\theta\cdot u} = (i\rho)^{k+1} e^{i\rho\theta\cdot u}. \tag{4.10}$$

Thus, applying (k+1)/2-th power of the Laplace operator with respect to u to (4.9), we

obtain

$$\Delta_u^{(k+1)/2}\widehat{D_u^k f}(\theta) = i^{k+1}\int_0^\infty e^{i\rho\theta\cdot u}\hat{f}(\rho\theta)\rho^{n-1}d\rho. \tag{4.11}$$

Now, recalling the Fourier inversion formula in polar coordinates

$$f(x) = \frac{1}{(2\pi)^n}\int_{\mathbb{S}^{n-1}}\int_0^\infty e^{i\rho\theta\cdot x}\hat{f}(\rho\theta)\rho^{n-1}d\rho d\theta \tag{4.12}$$

and comparing with (4.11), we obtain the desired formula

$$f(x) = \frac{(-i)^{k+1}}{(2\pi)^n}\int_{\mathbb{S}^{n-1}}\left(\Delta_u^{(k+1)/2}\widehat{D_u^k f}(\theta)\right)\Big|_{u=x}d\theta.$$

□

Remark 4.2.2. Considering formula (4.8), one realizes quickly that it is not very useful, since it requires "sources" u of the beams to be available throughout the whole space. In the Compton camera case, as well as in 3D CT, this would require detectors/sources to be placed throughout the object imaged, which is impossible.

Moreover, in this case, one deals with just a deconvolution problem, and a severely overdetermined one at that (the dimension of the data used is $2n-1$ instead of n). Thus, there must exist formulas requiring much less data, in particular allowing the detectors u to be situated only outside the object being imaged (e.g. Tuy's formula only requires an arc of external sources).

This is also related to the interesting question about "admissible" complexes of cones that provide enough data for stable reconstruction. We have already briefly addressed this issue in [37, 60] and plan to have more detailed discussion elsewhere.

Here we show an example of how such deficiency can be alleviated for the weighted

divergent beam transform.

Definition 4.2.3.

- Let $\mathcal{M} \subset \mathbb{R}^n$ be a smooth d-dimensional submanifold. We will say that it satisfies the *Tuy's condition* with respect to a subset $V \subset \mathbb{R}^n$, if any hyperplane intersecting V has a non-tangential intersection with $\mathcal{M}$.

  Equivalently: for any $x \in V$ and unit vector $\theta \in \mathbb{S}^{n-1}$, there exists a point $u \in \mathcal{M}$ such that $\theta \cdot x = \theta \cdot u$, and θ is not normal to $\mathcal{M}$ at the point u.

- We denote by P_u the orthogonal projection onto the tangent space to $\mathcal{M}$ at the point $u \in \mathcal{M}$.

Remark 4.2.4. Notice that the above condition is a strengthened version of what was called *admissibility condition* in [37, 60].

Theorem 4.2.5. *Let k be an odd non-negative integer and $\mathcal{M} \subset \mathbb{R}^n$ satisfies Tuy's condition with respect to a compact V. Then, for any homogeneous linear elliptic differential operator $L(u, \partial_u)$ of order $k+1$ on $\mathcal{M}$ and any smooth function f supported in V, the following inversion formula holds:*

$$f(x) = \frac{1}{(2\pi)^n} \int_{\mathbb{S}^{n-1}} \frac{1}{L(u, P_u\theta)} L(u, \partial_u) \widehat{D_u^k f}(\theta) d\theta, \tag{4.13}$$

where $u \in \mathcal{M}$ is related to x and θ as in the Tuy's condition.

If $\mathcal{M}$ is one-dimensional, then k can be any natural number (in this case, when $k = 0$, one ends up with the standard Tuy's formula).

Remark 4.2.6.

- Notice that $u \in \mathcal{M}$ in (4.13) depends on both x and θ and that $L(u, P_u\theta)$ does not vanish if the Tuy's condition is satisfied.

- The differential expression in the formula above is written in the variable u, while the actual variables at hand are θ and x. Due to the non-tangentiality required in the Tuy's condition, such a differential operator can be locally lifted to an operator in (x, θ) variables (which requires a specific calculation for each manifold of detectors).

- The choice of u in Tuy's condition might not be unique, and any such choice will work.

Proof. The proof follows exactly the one of Theorem 4.2.1, using at the end the formula for the symbol of a homogeneous differential operator of order $k+1$ (instead of a power of the Laplacian in (4.10)):

$$L(u, \partial_u) e^{i\rho\theta\cdot u} = (i\rho)^{k+1} L(u, P_u\theta) e^{i\rho\theta\cdot u} \tag{4.14}$$

and noticing that the factor $L(u, P_u\theta)$ does not vanish, due to the ellipticity and homogeneity of the operator and the Tuy's condition. □

A serious deficiency in Theorem 4.2.5 is that, unless $\mathcal{M}$ is one-dimensional, only odd values of k are allowed. This issue can be resolved, paying the price of having a more complex formula.

Indeed, consider the following first order linear differential operator acting tangentially to $\mathcal{M}$, with coefficients depending upon $u \in \mathcal{M}$ and $\theta \in \mathbb{S}^{n-1}$:

$$O(u, \theta, \partial_u) := P_u\theta \cdot \partial_u. \tag{4.15}$$

Let also $L(u, \partial_u)$ be an operator like in Theorem 4.2.5, but of order k. Applying the composition $O \circ (aL)$ to the exponential $e^{i\rho\theta\cdot u}$, where $a := 1/L(u, P_u\theta)$, and using (4.14),

we get

$$O \circ (aL)e^{i\rho\theta\cdot u} = |P_u\theta|^2(i\rho)^{k+1}e^{i\rho\theta\cdot u}. \tag{4.16}$$

Since the order of the composition is odd, this enables us to extended the inversion formula to the even values of k:

Theorem 4.2.7. *Let k be an even non-negative integer and $\mathcal{M} \subset \mathbb{R}^n$ satisfies Tuy's condition with respect to a compact V. Then, for any homogeneous elliptic differential operator $L(u, \partial_u)$ of order k on $\mathcal{M}$ and any smooth function f supported in V, the following inversion formula holds:*

$$f(x) = \frac{1}{(2\pi)^n}\int_{\mathbb{S}^{n-1}} \frac{1}{|P_u\theta|^2}\big(O \circ \frac{1}{L(u, P_u\theta)}L\big)\widehat{D_u^k f}(\theta)d\theta, \tag{4.17}$$

where u is related to x and θ as in the Tuy's condition.

Proof. The proof stays exactly the same, except instead of (4.14), we use (4.16). □

Remark 4.2.8. Since we are dealing with a severely overdetermined transform, the variety of possible inversion formulas is large and is not exhausted by the ones above. For instance, instead of using the operator $\frac{1}{|P_u\theta|^2}(O \circ \frac{1}{L(u,P_u\theta)}L)$, one can use $(\frac{1}{|P_u\theta|^2}O)^{k+1}$.

4.3 Inversion of the Weighted Cone Transform

The following result presents a relation between the weighted divergent beam and cone transforms defined in section 4.1, which will be instrumental in the inversion of the latter one.

Proposition 4.3.1. *Suppose that $f \in \mathcal{S}(\mathbb{R}^n)$, and $h(t)$ is a distribution on $\mathbb{R}$ regular near $t = \pm 1$. Then,*

$$\big\langle h(t), \frac{C^k f(u, \beta, t)}{\sqrt{1-t^2}}\big\rangle_{\mathbb{R}} = \langle h(\sigma\cdot\beta), D_u^k f(\sigma)\rangle_{\mathbb{S}^{n-1}}. \tag{4.18}$$

(Notice that $C^k f(u,\beta,t) = 0$ for $|t| > 1$, and is smooth for $|t| < 1$.)

Proof. By the representation (4.5) of the weighted cone transform, we have

$$\begin{aligned}\Big\langle h(t), \frac{C^k f(u,\beta,t)}{\sqrt{1-t^2}}\Big\rangle_{\mathbb{R}} &= \big\langle h(t), \langle \delta(\sigma\cdot\beta - t), D_u^k f(\sigma)\rangle_{\mathbb{S}^{n-1}}\big\rangle_{\mathbb{R}} \\ &= \big\langle (h*\delta)(\sigma\cdot\beta), D_u^k f(\sigma)\big\rangle_{\mathbb{S}^{n-1}} = \langle h(\sigma\cdot\beta), D_u^k f(\sigma)\rangle_{\mathbb{S}^{n-1}}.\end{aligned}$$

□

We note that (4.18) is equivalent to

$$\int_0^\pi C^k f(u,\beta,\psi) h(\cos\psi) d\psi = \int_{\mathbb{S}^{n-1}} D_u^k f(\sigma) h(\sigma\cdot\beta) d\sigma. \tag{4.19}$$

Definition 4.3.2. Let $k < n-1$. We introduce the following distribution:

$$\begin{aligned} h_{n,k}(t) &:= \int_0^\infty e^{-its} s^{n-k-2} ds \\ &= i^{n-k-1}[(n-k-2)! t^{k-n+1} + (-1)^{n-k-1} i\pi \delta^{(n-k-2)}(t)],\end{aligned} \tag{4.20}$$

(see e.g. [17, Chapter 2, p.172, eqn. (5)]).

Proposition 4.3.3. *The following identity holds:*

$$\widehat{D_u^k f}(\xi) = \int_{\mathbb{S}^{n-1}} D_u^k f(\sigma) h_{n,k}(\sigma\cdot\xi) d\sigma. \tag{4.21}$$

Proof. For each $\varphi \in \mathcal{S}(\mathbb{R}^n)$, since $D_u^k f$ is homogeneous of degree $-(k+1)$, we have

$$\begin{aligned}
\langle \widehat{D_u^k f}, \varphi \rangle = \langle D_u^k f, \hat{\varphi} \rangle &= \int_{\mathbb{R}^n} D_u^k f(y) \hat{\varphi}(y) dy \\
&= \int_{\mathbb{S}^{n-1}} \int_0^\infty D_u^k f(\sigma) \hat{\varphi}(s\sigma) s^{n-k-2} ds d\sigma \\
&= \int_{\mathbb{S}^{n-1}} \int_0^\infty D_u^k f(\sigma) \int_{\mathbb{R}^n} e^{-is\sigma\cdot\xi} \varphi(\xi) d\xi s^{n-k-2} ds d\sigma \\
&= \int_{\mathbb{R}^n} \int_{\mathbb{S}^{n-1}} D_u^k f(\sigma) h_{n,k}(\sigma \cdot \xi) d\sigma \varphi(\xi) d\xi,
\end{aligned}$$

which implies (4.21). □

Now, by combining (4.19) and (4.21), and using the inversion formula for the weighted divergent beam transform (4.8), we obtain an inversion formula for the weighted cone transform.

Theorem 4.3.4. *Let $f \in \mathcal{S}(\mathbb{R}^n)$, and $k < n-1$. Then,*

$$f(x) = \frac{(-i)^{k+1}}{(2\pi)^n} \int_{\mathbb{S}^{n-1}} \int_0^\pi \left(\Delta_u^{(k+1)/2} C^k f(u, \beta, \psi) \right) \Big|_{u=x} h_{n,k}(\cos\psi) d\psi d\beta. \tag{4.22}$$

Remark 4.3.5. The same deficiency applies here that was mentioned in remark 4.2.2: the formula requires the cones to be available with all vertices u throughout the space, which is unacceptable for many imaging applications (e.g. Compton ones). Fortunately, a similar remedy as for the divergent beam transform exists, which we address next.

Theorem 4.3.6. *Let $k \in \mathbb{Z}_+, k < n-1$. Suppose that $\mathcal{M} \subset \mathbb{R}^n$ satisfies the Tuy's condition with respect to a compact $V \subset \mathbb{R}^n$, and f is a smooth function supported in V. Then, depending on the parity of k, the following inversion formulas hold:*

1. *if k is odd, then for any homogeneous linear elliptic differential operator $L(u, \partial_u)$ of*

order $k+1$ on $\mathcal{M}$

$$f(x) = \frac{1}{(2\pi)^n} \int_{\mathbb{S}^{n-1}} \int_0^\pi \frac{1}{L(u, P_u\theta)} L(u, \partial_u) C^k f(u, \theta, \psi) h_{n,k}(\cos\psi) d\psi d\theta, \quad (4.23)$$

2. *if k is even, then for any homogeneous linear elliptic differential operator $L(u, \partial_u)$ of order k on $\mathcal{M}$*

$$f(x) = \frac{1}{(2\pi)^n} \int_{\mathbb{S}^{n-1}} \int_0^\pi \frac{1}{|P_u\theta|^2} \big(O \circ \frac{1}{L(u, P_u\theta)} L\big) C^k f(u, \theta, \psi) h_{n,k}(\cos\psi) d\psi d\theta, \quad (4.24)$$

where O is given as in (4.15)*, and $u \in \mathcal{M}$ is related to x and θ as in the Tuy's condition.*

Proof. The proof is just an immediate consequence of the equalities (4.21), (4.19), (4.13), and (4.17) (in that order). □

4.4 Relations with the Radon Transform: Other Inversion Formulas

In this section, we first present a relation between the Radon and the weighted divergent beam and cone transforms for any dimension n and any $k \in \mathbb{Z}_+$. Analogous relation for the usual divergent beam transform ($k = 0$) is obtained in [25] (see also [64, Chapter 2]).

Proposition 4.4.1. *Let $f \in \mathcal{S}(\mathbb{R}^n)$ and h be a distribution on $\mathbb{R}$ which is homogeneous of degree $k - n + 1$ and regular around ± 1. Then,*

$$\begin{aligned} &\int_0^\pi C^k f(u, \beta, \psi) h(-\cos\psi) d\psi \quad (4.25) \\ &= \int_{\mathbb{S}^{n-1}} D_u^k f(\sigma) h(-\sigma \cdot \beta) d\sigma = \int_{\mathbb{R}} Rf(\beta, s) h(u \cdot \beta - s) ds = (R_\beta f * h)(u \cdot \beta). \end{aligned}$$

Proof. The first equality is already obtained in Proposition 4.3.1. By definition of the

weighted divergent beam transform, we have

$$\begin{aligned}\int_{\mathbb{S}^{n-1}} D_u^k f(\sigma) h(-\sigma\cdot\beta)d\sigma &= \int_{\mathbb{S}^{n-1}}\int_0^\infty f(u+\rho\sigma)\rho^k d\rho h(-\sigma\cdot\beta)d\sigma \\ &= \int_{\mathbb{S}^{n-1}}\int_0^\infty f(u+\rho\sigma)h(-\rho\sigma\cdot\beta)\rho^{n-1}d\rho d\sigma,\end{aligned}$$

due to the homogeneity of h. Letting $x = u+\rho\sigma$, we obtain

$$\begin{aligned}&\int_{\mathbb{S}^{n-1}}\int_0^\infty f(u+\rho\sigma)h(-\rho\sigma\cdot\beta)\rho^{n-1}d\rho d\sigma \\ &\quad= \int_{\mathbb{R}^n} f(x)h((u-x)\cdot\beta)dx = \int_{\mathbb{R}^n} f(x)\left(\int_{\mathbb{R}} h(u\cdot\beta-s)\delta(x\cdot\beta-s)ds\right)dx \\ &\quad= \int_{\mathbb{R}}\left(\int_{\mathbb{R}^n} f(x)\delta(x\cdot\beta-s)dx\right)h(u\cdot\beta-s)ds = \int_{\mathbb{R}} Rf(\beta,s)h(u\cdot\beta-s)ds.\end{aligned}$$

□

Remark 4.4.2. In dimensions two and three, for $k = 0$ and $k = 1$, respectively, the relation (4.25) gives the following (geometrically obvious) formula:

$$C^k f(u,\beta,\frac{\pi}{2}) = R(\beta, u\cdot\beta),$$

which is used in [6] in dimension three.

Remark 4.4.3. In dimension three, a special case of (4.25), namely for $h(t) = t^{k-2}$, is proven and used to derive an inversion formula for the cone transform for $k = 0$ and $k = 1$ in [57]. In dimension two, an inversion formula for $k = 0$ is derived using (4.25) with $h(t) = t^{-1}$ in [1, 18]. For the usual divergent beam transform ($k = 0$) in dimension three, the applications of various functions h can be found in [64, Chapter 2, and references therein].

Let $k \in \mathbb{Z}_+$, and h be the function on $\mathbb{R}$ defined by

$$h(t) := \begin{cases} \dfrac{1}{2(k-n+1)!}|t|^{k-n+1}\text{sgn } t, & \text{if } k > n-2 \text{ and } k-n \text{ is odd,} \\ \dfrac{1}{2(k-n+1)!}|t|^{k-n+1}, & \text{if } k > n-2 \text{ and } k-n \text{ is even,} \\ \delta^{(n-k-2)}(t), & \text{if } k \leq n-2. \end{cases} \tag{4.26}$$

We note that h is homogeneous of degree $k-n+1$, and for $k > n-2$, $h^{(k-n+2)} = \delta(t)$ (see e.g. [17]).

Now, using the differentiation property of the convolution

$$\partial^\alpha (g * h) = \partial^\alpha g * h = g * \partial^\alpha h$$

and the inversion formula (B.18) for the Radon transform, we obtain the following formula, which can be used for inversion of both the weighted divergent beam and cone transforms:

Theorem 4.4.4. *Suppose that for any $u \in \mathcal{M}$ and $\beta \in \mathbb{S}^{n-1}$, $s = u \cdot \beta$ and*

$$\begin{aligned} G(\beta, s) := (R_\beta f * h)(s) &= \int_0^\pi C^k f(u, \beta, \psi) h(-\cos\psi) d\psi \\ &= \int_{\mathbb{S}^{n-1}} D_u^k f(\sigma) h(-\sigma \cdot \beta) d\sigma. \end{aligned} \tag{4.27}$$

Then, for any $f \in \mathcal{S}(\mathbb{R}^n)$,

$$f(x) = \frac{1}{2}(2\pi)^{1-n} \begin{cases} (-1)^{(n-1)/2} \displaystyle\int_{\mathbb{S}^{n-1}} G^{(k+1)}(\beta, x \cdot \beta)\, d\beta, & \textit{if } n \textit{ is odd,} \\ (-1)^{(n-2)/2} \displaystyle\int_{\mathbb{S}^{n-1}} \mathcal{H} G^{(k+1)}(\beta, x \cdot \beta)\, d\beta, & \textit{if } n \textit{ is even,} \end{cases} \tag{4.28}$$

where $G^{(k+1)}$ is the $(k+1)$-st derivative of G with respect to s, h is given in (4.26)*, and*

$\mathcal{H}$ is the Hilbert transform (B.19) *with respect to s.*

Proof. Using h given in (4.26) for $k \geq n-2$, we have

$$(R_\beta f * h)^{(k+1)} = (R_\beta f)^{(n-1)} * h^{(k-n+2)} = (R_\beta f)^{(n-1)} * \delta = (R_\beta f)^{(n-1)},$$

and for $k < n-2$, we get

$$(R_\beta f * h)^{(k+1)} = (R_\beta f * \delta^{(n-k-2)})^{(k+1)} = (R_\beta f)^{(n-1)}.$$

Hence, the application of Radon transform inversion (B.18) gives the result. □

Remark 4.4.5. The reconstruction formula (4.28) is independent of the geometry of the manifold $\mathcal{M}$ that u belongs to. Indeed, for the weighted cone transform, it is sufficient that for any $s \in \mathbb{R}$ and $\beta \in \mathbb{S}^{n-1}$, there is a vertex $u = s\beta + y$, where $y \perp \beta$, and the weighted cone data is available at all angles ψ for these u and β. In other words, the requirement for the reconstruction is that any hyperplane intersecting the domain of reconstruction contains the vertex of a cone with the axis normal to the plane and all opening angles.

For the weighted divergent beam transform, the corresponding condition is that for any $s \in \mathbb{R}$ and $\beta \in \mathbb{S}^{n-1}$, there is a source $u = s\beta + y$, where $y \perp \beta$, and the weighted divergent beam data is available at all directions σ for this source u.

4.5 Reconstruction Algorithms and Numerical Implementation Results

In this section, we present the results of numerical implementation of Theorem 4.4.4. In dimension two, the weighted cone transform and divergent beam transforms are similar, so we only provide examples for the weighted cone transform for $k = 1$ using two different vertex geometries. We then give the reconstruction results for the weighted cone transform in dimension three for $k = 0$ and $k = 2$ using a spherical vertex geometry. Examples showing the reaction of the algorithms to Gaussian white noise in the data are also

provided. We also present an example of numerical inversion of the weighted divergent beam transform in dimension three for the cases $k = 1$ and $k = 2$ using a spherical source geometry.

All phantoms are placed off-center of the vertex curve/surface, to avoid unintended use of rotational invariance. Care was taken to avoid other possibilities of committing an inverse crime, by making the forward and inverse algorithms as unrelated as possible.

ALGORITHM Numerical Implementation of (4.28)

Data: $c_{i,j,k} = Cf(u_i, \beta_j, \psi_k)$, $i = 1, ..., U$, $j = 1, ..., B$, $k = 1, ..., P$.

1: For $i = 1, ..., U$, $j = 1, ..., B$ compute

$$G(\beta_j, u_i \cdot \beta_j) := \sum_{k=1}^{P} c_{i,j,k} h(-\cos\psi_k)\Delta\psi \sim \int_0^{\pi} Cf(u, \beta, \psi) h(-\cos\psi) d\psi.$$

2: Carry out 1D interpolation to obtain $G(\omega_j, s_k)$ for a uniform mesh $\{s_k\}$ on $[-1, 1]$.

3: For $i = 1, ..., U$, and $j = 1, ..., B$, differentiate G with respect to s $(k + 1)$-times, and if n is even, compute $\mathcal{H}G^{(k+1)}$ using Fourier spectral method.

4: For each reconstruction point $x_{i,j,l} \in [-1, 1]^3$, find $G^{(k+1)}(x_{i,j,l} \cdot \beta, \beta)$ (if n is even, $\mathcal{H}G^{(k+1)}(x_{i,j,l} \cdot \beta, \beta)$) by interpolating $G(\omega_j, s_k)$.

5: Carry out the integration

$$f_{i,j,l} = \sum_{\tau \in K} \frac{Area(\tau)}{6(2\pi)^{n-1}} \sum_{v \in V(\tau)} G^{(k+1)}(v, x_{i,j,l} \cdot v) \sim \frac{(2\pi)^{1-n}}{2} \int_{\mathbb{S}^{n-1}} G^{(k+1)}(\beta, x \cdot \beta) d\beta,$$

where τ is a face of the triangular mesh K on $\mathbb{S}^2$, and $V(\tau)$ is the set of vertices of τ.

Result: $f_{i,j,l}$ is an approximation to the phantom f which is supported on the unit sphere.

4.5.1 2D Image Reconstruction from Weighted Cone Data

In dimension two, for $k = 0$, the relation (4.25) gives $C^0(u, \beta, \pi/2) = Rf(\beta, u \cdot \beta)$, which is geometrically obvious (also see [6]). Thus, we focus here on the case $k = 1$ only. Since a cone in 2D is represented by two rays with a common vertex, the weighted cone transform for $k = 1$ is given by

$$\begin{aligned} &C^1 f(u, \beta(\phi), \psi) \\ &\quad = \int_0^\infty [f(u + r(\cos(\phi - \psi), \sin(\phi - \psi)) + f(u + r(\cos(\phi + \psi), \sin(\phi + \psi))] r dr, \end{aligned}$$

where $\beta(\phi) = (\cos(\phi), \sin(\phi))$. The inversion formula (4.28) now reads as

$$f(x) = \frac{-1}{8\pi} \int_{\mathbb{S}^1} \Big(\mathcal{H} \frac{\partial^2}{\partial s^2} \int_0^\pi C^1 f(s\beta + y, \beta, \psi) \text{sgn}(\cos\psi) d\psi \Big) \Big|_{s = x \cdot \beta} d\beta. \tag{4.29}$$

For the numerical implementation of (4.29), we considered the phantom

$$f = \chi_{D_1} - 0.5 \chi_{D_2},$$

where D_1 and D_2 are the concentric disks centered at $(0, 0.4)$ with radii 0.25 and 0.5, respectively. Here, χ_{D_i} denotes the characteristic function of each disk (see Fig. 4.2). The cone projection data of the phantom f is simulated numerically using 256 counts for vertices u, 400 counts for central axis directions β and 90 counts for opening angles ψ.

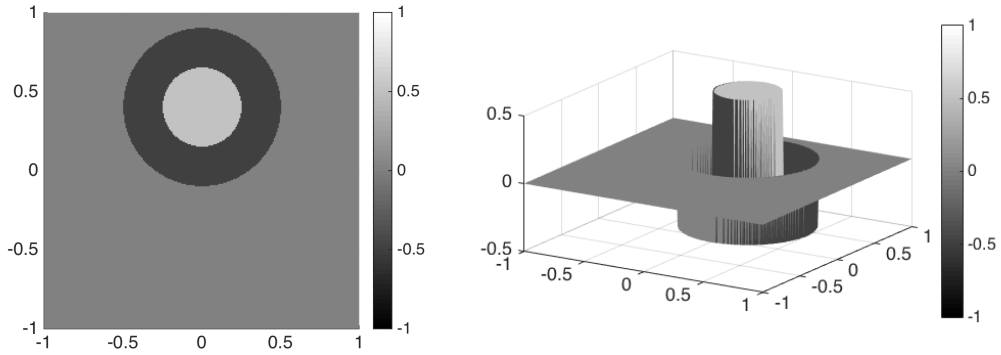

Figure 4.2: The density plot (left) and surface plot (right) of the phantom f that consists of two concentric disks centered at $(0, 0.4)$ with radii 0.25 and 0.5, and densities 1 and -0.5 units, respectively.

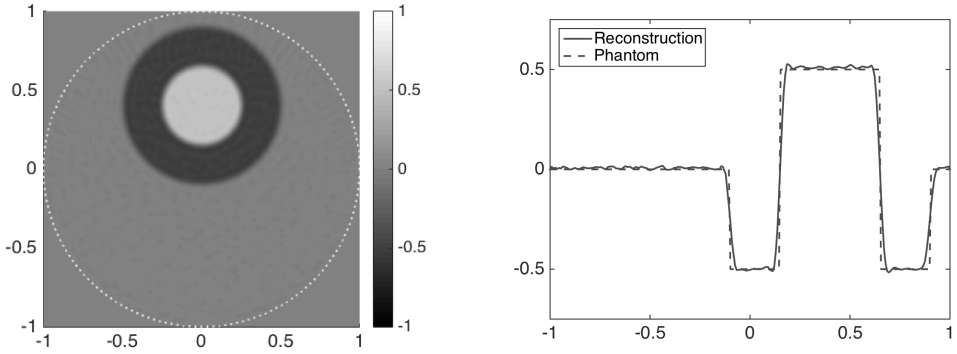

Figure 4.3: The density plot of 256×256 image reconstructed from the simulated cone data using 256 counts for vertices u (represented by white dots on the unit circle), 400 counts for directions β and 90 counts for opening angles ψ (left), and the comparison of y-axis profiles of the phantom and the reconstruction (right).

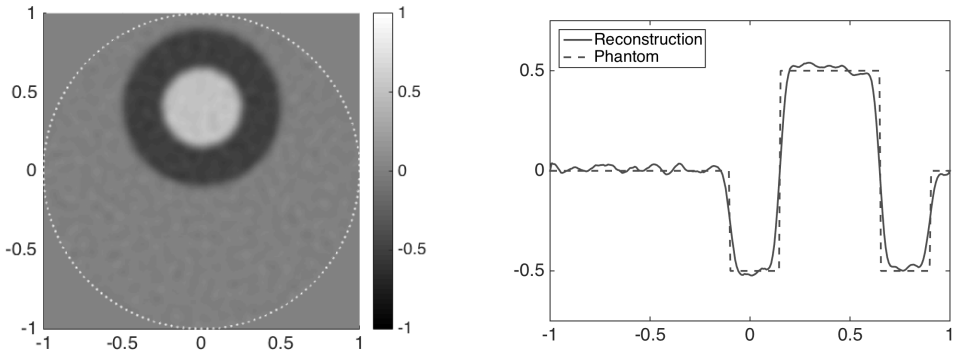

Figure 4.4: The density plot of 256×256 image reconstructed from cone data contaminated with 5% Gaussian noise (left), and the comparison of y-axis profiles of the phantom and the reconstruction (right). The dimensions of the cone data are taken as in Fig. 4.3.

As our inversion formula is valid for arbitrary geometry of vertices, we considered both a circular and a square geometry of vertices of the cones.

Figure 4.3 shows the results of reconstruction from cone projections where the vertices cover the unit circle. The density plot and the y-axis profile of the reconstruction are provided in (a) and (b), respectively. The results with a 5% Gaussian white noise added to the cone data is shown in Figure 4.4.

In Figure 4.5, we provide the results of reconstruction from cone projections where the vertices are placed along the sides of a square with sides of length two. The density plot and the y-axis profile of the reconstruction are provided in Figure 4.5 (a) and (b), respectively. Figure 4.6 shows the results with a 5% Gaussian white noise added to the cone data.

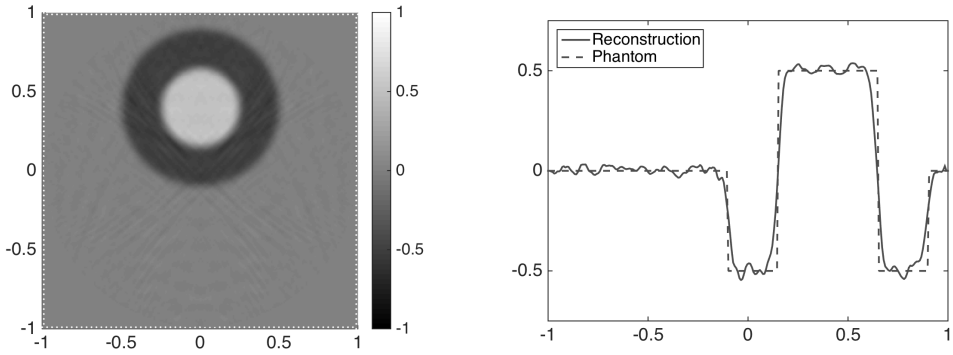

Figure 4.5: The density plot of 256×256 image reconstructed from the simulated cone data using 256 counts for vertices u (represented by white dots around the square), 400 counts for directions β and 90 counts for opening angles ψ (left), and the comparison of y-axis profiles of the phantom and the reconstruction (right).

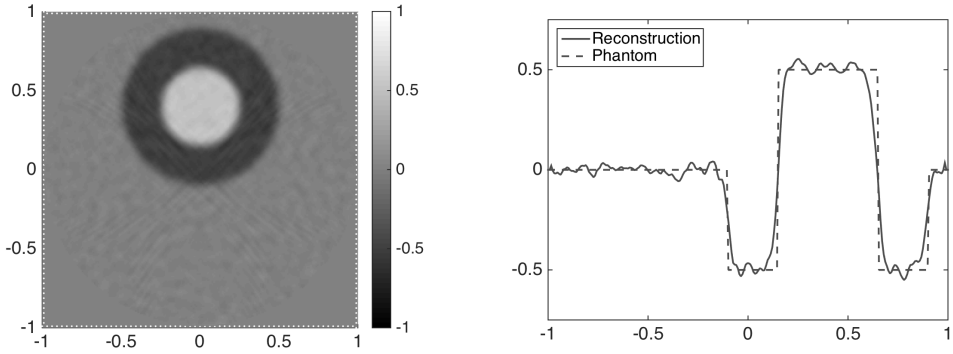

Figure 4.6: The density plot of 256×256 image reconstructed from cone data contaminated with 5% Gaussian noise (left), and the comparison of y-axis profiles of the phantom and the reconstruction (right). The dimensions of the cone data are taken as in Fig. 4.5.

In the case of the square geometry (but not in the circular one), some corner-related effects appear along the diagonals, as shown in Figure 4.7. They can be eliminated by

using a finer discretization in β.

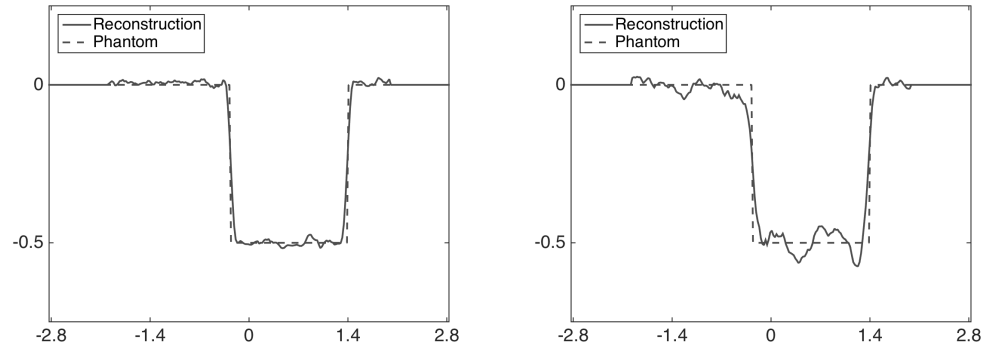

Figure 4.7: Comparison of the profiles of the reconstruction along the diagonal of the square region for the circular (left) and square (right) locations of the vertices (detectors).

4.5.2 3D Image Reconstruction from Weighted Cone Data

In dimension three, the relation (4.25) is geometrically obvious for the case k=1 (see remark 4.2), and is numerically implemented in [6] using spherical harmonic expansions. Here, we provide examples of reconstruction from the weighted cone data for $k = 0$ and $k = 2$. Theorem 4.4.4 gives the following inversion formula for $k = 0$:

$$\begin{aligned} f(x) &= \frac{1}{8\pi^2} \int_{\mathbb{S}^2} \Big(\frac{\partial}{\partial s} \int_0^{\pi} C^0 f(s\beta + y, \beta, \psi) \delta'(\cos\psi) d\psi \Big) \Big|_{s=x\cdot\beta} d\beta \\ &= \frac{-1}{8\pi^2} \int_{\mathbb{S}^2} \Big(\frac{\partial}{\partial s} \Big(\frac{\partial}{\partial t} C^0 f(s\beta + y, \beta, t) \Big) \Big|_{t=0} \Big) \Big|_{s=x\cdot\beta} d\beta, \end{aligned} \tag{4.30}$$

and for $k = 2$, we have

$$f(x) = \frac{-1}{16\pi^2} \int_{\mathbb{S}^2} \Big(\frac{\partial^3}{\partial s^3} \int_0^{\pi} C^2 f(s\beta + y, \beta, \psi) \mathrm{sgn}(\cos\psi) d\psi \Big) \Big|_{s=x\cdot\beta} d\beta. \tag{4.31}$$

In our examples, the vertices of the cones cover the unit sphere $\mathbb{S}^2$ in $\mathbb{R}^3$ and the phantom is the characteristic function of the 3D ball of radius 0.5 units located strictly inside and off-center of this sphere.

The forward simulations of weighted cone projections were done numerically using 1800 counts for vertices u on the unit sphere, 1800 counts for unit vectors for the cone axis directions β and 200 counts for opening angles ψ. For the discretization of the sphere, we used a uniform mesh for both the azimuthal and the polar angles.

Figure 4.8 shows the three cross sections of the spherical phantom and of its reconstructions from the cone data obtained via (4.30). The comparison of the phantom and the reconstruction given in Figure 4.8 in terms of their coordinate axis profiles is provided in Figure 4.9.

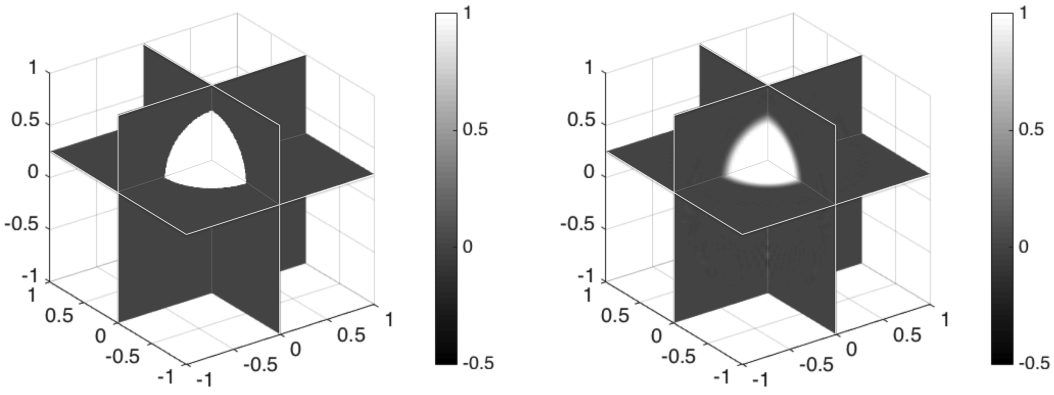

Figure 4.8: The 3D ball phantom with radius 0.5, center (0,0,0.25) and unit density (left), and 90×90 image reconstructed via (4.30) from weighted cone data simulated using 1800 counts for vertices u on the unit sphere, 1800 counts for directions β and 200 counts for opening angles ψ (right). The cross sections by the planes $x = 0, y = 0$ and $z = 0.25$ are shown.

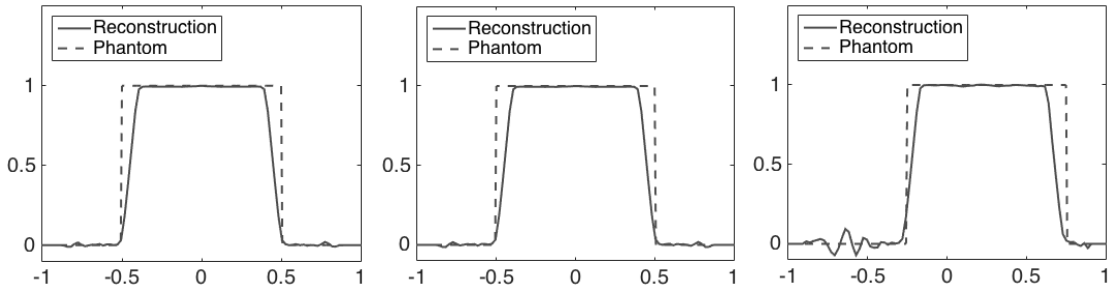

Figure 4.9: Comparison of the x-axis (left), y-axis (center) and z-axis (right) profiles of the reconstruction and the phantom given in Fig. 4.8.

Figure 4.10 shows the three cross sections of the spherical phantom and of its reconstructions from the cone data obtained via (4.31). The comparison of the phantom and the reconstruction given in Figure 4.10 in terms of their coordinate axis profiles is provided in Figure 4.11.

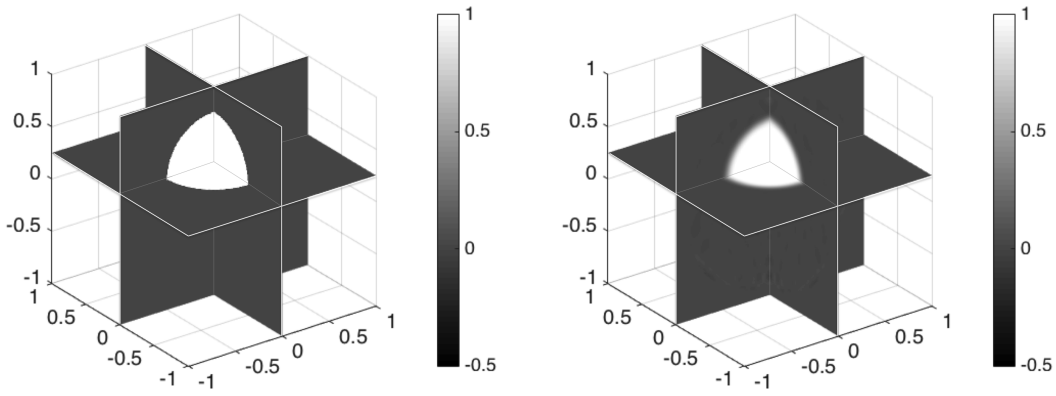

Figure 4.10: The 3D ball phantom with radius 0.5, center (0,0,0.25) and unit density (left), and 90×90 image reconstructed via (4.31) from weighted cone data simulated using 1800 counts for vertices u on the unit sphere, 1800 counts for directions β and 200 counts for opening angles ψ (right). The cross sections by the planes $x = 0, y = 0$ and $z = 0.25$ are shown.

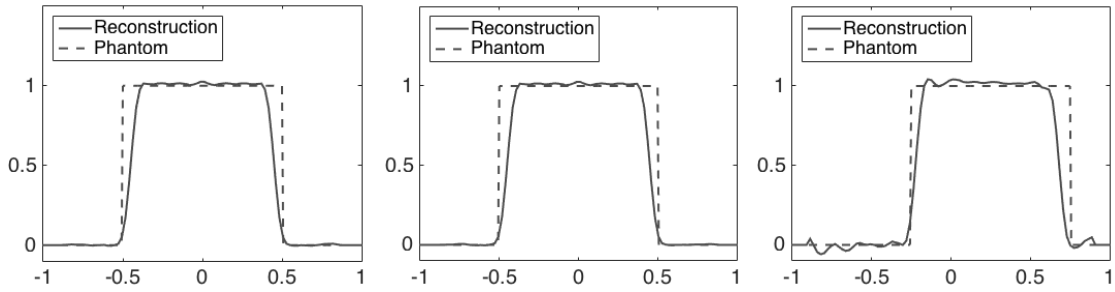

Figure 4.11: Comparison of the x-axis (left), y-axis (center) and z-axis (right) profiles of the reconstruction and the phantom given in Fig. 4.10.

Figures 4.12 and 4.13 show the results of reconstruction from weighted cone data for $k = 2$ contaminated with 5% Gaussian white noise.

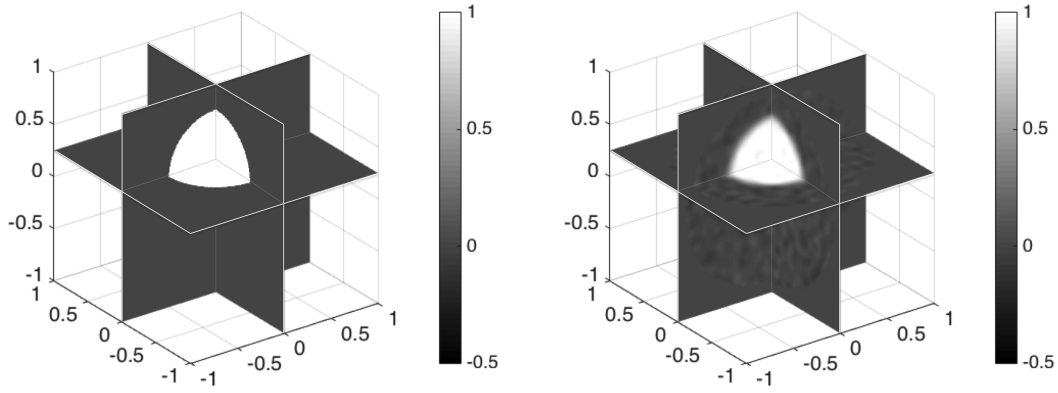

Figure 4.12: The 3D ball phantom with radius 0.5, center (0,0,0.25) and unit density (left), and 90×90 image reconstructed via (4.31) from weighted cone data contaminated with 5% Gaussian white noise (right). The dimensions of the cone projections are taken as in Fig. 4.10. The cross sections by the planes $x = 0, y = 0$ and $z = 0.25$ are shown.

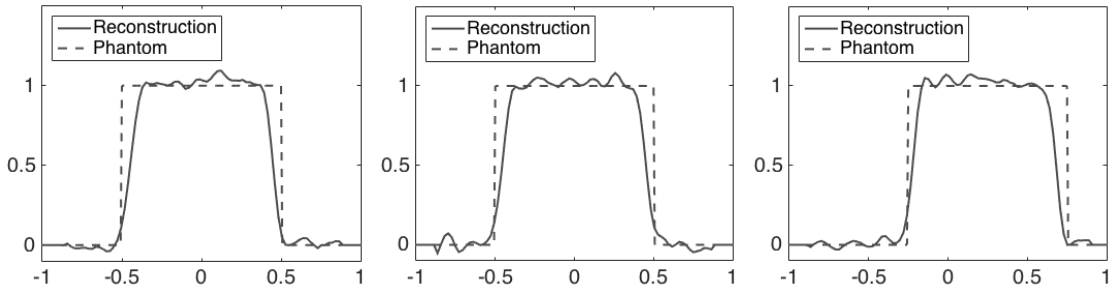

Figure 4.13: Comparison of the x-axis (left), y-axis (center) and z-axis (right) profiles of the reconstruction and the phantom given in Fig. 4.12.

4.5.3 3D Image Reconstruction from Weighted Divergent Beam Data

In dimension three, when $k = 0$, Theorem 4.4.4 reduces to Grangeat's formula [22]. Here, we provide examples of reconstruction from the weighted divergent beam data for $k = 1$ and $k = 2$ using a spherical source geometry. For $k = 1$, Theorem 4.4.4 gives the following inversion formula:

$$f(x) = \frac{1}{8\pi^2} \int\limits_{\mathbb{S}^2} \Big(\frac{\partial^2}{\partial s^2} \int\limits_{\mathbb{S}^2} D^1 f(s\beta + y, \sigma) \delta(\sigma \cdot \beta) d\sigma \Big) \Big|_{s=x\cdot\beta} d\beta, \tag{4.32}$$

and for $k = 2$, we have

$$f(x) = \frac{-1}{16\pi^2} \int\limits_{\mathbb{S}^2} \Big(\frac{\partial^3}{\partial s^3} \int\limits_{\mathbb{S}^2} D^2 f(s\beta + y, \sigma) \mathrm{sgn}(\sigma \cdot \beta) d\sigma \Big) \Big|_{s=x\cdot\beta} d\beta. \tag{4.33}$$

The forward simulations of weighted divergent beam projections were done numerically using 1800 counts for sources u on the unit sphere, 30K counts for unit directions σ. For the triangulation of the sphere, we used the algorithm given in [50].

Figure 4.14 shows the three cross sections of the spherical phantom and of its reconstructions from the weighted divergent beam data obtained via (4.32). The comparison of

the phantom and the reconstruction given in Figure 4.14 in terms of their coordinate axis profiles is provided in Figure 4.15.

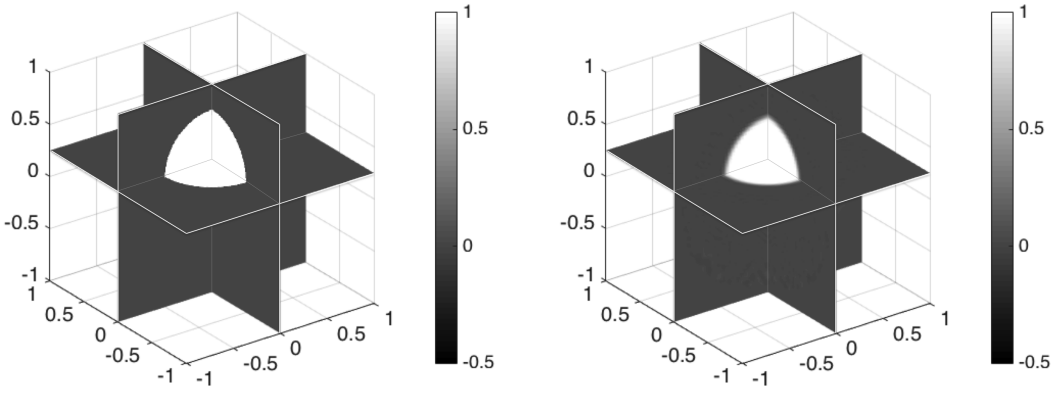

Figure 4.14: The 3D ball phantom with radius 0.5, center (0,0,0.25) and unit density (left), and 90×90 image reconstructed via (4.32) from weighted divergent beam data simulated using 1800 counts for sources u on the unit sphere and 30K counts for unit directions σ (right). The cross sections by the planes $x = 0, y = 0$ and $z = 0.25$ are shown.

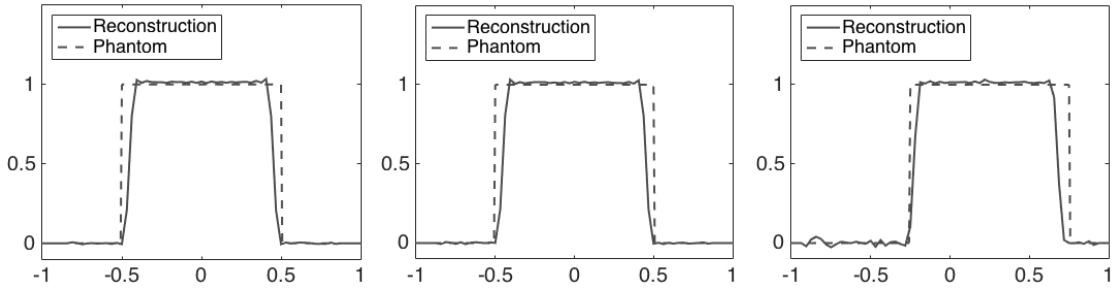

Figure 4.15: Comparison of the x-axis (left), y-axis (center) and z-axis (right) profiles of the phantom and the reconstruction given in Fig. 4.14.

Figure 4.16 shows the three cross sections of the spherical phantom and of its recon-

structions from the weighted divergent beam data obtained via (4.33). The comparison of the phantom and the reconstruction given in Figure 4.16 in terms of their coordinate axis profiles is provided in Figure 4.17.

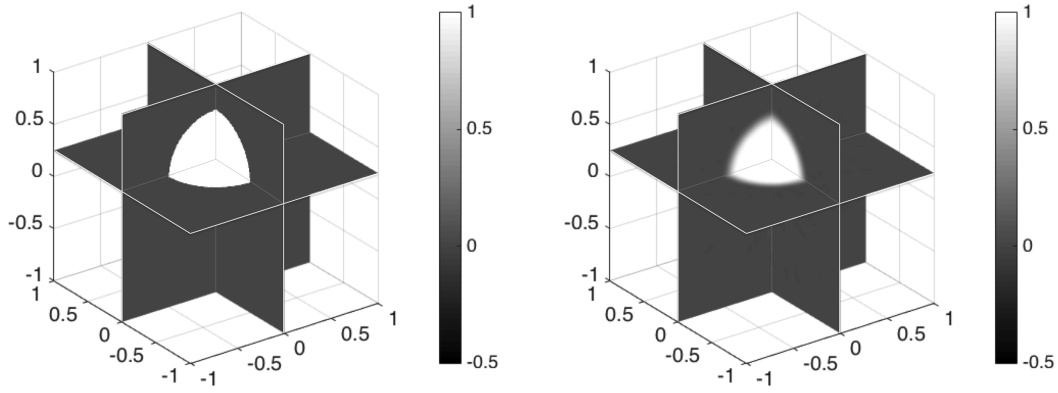

Figure 4.16: The 3D ball phantom with radius 0.5, center (0,0,0.25) and unit density (left), and 90×90 image reconstructed via (4.33) from weighted divergent beam data simulated using 1800 counts for sources u on the unit sphere and 30K counts for unit directions σ (right). The cross sections by the planes $x = 0, y = 0$ and $z = 0.25$ are shown.

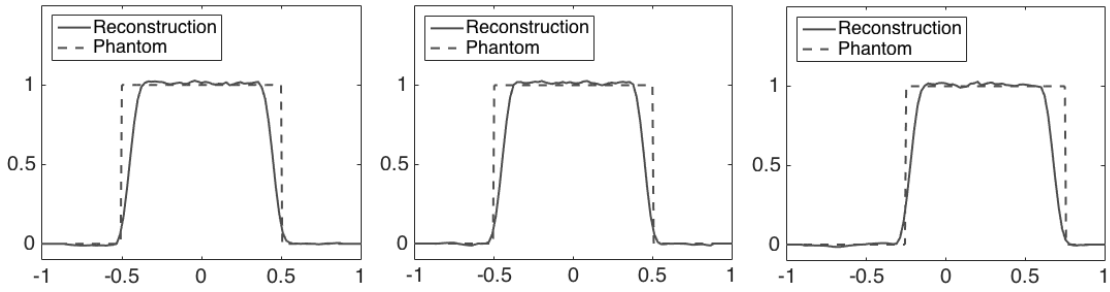

Figure 4.17: Comparison of the x-axis (left), y-axis (center) and z-axis (right) profiles of the reconstruction and the phantom given in Fig. 4.16.

5. FURTHER PROPERTIES OF THE WEIGHTED CONE TRANSFORM

In this chapter, we present some further results about the weighted cone transform. In Section 5.1, we derive identities that relate spherical harmonic expansion coefficients of the weighted cone transform with the weighted divergent beam transform and the Radon transform. Then, we provide a range condition for the weighted cone transform in Section 5.2. In Section 5.3 we present the dual operator to the weighted cone transform, and prove in Section 5.4 that the normal operator is a classical pseudo-differential operator.

5.1 Spherical Harmonic Expansions

Let us fix a vertex (source, detector) location u. Then cones with the vertex u are in one-to-one correspondence with the $(n-2)$-dimensional spheres on the unit $(n-1)$-dimensional sphere centered at u, the correspondence being given by intersecting a cone with the unit sphere. Analogously, rays (divergent beams) emanating from u correspond to the points on this unit sphere. It is clear then that the (weighted) cone data with the vertex u is the "Radon" transform over the $(n-2)$-dimensional spheres of the correspondingly weighted divergent beam transform data. Since the transform that integrates over these spheres is rotationally invariant, it is natural to use spherical harmonics expansion in the hope of relating the two types of data. This is exactly what we plan to do in this section: find a relation between spherical harmonic expansion coefficients of the weighted cone and divergent beam transforms.

We can expand $C^k f(u,\beta,t)$ and $D_u^k f(\sigma)$ in spherical harmonics as follows:

$$D_u^k f(\sigma) \sim \sum_{l=0}^{\infty} \sum_{m=0}^{N(n,l)} d_{l,m}^k(u) Y_{l,m}(\sigma) \tag{5.1}$$

and

$$C^k f(u,\beta,t) \sim \sum_{l=0}^{\infty} \sum_{m=0}^{N(n,l)} c_{l,m}^k(u,t) Y_{l,m}(\beta), \tag{5.2}$$

where $Y_{l,m}$ is the spherical harmonic of degree l and order m (see Appendix B.1.3),

$$N(n,l) = (n+2l-2)\frac{(n+l-3)!}{l!(n-2)!}, \tag{5.3}$$

$$d_{l,m}^k(u) = \int_{\mathbb{S}^{n-1}} D_u^k f(\sigma) Y_{l,m}(\sigma) d\sigma, \tag{5.4}$$

and

$$c_{l,m}^k(u,t) = \int_{\mathbb{S}^{n-1}} C^k f(u,\beta,t) Y_{l,m}(\beta) d\beta. \tag{5.5}$$

The following theorem gives a relation between spherical harmonic expansion coefficients (5.4) and (5.5) of the weighted divergent beam and cone transforms, respectively. This relation for $k = 1$ in dimension three was provided in [6].

Theorem 5.1.1. *Let $P_l^\lambda(t)$ be the Gegenbauer (ultraspherical) polynomials of degree l, $\lambda > -1/2$ (see Appendix B.1.2). Then, for any $u \in \mathbb{R}^n$,*

$$c_{l,m}^k(u,t) = \begin{cases} |S^{n-2}|(1-t^2)^{(n-2)/2} P_l^{(n-2)/2}(t) d_{l,m}^k(u), & |t| \le 1 \\ 0, & |t| > 1. \end{cases} \tag{5.6}$$

Proof. In view of (4.4), it is clear that $c_{l,m}^k(u,t) = 0$ when $|t| > 1$. For $|t| \le 1$, we can

write

$$\begin{aligned} c_{l,m}^k(u,t) &= \int_{\mathbb{S}^{n-1}} C^k f(u,\beta,t) Y_{l,m}(\beta) d\beta \\ &= \sqrt{1-t^2} \int_{\mathbb{S}^{n-1}} \int_{\mathbb{S}^{n-1}} D_u^k f(\sigma) \delta(\sigma\cdot\beta - t) d\sigma \; Y_{l,m}(\beta) d\beta \\ &= \sqrt{1-t^2} \int_{\mathbb{S}^{n-1}} D_u^k f(\sigma) \int_{\mathbb{S}^{n-1}} \delta(\sigma\cdot\beta - t) Y_{l,m}(\beta) d\beta \; d\sigma. \end{aligned}$$

Here, we can apply Funk-Hecke formula (see Theorem B.1.1) to obtain

$$\int_{\mathbb{S}^{n-1}} \delta(\sigma\cdot\beta - t) Y_{l,m}(\beta) d\beta = |S^{n-2}|(1-t^2)^{(n-3)/2} P_l^{(n-2)/2}(t) Y_{l,m}(\sigma).$$

Hence,

$$c_{l,m}^k(u,t) = |S^{n-2}|(1-t^2)^{(n-2)/2} P_l^{(n-2)/2}(t) \int_{\mathbb{S}^{n-1}} D_u^k f(\sigma) Y_{l,m}(\sigma) d\sigma,$$

which implies (5.6). □

When $k = n-2$, we can use the relation of the cosine transform with spherical harmonics to find a relation between the spherical harmonic expansion coefficients of the cone and Radon transforms.

Lemma 5.1.2. *Let $g \in L^1(S^{n-1})$. Then,*

$$\int_{S^{n-1}} \int_0^\pi Cf(u,\beta,\psi) g(\beta) \sin\psi d\psi d\beta = \pi \int_{S^{n-1}} Rf(\omega, \omega\cdot u) \mathfrak{C} g(\omega) d\omega. \tag{5.7}$$

Proof. Multiplying both sides of (3.10) with $g(\beta)$ and integrating with respect to β over

S^{n-1}, we have

$$\int_{S^{n-1}} \int_0^{\pi} Cf(u,\beta,\psi)g(\beta)\sin\psi d\psi d\beta = \frac{\pi}{|S^{n-1}|} \int_{S^{n-1}} Rf(\omega,\omega\cdot u) \int_{S^{n-1}} g(\beta)|\omega\cdot\beta| d\beta d\omega$$
$$= \pi \int_{S^{n-1}} Rf(\omega,\omega\cdot u)\mathfrak{C}g(\omega)d\omega.$$

□

The spherical harmonics are known to be the eigenfunctions of the cosine transform. This follows from the Funk-Hecke Formula (B.1.1).

Corollary 5.1.3. *For every spherical harmonic Y_l of degree l, $l = 0, 1, 2, ...$, and every $\omega \in S^{n-1}$,*

$$\mathfrak{C}Y_l(\omega) = \lambda_l Y_l(\omega) \tag{5.8}$$

where λ_l is given as in Funk-Hecke Formula (Theorem B.1.1) for $f(t) = |t|$.

Now, we can establish the following relation.

Proposition 5.1.4. *For every spherical harmonic Y_l of degree l,*

$$\int_{S^{n-1}} \int_0^{\pi} Cf(u,\beta,\psi)Y_l(\beta)\sin\psi d\psi d\beta = \pi\lambda_l \int_{S^{n-1}} Rf(\omega,\omega\cdot u)Y_l(\omega)d\omega. \tag{5.9}$$

In particular, for $l = 0$, we obtain (3.15)*.*

Proof. Letting $g = Y_l$ in (5.7), and using (5.8), we get (5.9). Then, the equation (3.15) follows from direct calculation. □

Remark 5.1.5. As the relation (5.9) gives the spherical harmonics coefficients of the function $Rf(\omega, u\cdot\omega)$, one can recover it for all $u \in \mathbb{R}^n$ and $\omega \in S^{n-1}$. Then, any inversion

formula for the Radon transform (B.16) would reconstruct the function f. This can be considered as an analog of Cormack's method [46].

5.2 A Range Condition

Theorem 5.2.1. *Suppose that $f \in \mathcal{S}(\mathbb{R}^n)$. For any $k \in \mathbb{Z}_+$ and $u \in \mathbb{R}^n$, the weighted cone transform $C_u^k f(\beta, t)$ satisfies the following differential equation.*

$$\left\{ a_2(n,t)\frac{\partial^2}{\partial t^2} + a_1(n,t)\frac{\partial}{\partial t} + a_0(n,t) + b(n,t)\Delta_S \right\} g(\beta,t) = 0 \quad \textit{on} \quad \mathbb{S}^{n-1} \times (-1,1)$$
$$g(\beta,-1) = g(\beta,1) = 0, \tag{5.10}$$

where

$$\begin{aligned} a_0(n,t) &= \frac{1}{2}(n-2)[(n-1)t - n], \\ a_1(n,t) &= -\frac{1}{2}(2t+n-2)(1-t^2), \\ a_2(n,t) &= (1-t^2)^2, \\ b(n,t) &= -(1-t^2). \end{aligned} \tag{5.11}$$

Proof. Let $\lambda = (n-2)/2$. It is well known that $P_l^\lambda(t)$ solves the following differential equation (see Appendix B.1.2):

$$(1-t^2)y'' - (n-1)ty' + l(l+2\lambda)y = 0. \tag{5.12}$$

Let $y(t) = P_l^\lambda(t)$, and $\tilde{y}(t) = (1-t^2)^\lambda y(t)$. Then, for $t \in (-1,1)$,

$$\begin{aligned}
&y(t) = (1-t^2)^{-\lambda}\tilde{y}(t),\\
&y'(t) = (1-t^2)^{-\lambda-1}\left[(1-t^2)\tilde{y}'(t) - \lambda\tilde{y}(t)\right], \qquad (5.13)\\
&y''(t) = (1-t^2)^{-\lambda-2}\left[(1-t^2)^2\tilde{y}''(t) - \lambda(2t-1)(1-t^2)\tilde{y}'(t) - 2\lambda(\lambda+1)t\tilde{y}(t)\right].
\end{aligned}$$

Plugging (5.13) in (B.6), we obtain

$$\begin{aligned}
&(1-t^2)^2\tilde{y}'' - (t+\lambda)(1-t^2)\tilde{y}'\\
&\qquad + \left[\lambda(2\lambda+1)t - 2\lambda(\lambda+1) + l(l+2\lambda)(1-t^2)\right]\tilde{y} = 0.
\end{aligned}$$

Then, (5.6) implies that for any $k \in \mathbb{Z}_+$ and $u \in \mathbb{R}^n$, $c_{l,m}^k(u,t)$ satisfies

$$\left\{a_2(n,t)\frac{\partial^2}{\partial t^2} + a_1(n,t)\frac{\partial}{\partial t} + a_0(n,t) + b(n,t)(-l)(l+n-2)\right\} c_{l,m}^k(u,t) = 0, \quad (5.14)$$

where $a_i(n,t), i = 0,1,2$, and $b(n,t)$ is as in (5.11). Now, since

$$\Delta_S Y_{l,m} = -l(l+n-2)Y_{l,m} \qquad l = 0,1,2,... \qquad (5.15)$$

we obtain

$$\left\{a_2(n,t)\frac{\partial^2}{\partial t^2} + a_1(n,t)\frac{\partial}{\partial t} + a_0(n,t) + b(n,t)\Delta_S\right\} c_{l,m}^k(u,t)Y_{l,m}(\beta) = 0, \qquad (5.16)$$

whose application in (5.2) implies the theorem. □

5.3 Dual Operator

Let $Z = \mathbb{R}^n \times \mathbb{S}^{n-1} \times (-1, 1)$, $w \in C_c^\infty(\mathbb{R}^n)$ be a weight function, and

$$L_w^2(Z) := \left\{ g : Z \to \mathbb{R} \quad | \quad ||g||_{L_w^2(Z)} = \left(\int_Z |g(u, \beta, t)|^2 \frac{w(u)}{1 - t^2} dt d\beta du \right)^{1/2} < \infty \right\}.$$

Theorem 5.3.1. *Let $C_\#^k$ be the operator defined on $L_w^2(Z)$ as*

$$\begin{aligned} C_\#^k g(x) &= \int_Z g(x - y, \beta, t) \delta(y \cdot \beta - |y|t) \frac{|y|^{k-n+2} w(x - y)}{\sqrt{1 - t^2}} dt d\beta dy \\ &= \int_{\mathbb{R}^n} \int_{S^{n-1}} g(x - y, \beta, \frac{y}{|y|} \cdot \beta) \frac{|y|^{k-n+1} w(x - y)}{\sqrt{1 - \left(\frac{y}{|y|} \cdot \beta \right)^2}} d\beta dy. \end{aligned} \tag{5.17}$$

Then, C^k, $C_\#^k$ form a dual pair, that is for $f \in \mathcal{S}(\mathbb{R}^n)$, we have

$$(C^k f, g)_{L_w^2(Z)} = (f, C_\#^k g)_{L^2(\mathbb{R}^n)}$$

Proof. By definition of the cone transform (4.3),

$$
\begin{aligned}
&(C^k f, g)_{L^2_w(Z)} \\
&= \int_Z C^k f(u,\beta,t) g(u,\beta,t) \frac{w(u)}{1-t^2} dt d\beta du \\
&= \int_Z \int_{\mathbb{R}^n} f(x) \delta((x-u)\cdot\beta - |x-u|t) |x-u|^{k-n+2} dx \; g(u,\beta,t) \frac{w(u)}{\sqrt{1-t^2}} dt d\beta du \\
&= \int_{\mathbb{R}^n} f(x) \left(\int_Z g(u,\beta,t) \delta((x-u)\cdot\beta - |x-u|t) \frac{|x-u|^{k-n+2} w(u)}{\sqrt{1-t^2}} dt d\beta du \right) dx \\
&= \int_{\mathbb{R}^n} f(x) \left(\int_Z g(x-y,\beta,t) \delta(y\cdot\beta - |y|t) \frac{|y|^{k-n+2} w(x-y)}{\sqrt{1-t^2}} dt d\beta dy \right) dx \\
&= \int_{\mathbb{R}^n} f(x) C^k_{\#} g(x) dx = (f, C^k_{\#} g)_{L^2(\mathbb{R}^n)}.
\end{aligned}
$$

□

5.4 A Microlocal Property

It is rather standard in tomography to consider the normal operator $C^k_{\#} C^k$, and study its properties.

Theorem 5.4.1. *The normal operator $C^k_{\#} C^k$ is a classical pseudo-differential operator (see e.g., [23, 55]) of order $1-n$,*

$$C^k_{\#} C^k f(x) = \int_{\mathbb{R}^n} \int_{\mathbb{R}^n} e^{i(x-y)\cdot\xi} a(x,y,\xi) f(y) dy d\xi,$$

with an amplitude

$$a(x,y,\xi) = a_0(x,y) |\xi|^{1-n},$$

where

$$a_0(x,y) = 2\int\limits_{\mathbb{R}^n} \frac{|x-y||(x-u)(2u-v)|^{k-n+2}w(u)}{||x-u|(y-u)-|y-u|(x-u)|}du.$$

Proof. We compute the normal operator

$$C_{\#}^k C^k f(x) = \int\limits_{\mathbb{R}^n}\int\limits_{S^{n-1}} C^k f(x-y,\beta,\frac{y}{|y|}\cdot\beta)\frac{|y|^{k-n+2}w(x-y)}{\sqrt{1-\left(\frac{y}{|y|}\cdot\beta\right)^2}}d\beta\frac{dy}{|y|}$$
$$= \int\limits_{\mathbb{R}^n}\int\limits_{S^{n-1}}\int\limits_{\mathbb{R}^n} f(x-y+z)\delta(z\cdot\beta-|z|\frac{y}{|y|}\cdot\beta)|x-y-z|^{k-n+2}dz\ |y|^{k-n+2}w(x-y)d\beta\frac{dy}{|y|}$$
$$= \int\limits_{\mathbb{R}^n}\int\limits_{S^{n-1}}\int\limits_{\mathbb{R}^n} f(x+z-y)\delta((|y|z-|z|y)\cdot\beta)w(x-y)|y(x-y-z)|^{k-n+2}dyd\beta dz,$$

where we have used $\delta(a(x-y)) = \frac{1}{a}\delta(x-y)$.

Now, for fixed $y, z \in \mathbb{R}^n$, $y \neq z$,

$$|y|z-|z|y = \frac{||y|z-|z|y|}{|z-y|}A(z-y)$$

for some the rotation matrix A depending on y and z. Thus,

$$\delta((|y|z-|z|y)\cdot\beta) = \delta(\frac{||y|z-|z|y|}{|z-y|}A(z-y)\cdot\beta) = \frac{|z-y|}{||y|z-|z|y|}\delta((z-y)\cdot A^{-1}\beta).$$

As the Lebesgue measure on S^{n-1} is rotation invariant, we obtain

$$C_{\#}^k C^k f(x) =$$
$$\int\limits_{\mathbb{R}^n}\int\limits_{S^{n-1}}\int\limits_{\mathbb{R}^n} f(x+z-y)\frac{|z-y|}{||y|z-|z|y|}\delta((z-y)\cdot\beta)w(x-y)|y(x-y-z)|^{k-n+2}dyd\beta dz.$$

As $\delta((z-y)\cdot\beta) = \int_{-\infty}^{\infty} e^{-i[(z-y)\cdot\beta]r}dr$, we have

$$\int_{S^{n-1}} \delta((z-y)\cdot\beta)d\beta = \int_{S^{n-1}}\int_{-\infty}^{\infty} e^{-i[(z-y)\cdot\beta]r}drd\beta$$

Letting $\xi = r\beta$ and using rotation invariance of Lebesgue measure, we obtain

$$\int_{S^{n-1}}\int_{-\infty}^{\infty} e^{-i[(z-y)\cdot\beta]r}drd\beta = 2\int_{\mathbb{R}^n} e^{-i(z-y)\cdot\xi}|\xi|^{1-n}d\xi.$$

Therefore,

$$\begin{aligned}
&C^k_{\#}C^k f(x)\\
&= 2\int_{\mathbb{R}^n}\int_{\mathbb{R}^n}\int_{\mathbb{R}^n} e^{-i(z-y)\cdot\xi}f(x+z-y)w(x-y)\frac{|z-y||y(x-y-z)|^{k-n+2}}{||y|z-|z|y|}dydz|\xi|^{1-n}d\xi\\
&= 2\int_{\mathbb{R}^n}\int_{\mathbb{R}^n}\int_{\mathbb{R}^n} e^{i(x-v)\cdot\xi}f(v)\frac{|x-v||y(2(x-y)-v))|^{k-n+2}w(x-y)}{||y|(v-x+y)-|v-x+y|y|}dydv|\xi|^{1-n}d\xi\\
&= 2\int_{\mathbb{R}^n}\int_{\mathbb{R}^n}\int_{\mathbb{R}^n} e^{i(x-v)\cdot\xi}f(v)\frac{|x-v||(x-u)(2u-v)|^{k-n+2}w(u)}{||x-u|(v-u)-|v-u|(x-u)|}dudv|\xi|^{1-n}d\xi,
\end{aligned}$$

where we changed variables in z by letting $v = x+z-y$, and then in y by $u = x-y$. Hence,

$$C^k_{\#}C^k f(x) = \int_{\mathbb{R}^n}\int_{\mathbb{R}^n} e^{i(x-v)\cdot\xi}a_0(x,v)|\xi|^{1-n}f(v)dvd\xi,$$

where

$$a_0(x,v) = 2\int_{\mathbb{R}^n}\frac{|x-v||(x-u)(2u-v)|^{k-n+2}w(u)}{||x-u|(v-u)-|v-u|(x-u)|}du.$$

Finally letting

$$a(x, v, \xi) = a_0(x, v)|\xi|^{1-n}$$

implies the result. □

6. CONCLUSION AND REMARKS

In this dissertation, the (weighted) cone transform was investigated in terms of its invertibility, range conditions and microlocal properties. It was argued that in the case of Compton camera imaging, reducing the set of cones "visible" from a detector (e.g., considering only the cones with a given axial direction), which was done in most previous studies, seems not to be a very good idea (especially in presence of low signal-to-noise ratio), since this amounts to discarding the already collected data while it could be used for stabilizing the reconstruction. We thus considered the full data (weighted) cone transform, and derived various inversion formulas that are applicable for a wide variety of detector geometries in any dimension. We note that it is common to have a variety of different inversion formulas for Radon type transforms, which are all the same for perfect data, but react differently to unavoidable errors in data. Having such a variety is even more important when dealing with overdetermined data, as in Compton camera imaging.

A closely related to the weighted cone transform is what is called weighted divergent beam transform. When the weight factor is not present, this is the well studied and important for the 3D X-ray CT divergent (or cone) beam transform. We thus studied it in some details, derived various inversion formulas and implemented them numerically in dimension three.

One of the most important features, in the author's view, is that the new formulas are adjustable to a wide variety of (detector) geometries. We introduced the class of such geometries satisfying what we call in Chapter 4 the *Tuy's condition* (its weaker form was defined as *Compton admissibility condition* in Chapter 3). Most of the previously derived formulas required very symmetric geometries, allowing for harmonic analysis tools to be used. This is also related to the important issue of understanding the geometries that allow

for (stable) reconstruction. They deserve a much more thorough study, which we plan to address in future work.

As it was mentioned in the introduction, to avoid being distracted from the main purpose of this text, we assumed that the functions to be reconstructed belong to the Schwartz space $\mathcal{S}$. However, as in the case of Radon transform (see, e.g. [36, 46]), the results undoubtedly have a much wider area of applicability, since the derived formulas can be extended by continuity to some wider function spaces. Although we haven't done this in the current text, this conclusion is confirmed, in particular, by our successful numerical implementations for discontinuous (piecewise continuous) phantoms. The issues of appropriate function spaces will be addressed elsewhere.

Practical soundness of the derived inversion techniques is shown by their numerical implementation in the most interesting dimensions two and three. The implementation of the 3D inversion algorithms in Chapter 3 is challenging due to the high dimensionality of the forward data, and the fact that the application of a fourth order differential operator on the unit sphere to a singular integral is required. We thus develop and apply three different inversion algorithms and study their feasibility. One should also notice, that the algorithm of the 3D cone transform inversion in Chapter 4 works much faster than some of the ones developed in Chapter 3. The reason is that a much coarser mesh (1.8K nodes) on the sphere suffices, rather than 30K used in Chapter 3.

REFERENCES

[1] M. ALLMARAS, D. DARROW, Y. HRISTOVA, G. KANSCHAT, AND P. KUCHMENT, *Detecting small low emission radiating sources*, Inverse Problems and Imaging, 7 (2013), pp. 47–79.

[2] G. AMBARTSOUMIAN, *Inversion of the V-line Radon transform in a disc and its applications in imaging*, Computers & Mathematics with Applications, 64 (2012), pp. 260–265.

[3] G. AMBARTSOUMIAN AND S. MOON, *A series formula for inversion of the V-line Radon transform in a disc*, Computers & Mathematics with Applications, 66 (2013), pp. 1567–1572.

[4] G. AMBARTSOUMIAN AND S. ROY, *Numerical inversion of a broken ray transform arising in single scattering optical tomography*, IEEE Transactions on Computational Imaging, 2 (2016), pp. 166–173.

[5] S. R. ARRIDGE, *Optical tomography in medical imaging*, Inverse problems, 15 (1999), p. R41.

[6] R. BASKO, G. L. ZENG, AND G. T. GULLBERG, *Application of spherical harmonics to image reconstruction for the Compton camera*, Physics in Medicine and Biology, 43 (1998), p. 887.

[7] M. BELKIN, J. SUN, AND Y. WANG, *Discrete Laplace operator on meshed surfaces*, in Proceedings of the twenty-fourth annual symposium on computational geometry, ACM, 2008, pp. 278–287.

[8] M. J. CREE AND P. J. BONES, *Towards direct reconstruction from a gamma camera based on Compton scattering*, IEEE transactions on medical imaging, 13 (1994),

pp. 398–407.

[9] D. B. EVERETT, J. S. FLEMING, R. W. TODD, AND J. M. NIGHTINGALE, *Gamma-radiation imaging system based on the Compton effect*, Electrical Engineers, Proceedings of the Institution of, 124 (1977), p. 995.

[10] L. FLORESCU, V. A. MARKEL, AND J. C. SCHOTLAND, *Single-scattering optical tomography: Simultaneous reconstruction of scattering and absorption*, Physical Review E, 81 (2010), p. 016602.

[11] ——, *Inversion formulas for the broken-ray Radon transform*, Inverse Problems, 27 (2011), p. 025002.

[12] L. FLORESCU, J. C. SCHOTLAND, AND V. A. MARKEL, *Single-scattering optical tomography*, Physical Review E, 79 (2009), p. 036607.

[13] P. FUNK, *Über flächen mit lauter geschlossenen geodätischen linien*, Mathematische Annalen, 74 (1913), pp. 278–300.

[14] R. J. GARDNER, *Geometric Tomography*, vol. 6, Cambridge University Press Cambridge, 1995.

[15] I. M. GEL'FAND, S. G. GINDIKIN, AND M. I. GRAEV, *Selected Topics in Integral Geometry*, vol. 220, American Mathematical Soc., 2003.

[16] I. M. GEL'FAND AND A. B. GONCHAROV, *Recovery of a compactly supported function starting from its integrals over lines intersecting a given set of points in space*, in Soviet Math. Dokl, vol. 34, 1987, pp. 373–376.

[17] I. M. GEL'FAND AND G. E. SHILOV, *Generalized Functions, Volume 1: Properties and Operations*, Academic, New York, 1964.

[18] Y. N. GEORGIEVA-HRISTOVA, *Mathematical Problems of Thermoacoustic and Compton Camera Imaging*, PhD thesis, Texas A&M University, 2010.

[19] P. GOODEY AND W. WEIL, *Centrally symmetric convex bodies and the spherical Radon transform*, Journal of Differential Geometry, 35 (1992), pp. 675–688.

[20] R. GOUIA-ZARRAD, *Analytical reconstruction formula for n-dimensional conical Radon transform*, Computers & Mathematics with Applications, 68 (2014), pp. 1016–1023.

[21] R. GOUIA-ZARRAD AND G. AMBARTSOUMIAN, *Exact inversion of the conical Radon transform with a fixed opening angle*, Inverse Problems, 30 (2014), p. 045007.

[22] P. GRANGEAT, *Mathematical framework of cone beam 3D reconstruction via the first derivative of the Radon transform*, in Mathematical methods in tomography, Springer, 1991, pp. 66–97.

[23] A. GRIGIS AND J. SJÖSTRAND, *Microlocal analysis for differential operators: an introduction*, vol. 196, Cambridge University Press, 1994.

[24] M. HALTMEIER, *Exact reconstruction formulas for a Radon transform over cones*, Inverse Problems, 30 (2014), p. 035001.

[25] C. HAMAKER, K. T. SMITH, D. C. SOLMON, AND S. L. WAGNER, *The divergent beam x-ray transform*, Rocky Mt. J. Math., 10 (1980).

[26] S. HELGASON, *Integral Geometry and Radon Transforms*, Springer Science & Business Media, 2010.

[27] Y. HRISTOVA, *Inversion of a V-line transform arising in emission tomography*, Journal of Coupled Systems and Multiscale Dynamics, 3 (2015), pp. 272–277.

[28] M. HUBENTHAL, *The broken ray transform on the square*, Journal of Fourier Analysis and Applications, 20 (2014), pp. 1050–1082.

[29] J. ILMAVIRTA, *Broken ray tomography in the disc*, Inverse Problems, 29 (2013), p. 035008.

[30] C.-Y. JUNG AND S. MOON, *Inversion formulas for cone transforms arising in application of Compton cameras*, Inverse Problems, 31 (2015), p. 015006.

[31] ——, *Exact inversion of the cone transform arising in an application of a Compton camera consisting of line detectors*, SIAM Journal on Imaging Sciences, 9 (2016), pp. 520–536.

[32] A. KATSEVICH, *Theoretically exact filtered backprojection-type inversion algorithm for spiral ct*, SIAM Journal on Applied Mathematics, 62 (2002), pp. 2012–2026.

[33] ——, *An improved exact filtered backprojection algorithm for spiral computed tomography*, Advances in Applied Mathematics, 32 (2004), pp. 681–697.

[34] A. KATSEVICH AND R. KRYLOV, *Broken ray transform: inversion and a range condition*, Inverse Problems, 29 (2013), p. 075008.

[35] R. KRYLOV AND A. KATSEVICH, *Inversion of the broken ray transform in the case of energy-dependent attenuation*, Physics in medicine and biology, 60 (2015), p. 4313.

[36] P. KUCHMENT, *The Radon transform and medical imaging*, vol. 85, SIAM, 2014.

[37] P. KUCHMENT AND F. TERZIOGLU, *Three-dimensional image reconstruction from Compton camera data*, SIAM Journal on Imaging Sciences, 9 (2016), pp. 1708–1725.

[38] ——, *Inversion of weighted divergent beam and cone transforms*, Inverse Problems & Imaging, 11 (2017), pp. 1071–1090.

[39] A. K. LOUIS AND P. MAASS, *A mollifier method for linear operator equations of the first kind*, Inverse problems, 6 (1990), p. 427.

[40] A. K. LOUIS, M. RIPLINGER, M. SPIESS, AND E. SPODAREV, *Inversion algorithms for the spherical Radon and cosine transform*, Inverse Problems, 27 (2011), p. 035015.

[41] R. B. MARR, C.-N. CHEN, AND P. C. LAUTERBUR, *On two approaches to 3d reconstruction in nmr zeugmatography*, in Mathematical aspects of computerized tomography, Springer, 1981, pp. 225–240.

[42] V. MAXIM, *Filtered backprojection reconstruction and redundancy in Compton camera imaging*, IEEE Transactions on Image Processing, 23 (2014), pp. 332–341.

[43] V. MAXIM, M. FRANDEŞ, AND R. PROST, *Analytical inversion of the Compton transform using the full set of available projections*, Inverse Problems, 25 (2009), p. 095001.

[44] M. MORVIDONE, M. K. NGUYEN, T. T. TRUONG, AND H. ZAIDI, *On the V-line Radon transform and its imaging applications*, Journal of Biomedical Imaging, 2010 (2010), p. 11.

[45] C. MÜLLER, *Spherical harmonics*, Springer, 1966.

[46] F. NATTERER, *The mathematics of computerized tomography*, vol. 32, Siam, 1986.

[47] M. K. NGUYEN, T. T. TRUONG, AND P. GRANGEAT, *Radon transforms on a class of cones with fixed axis direction*, Journal of Physics A: Mathematical and General, 38 (2005), p. 8003.

[48] A. OLSON, A. CIABATTI, Y. HRISTOVA, P. KUCHMENT, J. RAGUSA, AND M. ALLMARAS, *Passive detection of small low-emission sources: Two-dimensional numerical case studies*, Nuclear Science and Engineering, 184 (2016), pp. 125–150.

[49] V. PALAMODOV, *Reconstructive integral geometry*, vol. 98, Springer Science & Business Media, 2004.

[50] P.-O. PERSSON AND G. STRANG, *A simple mesh generator in matlab*, SIAM review, 46 (2004), pp. 329–345.

[51] M. RIPLINGER AND M. SPIESS, *Numerical inversion of the spherical Radon transform and the cosine transform using the approximate inverse with a special class of locally supported mollifiers*, Journal of Inverse and Ill-posed Problems, 22 (2014), pp. 497–536.

[52] B. RUBIN, *Introduction to Radon transforms*, vol. 160, Cambridge University Press, 2015.

[53] J. C. SCHOTLAND, *Direct reconstruction methods in optical tomography*, in Mathematical Modeling in Biomedical Imaging II, Springer, 2012, pp. 1–29.

[54] B. SHERSON, *Some Results in Single-Scattering Tomography*, PhD thesis, Oregon State University, 2015.

[55] M. A. SHUBIN AND S. I. ANDERSSON, *Pseudodifferential operators and spectral theory*, vol. 200, Springer, 1987.

[56] M. SINGH, *An electronically collimated gamma camera for single photon emission computed tomography. part i: Theoretical considerations and design criteria*, Medical Physics, 10 (1983), pp. 421–427.

[57] B. SMITH, *Reconstruction methods and completeness conditions for two Compton data models*, JOSA A, 22 (2005), pp. 445–459.

[58] B. D. SMITH, *Image reconstruction from cone-beam projections: necessary and sufficient conditions and reconstruction methods*, IEEE transactions on medical imaging, 4 (1985), pp. 14–25.

[59] E. M. STEIN AND G. WEISS, *Introduction to Fourier analysis on Euclidean spaces*, vol. 32, Princeton university press, 2016.

[60] F. TERZIOGLU, *Some inversion formulas for the cone transform*, Inverse Problems, 31 (2015), p. 115010.

[61] T. T. TRUONG AND M. K. NGUYEN, *On new-line Radon transforms in and their inversion*, Journal of Physics A: Mathematical and Theoretical, 44 (2011), p. 075206.

[62] ——, *New properties of the V-line Radon transform and their imaging applications*, Journal of Physics A: Mathematical and Theoretical, 48 (2015), p. 405204.

[63] H. K. TUY, *An inversion formula for cone-beam reconstruction*, SIAM Journal on Applied Mathematics, 43 (1983), pp. 546–552.

[64] F. WUBBELING AND F. NATTERER, *Mathematical methods in image reconstruction*, SIAM, Philadelphia, 8 (2001), p. 16.

[65] X. XUN, B. MALLICK, R. J. CARROLL, AND P. KUCHMENT, *A Bayesian approach to the detection of small low emission sources*, Inverse problems, 27 (2011), p. 115009.

APPENDIX A

AN ALTERNATIVE PROOF OF THEOREM 3.3.1

Here we prove Theorem 3.3.1 in an alternative way, which avoids reference to the relation (B.31).

As in the case of the Radon transform, invariance properties play a key role in the inversion of the cone transform. In fact, due to rotational invariance, it suffices to prove (3.10) only for the vertical cone transform. Moreover, shift invariance enables us to consider vertical cones having vertex at the origin only, that is $u = 0$.

Proposition A.0.1. *For any $f \in \mathcal{S}(\mathbb{R}^n)$, we have*

$$\int_0^\pi Cf(0, e_n, \psi) \sin\psi d\psi = \frac{\pi}{|\mathbb{S}^{n-1}|} \int_{\mathbb{S}^{n-1}} Rf(\omega, 0)|\omega \cdot e_n| d\omega. \tag{A.1}$$

We first prove the proposition for $n = 2$. By definition of the 2-dimensional cone transform (3.4), we have

$$\begin{aligned}\int_0^\pi Cf(0, e_2, \psi) \sin\psi d\psi = &\int_0^\pi \int_0^\infty f(r\sin\psi, r\cos\psi) \sin\psi dr d\psi \\ &+ \int_0^\pi \int_0^\infty f(-r\sin\psi, r\cos\psi) \sin\psi dr d\psi.\end{aligned}$$

Changing variables by letting $r \to -r$ and $\psi \to \pi - \psi$, respectively, we obtain

$$\begin{aligned}\int_0^\pi \int_0^\infty f(r\sin\psi, r\cos\psi)\sin\psi dr d\psi &= \int_0^\pi \int_{-\infty}^0 f(-r\sin\psi, -r\cos\psi)\sin\psi dr d\psi \\ &= \int_0^\pi \int_{-\infty}^0 f(-r\sin\phi, r\cos\phi)\sin\phi dr d\phi.\end{aligned}$$

Therefore,

$$\begin{aligned}\int_0^\pi Cf(0, e_2, \psi)\sin\psi d\psi &= \int_0^\pi \int_{-\infty}^\infty f(-r\sin\psi, r\cos\psi)\sin\psi dr d\psi \\ &= \int_0^\pi Rf(\omega(\psi), 0)\sin\psi d\psi\end{aligned}$$

where $\omega(\psi) := (\cos\psi, \sin\psi)$. Now, the evenness property of the Radon transform implies that

$$\int_0^\pi Rf(\omega(\psi), 0)\sin\psi d\psi = \int_0^\pi Rf(\omega(\psi+\pi), 0)\sin\psi d\psi = -\int_\pi^{2\pi} Rf(\omega(\phi), 0)\sin\phi d\phi.$$

Hence, we get

$$\int_0^\pi Cf(0, e_2, \psi)\sin\psi d\psi = \frac{1}{2}\int_0^{2\pi} Rf(\omega(\psi), 0)|\sin\psi| d\psi = \frac{1}{2}\int_{\mathbb{S}^1} Rf(\omega, 0)|\omega \cdot e_2| d\omega,$$

which is the equation (A.1) for $n = 2$.

In order to prove the proposition for $n \geq 3$, we need several auxiliary results.

Lemma A.0.2. *For any $f \in \mathcal{S}(\mathbb{R}^n)$, $u \in \mathbb{R}^n$, and $p \in \mathbb{R}$,*

$$\int_{\mathbb{S}^{n-1}} Rf(\omega, p + u \cdot \omega) d\omega = |\mathbb{S}^{n-2}| \int_{\mathbb{S}^{n-1}} \int_{|p|}^{\infty} f(u + r\omega)(r^2 - p^2)^{(n-3)/2} r dr d\omega. \tag{A.2}$$

Proof. Due to the shift invariance of the Radon transform, it suffices to prove the lemma for $u = 0$ only. Let F be the spherical mean-value of f, i.e.,

$$F(r) = \frac{1}{|\mathbb{S}^{n-1}|} \int_{\mathbb{S}^{n-1}} f(r\omega) d\omega.$$

The rotational invariance of the Radon transform implies that it commutes with the spherical mean-value operator. Thus,

$$\hat{F}(p) := RF(\omega, p) = \frac{1}{|\mathbb{S}^{n-1}|} \int_{\mathbb{S}^{n-1}} Rf(\xi, p) d\xi.$$

On the other hand, if $\{\omega, \omega_1^{\perp}, ..., \omega_{n-1}^{\perp}\}$ is an orthonormal system in $\mathbb{R}^n$,

$$\begin{aligned} \hat{F}(p) &= \int_{-\infty}^{\infty} \cdots \int_{-\infty}^{\infty} F(p\omega + t_1\omega_1^{\perp} + \cdots + t_{n-1}\omega_{n-1}^{\perp}) dt_1 ... dt_{n-1} \\ &= \int_{-\infty}^{\infty} \cdots \int_{-\infty}^{\infty} F\left(\sqrt{p^2 + t_1^2 + \cdots t_{n-1}^2}\right) dt_1 ... dt_{n-1} \end{aligned}$$

as F is radial. Letting $x = t_1\omega_1^{\perp} + \cdots + t_{n-1}\omega_{n-1}^{\perp}$, we have

$$\begin{aligned} \int_{-\infty}^{\infty} \cdots \int_{-\infty}^{\infty} F\left(\sqrt{p^2 + t_1^2 + \cdots t_{n-1}^2}\right) dt_1 ... dt_{n-1} &= \int_{\mathbb{R}^{n-1}} F(\sqrt{p^2 + |x|^2}) dx \\ &= |\mathbb{S}^{n-2}| \int_0^{\infty} F(\sqrt{p^2 + t^2}) t^{n-2} dt. \end{aligned}$$

Finally, letting $r = \sqrt{p^2 + t^2}$, we obtain

$$\int_0^\infty F(\sqrt{p^2+t^2})t^{n-2}dt = \int_{|p|}^\infty F(r)(r^2-p^2)^{(n-3)/2}rdr$$
$$= \frac{1}{|\mathbb{S}^{n-1}|}\int_{\mathbb{S}^{n-1}}\int_{|p|}^\infty f(r\omega)(r^2-p^2)^{(n-3)/2}rdrd\omega.$$

Hence, the result follows. □

Corollary A.0.3. *Letting $p = 0$ in* (A.2)*, we obtain*

$$R^\# Rf(u) = \int_{\mathbb{S}^{n-1}} Rf(\omega, u\cdot\omega)d\omega = |\mathbb{S}^{n-2}|\int_{\mathbb{S}^{n-1}}\int_0^\infty f(u+r\omega)r^{n-2}drd\omega$$
$$= |\mathbb{S}^{n-2}|\int_{\mathbb{R}^n} f(u+x)|x|^{-1}dx = |\mathbb{S}^{n-2}|(|x|^{-1} * f)(u). \tag{A.3}$$

(See also [46, Chapter 2, Theorem 1.5].)

Lemma A.0.4. *For $\psi_0 \in (0, \pi/2)$, $\psi \in (0, \pi)$, and $n \geq 3$, we define*

$$g(\psi_0, \psi) = \frac{(\cos^2\psi_0 - \cos^2\psi)^{(n-4)/2}}{(\sin\psi)^{n-3}}. \tag{A.4}$$

Then, for any $f \in \mathcal{S}(\mathbb{R}^n)$,

$$\int_{\psi_0}^{\pi-\psi_0} Cf(0, e_n, \psi)g(\psi_0, \psi)d\psi = \frac{(\cos\psi_0)^{n-3}}{|S^{n-3}|}\int_{\mathbb{S}^{n-2}} Rf((\cos\psi_0)\omega, \sin\psi_0), 0)d\omega. \tag{A.5}$$

Proof. The idea of the proof is to exhaust the exterior volume of two opposite cones having a common vertex in two ways. The first is by taking a family of vertical cones whose vertices are at the origin and opening angles vary from ψ_0 to $\pi - \psi_0$. The second is to consider a family of hyperplanes passing through origin and are tangent to the vertical

cone having vertex at the origin and opening angle ψ_0 (See Fig. A.1).

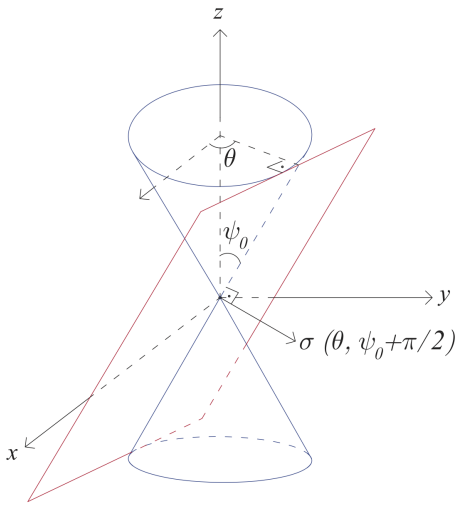

Figure A.1: Geometry of Lemma A.0.4.

Let the functions f and g be given as in the lemma. We can split the integral on the left hand side of equation (A.5) into two parts to get

$$\int_{\psi_0}^{\pi-\psi_0} Cf(0,e_n,\psi)g(\psi_0,\psi)d\psi = \int_{\psi_0}^{\pi/2} Cf(0,e_n,\psi)g(\psi_0,\psi)d\psi + \int_{\pi/2}^{\pi-\psi_0} Cf(0,e_n,\psi)g(\psi_0,\psi)d\psi. \tag{A.6}$$

By the definition of the vertical cone transform (3.3), for the first term on the right

hand side, then

$$\int_{\psi_0}^{\pi/2} Cf(0, e_n, \psi) g(\psi_0, \psi) d\psi$$
$$= \int_{\psi_0}^{\pi/2} \int_{0}^{\infty} \int_{\mathbb{S}^{n-2}} f(\rho(\sin\psi)\omega, \rho\cos\psi)(\rho\sin\psi)^{n-2} g(\psi_0, \psi) d\omega d\rho d\psi.$$

If we make a change of variables in the integral with respect to ρ by letting $z = \rho\cos\psi$, we have

$$\int_{\psi_0}^{\pi/2} Cf(0, e_n, \psi) g(\psi_0, \psi) d\psi$$
$$= \int_{\psi_0}^{\pi/2} \int_{0}^{\infty} \int_{\mathbb{S}^{n-2}} f(z\tan\psi\omega, z)(z\tan\psi)^{n-2} g(\psi_0, \psi) d\omega \frac{dz}{\cos\psi} d\psi.$$

Now, if we let $r = z\tan\psi$, then $dr = z\sec^2\psi d\psi$, and since

$$\cos^2\psi_0 - \cos^2\psi = \frac{\sec^2\psi - \sec^2\psi_0}{\sec^2\psi_0 \sec^2\psi} = \frac{\tan^2\psi - \tan^2\psi_0}{\sec^2\psi_0 \sec^2\psi} = \frac{r^2 - z^2\tan^2\psi_0}{z^2\sec^2\psi_0\sec^2\psi},$$

we have $g(\psi_0, \psi(r, z)) = \dfrac{(r^2 - z^2\tan^2\psi_0)^{(n-4)/2}}{(r\sec\psi_0)^{n-4}}$.

Thus,

$$\int_{\psi_0}^{\pi/2} Cf(0, e_n, \psi) g(\psi_0, \psi) d\psi$$
$$= (\cos\psi_0)^{n-4} \int_{0}^{\infty} \int_{\mathbb{S}^{n-2}} \int_{z\tan\psi_0}^{\infty} f_z(r\omega)(r^2 - z^2\tan^2\psi_0)^{(n-4)/2} r dr d\omega dz.$$

Then, using the identity (A.2), we obtain the following relation between the cone trans-

form of f and $(n-1)$-dimensional Radon transform of f_z.

$$\int_{\psi_0}^{\pi/2} Cf(0,e_n,\psi)g(\psi_0,\psi)d\psi = \frac{(\cos\psi_0)^{n-4}}{|S^{n-3}|}\int_0^{\infty}\int_{\mathbb{S}^{n-2}} Rf_z(\omega,-z\tan\psi_0)d\omega dz$$
$$= \frac{(\cos\psi_0)^{n-4}}{|S^{n-3}|}\int_0^{\infty}\int_{\mathbb{S}^{n-2}}\int_{\mathbb{R}^{n-1}} f_z(\bar{x})\delta(\bar{x}\cdot\omega + z\tan\psi_0)d\bar{x}d\omega dz.$$

Now, since $\delta(\lambda(u-a)) = \lambda^{-1}\delta(u-a)$, we get

$$\int_{\psi_0}^{\pi/2} Cf(0,e_n,\psi)g(\psi_0,\psi)d\psi$$
$$= \frac{(\cos\psi_0)^{n-3}}{|S^{n-3}|}\int_{\mathbb{S}^{n-2}}\int_0^{\infty}\int_{\mathbb{R}^{n-1}} f(\bar{x},z)\delta(\bar{x}\cdot(\cos\psi_0)\omega + z\sin\psi_0)d\bar{x}dzd\omega. \qquad \text{(A.7)}$$

For the second term of the right hand side of (A.6), we change the variable ψ by $\pi-\psi$ to get

$$\int_{\pi/2}^{\pi-\psi_0} Cf(0,e_n,\psi)g(\psi_0,\psi)d\psi = \int_{\psi_0}^{\pi/2} Cf(0,e_n,\pi-\psi)g(\psi_0,\pi-\psi)d\psi$$
$$= \int_{\psi_0}^{\pi/2}\int_0^{\infty}\int_{\mathbb{S}^{n-2}} f(\rho(\sin\psi)\omega,-\rho\cos\psi)(\rho\sin\psi)^{n-2}g(\psi_0,\psi)d\omega d\rho d\psi.$$

Again we change variables first by letting $z = \rho\cos\psi$ and then $r = z\tan\psi$ to obtain

$$\begin{aligned}
&\int_{\pi/2}^{\pi-\psi_0} Cf(0,e_n,\psi)g(\psi_0,\psi)d\psi \\
&\quad = (\cos\psi_0)^{n-4}\int_0^\infty\int_{\mathbb{S}^{n-2}}\int_{z\tan\psi_0}^\infty f_{-z}(r\omega)(r^2 - z^2\tan^2\psi_0)^{(n-4)/2} r dr d\omega dz \\
&\quad = \frac{(\cos\psi_0)^{n-4}}{|S^{n-3}|}\int_0^\infty\int_{\mathbb{S}^{n-2}} Rf_{-z}(\omega, z\tan\psi_0)d\omega dz,
\end{aligned}$$

where the last equality follows from the identity (A.2). Again, by the definition of the Radon transform, and $\delta(\lambda(u-a)) = \lambda^{-1}\delta(u-a)$, we get

$$\begin{aligned}
&\int_0^\infty\int_{\mathbb{S}^{n-2}} Rf_{-z}(\omega, z\tan\psi_0)d\omega dz \\
&\qquad = \cos\psi_0\int_{\mathbb{S}^{n-2}}\int_0^\infty\int_{\mathbb{R}^{n-1}} f(\bar{x},-z)\delta(\bar{x}\cdot(\cos\psi_0)\omega - z\sin\psi_0)d\bar{x}dzd\omega \\
&\qquad = \cos\psi_0\int_{\mathbb{S}^{n-2}}\int_{-\infty}^0\int_{\mathbb{R}^{n-1}} f(\bar{x},z)\delta(\bar{x}\cdot(\cos\psi_0)\omega + z\sin\psi_0)d\bar{x}dzd\omega.
\end{aligned}$$

Thus,

$$\begin{aligned}
&\int_{\pi/2}^{\pi-\psi_0} Cf(0,e_n,\psi)g(\psi_0,\psi)d\psi \\
&\quad = \frac{(\cos\psi_0)^{n-3}}{|S^{n-3}|}\int_{\mathbb{S}^{n-2}}\int_{-\infty}^0\int_{\mathbb{R}^{n-1}} f(\bar{x},z)\delta(\bar{x}\cdot(\cos\psi_0)\omega + z\sin\psi_0)d\bar{x}dzd\omega. \qquad \text{(A.8)}
\end{aligned}$$

Now, using (A.7) and (A.8) for the first and second terms in the equation (A.6), we

obtain

$$\int_{\psi_0}^{\pi-\psi_0} Cf(0, e_n, \psi)g(\psi_0, \psi)d\psi$$
$$= \frac{(\cos\psi_0)^{n-3}}{|S^{n-3}|} \int_{\mathbb{S}^{n-2}} \int_{\mathbb{R}^n} f(x)\delta(x \cdot ((\cos\psi_0)\omega, \sin\psi_0))dxd\omega.$$

Finally, observing that

$$\int_{\mathbb{R}^n} f(x)\delta(x \cdot ((\cos\psi_0)\omega, \sin\psi_0))dx = Rf(((\cos\psi_0)\omega, \sin\psi_0), 0),$$

we have

$$\int_{\psi_0}^{\pi-\psi_0} Cf(0, e_n, \psi)g(\psi_0, \psi)d\psi = \frac{(\cos\psi_0)^{n-3}}{|S^{n-3}|} \int_{\mathbb{S}^{n-2}} Rf((\cos\psi_0)\omega, \sin\psi_0), 0)d\omega.$$

Hence, we get the result. □

Lemma A.0.5. *Assume that $n \geq 3$. Let $g(\psi_0, \psi)$ be given as in* (A.4) *and define*

$$h(\psi_0, \psi) = \frac{(\cos^2\psi_0 - \cos^2\psi)^{(n-2)/2}}{(\sin\psi)^{n-3}}.$$

Then,

$$\frac{d}{d\psi_0} \int_{\psi_0}^{\pi-\psi_0} Cf(0, e_n, \psi)h(\psi_0, \psi)d\psi$$
$$= (2-n)\cos\psi_0 \sin\psi_0 \int_{\psi_0}^{\pi-\psi_0} Cf(0, e_n, \psi)g(\psi_0, \psi)d\psi.$$

Proof. As $\dfrac{\partial h}{\partial \psi_0}(\psi_0, \psi) = (2-n)\cos\psi_0 \sin\psi_0 g(\psi_0, \psi)$, utilizing Leibniz integral rule and noticing that $h(\psi_0, \pi - \psi_0) = h(\psi_0, \psi_0) = 0$ gives the result. □

Proof of Proposition A.0.1, $n \geq 3$. By Lemmas A.0.5 and A.0.4, we have

$$\begin{aligned}
&\frac{d}{d\psi_0} \int_{\psi_0}^{\pi-\psi_0} Cf(0, e_n, \psi) h(\psi_0, \psi) d\psi \\
&\qquad = (2-n)\cos\psi_0 \sin\psi_0 \int_{\psi_0}^{\pi-\psi_0} Cf(0, e_n, \psi) g(\psi_0, \psi) d\psi \\
&\qquad = \frac{(2-n) sin\psi_0 (\cos\psi_0)^{n-2}}{|S^{n-3}|} \int_{\mathbb{S}^{n-2}} Rf(((\cos\psi_0)\omega, \sin\psi_0), 0) d\omega.
\end{aligned}$$

Integrating both sides with respect to ψ_0 from 0 to $\pi/2$, we obtain

$$\begin{aligned}
&\int_0^{\pi} Cf(0, e_n, \psi) \sin\psi d\psi \\
&\quad = \frac{n-2}{|S^{n-3}|} \int_0^{\pi/2} \int_{\mathbb{S}^{n-2}} Rf(((\cos\psi_0)\omega, \sin\psi_0), 0) d\omega \sin\psi_0 (\cos\psi_0)^{n-2} d\psi_0 \qquad \text{(A.9)} \\
&\quad = \frac{n-2}{|S^{n-3}|} \int_0^{\pi/2} \int_{\mathbb{S}^{n-2}} Rf(((\sin\phi)\omega, \cos\phi), 0) \cos\phi (\sin\phi)^{n-2} d\omega d\phi,
\end{aligned}$$

where we changed the variable by letting $\phi = \dfrac{\pi}{2} - \psi_0$. On the other hand, letting $\phi =$

$\psi_0 + \dfrac{\pi}{2}$, we have

$$\begin{aligned}
&\int_0^{\pi} Cf(0, e_n, \psi) \sin\psi d\psi \\
&\qquad = \frac{n-2}{|S^{n-3}|} \int_0^{\pi/2} \int_{\mathbb{S}^{n-2}} Rf(((\cos\psi_0)\omega, \sin\psi_0), 0) d\omega \sin\psi_0 (\cos\psi_0)^{n-2} d\psi_0 \\
&\qquad = \frac{n-2}{|S^{n-3}|} \int_{\pi/2}^{\pi} \int_{\mathbb{S}^{n-2}} Rf(((\sin\phi)\omega, -\cos\phi), 0)(-\cos\phi)(\sin\phi)^{n-2} d\omega d\phi.
\end{aligned}$$

Now, due to evenness of Radon transform, we have

$$\begin{aligned}
Rf(((\sin\phi)\omega, -\cos\phi), 0) &= Rf(((-\sin\phi)(-\omega), -\cos\phi), 0) \\
&= Rf(-((\sin\phi)(-\omega), \cos\phi), 0) = Rf(((\sin\phi)(-\omega), \cos\phi), 0).
\end{aligned}$$

Since the Lebesgue measure is rotation invariant, we obtain

$$\begin{aligned}
&\int_0^{\pi} Cf(0, e_n, \psi) \sin\psi d\psi \\
&\qquad = \frac{n-2}{|S^{n-3}|} \int_{\pi/2}^{\pi} \int_{\mathbb{S}^{n-2}} Rf(((\sin\phi)\omega, \cos\phi), 0)(-\cos\phi)(\sin\phi)^{n-2} d\omega d\phi.
\end{aligned} \tag{A.10}$$

Summing (A.9) and (A.10), we conclude that

$$\begin{aligned}
&\int_0^{\pi} Cf(0, e_n, \psi) \sin\psi d\psi \\
&\qquad = \frac{n-2}{2|S^{n-3}|} \int_0^{\pi} \int_{\mathbb{S}^{n-2}} Rf(((\sin\phi)\omega, \cos\phi), 0) |\cos\phi| (\sin\phi)^{n-2} d\omega d\phi \\
&\qquad = \frac{n-2}{2|S^{n-3}|} \int_{\mathbb{S}^{n-1}} Rf(\sigma, 0) |\sigma \cdot e_n| d\sigma.
\end{aligned}$$

Finally, application of the formula (3.8) and $\Gamma(z+1) = z\Gamma(z)$ gives the result. □

Proof of Theorem 3.3.1. We will use Proposition A.0.1 and the properties of the cone transform to deduce Theorem 3.3.1. We first remind that the Radon transform commutes with shifts and rotations, that is $R(T_u f)(\omega, s) = Rf(\omega, s + \omega \cdot u)$ and $M_A Rf(\omega, s) = Rf(A\omega, s) = R(M_A f)(\omega, s)$.

As cone transform also commutes with shifts, Proposition A.0.1 implies that

$$\begin{aligned}
&\int_0^{\pi} Cf(u, e_n, \psi) \sin\psi d\psi = \int_0^{\pi} C(T_u f)(0, e_n, \psi) \sin\psi d\psi \\
&\quad = \frac{\pi}{|\mathbb{S}^{n-1}|} \int_{\mathbb{S}^{n-1}} R(T_u f)(\omega, 0) |\omega \cdot e_n| d\omega = \frac{\pi}{|\mathbb{S}^{n-1}|} \int_{\mathbb{S}^{n-1}} Rf(\omega, \omega \cdot u) |\omega \cdot e_n| d\omega.
\end{aligned}$$

Next, for $\beta \in \mathbb{S}^{n-1}$, let A be the rotation matrix such that $\beta = Ae_n$ and $x = A^{-1}u$. As cone transform commutes with rotations, we further have

$$\begin{aligned}
\int_0^{\pi} Cf(u, \beta, \psi) \sin\psi d\psi &= \int_0^{\pi} C(M_A f)(x, e_n, \psi) \sin\psi d\psi \\
&= \frac{\pi}{|\mathbb{S}^{n-1}|} \int_{\mathbb{S}^{n-1}} R(M_A f)(\omega, \omega \cdot x) |\omega \cdot e_n| d\omega.
\end{aligned}$$

Due to the rotational invariance of the Radon transform, we have

$$\begin{aligned}\int_{\mathbb{S}^{n-1}} R(M_A f)(\omega, \omega\cdot x)|\omega\cdot e_n|d\omega &= \int_{\mathbb{S}^{n-1}} M_A Rf(\omega,\omega\cdot x)|\omega\cdot e_n|d\omega\\ &= \int_{\mathbb{S}^{n-1}} Rf(A\omega,\omega\cdot x)|\omega\cdot e_n|d\omega = \int_{\mathbb{S}^{n-1}} Rf(A\omega,\omega\cdot A^{-1}u)|\omega\cdot A^{-1}\beta|d\omega\\ &= \int_{\mathbb{S}^{n-1}} Rf(A\omega,A\omega\cdot u)|A\omega\cdot\beta|d\omega = \int_{\mathbb{S}^{n-1}} Rf(\omega,\omega\cdot u)|\omega\cdot\beta|d\omega,\end{aligned}$$

The last equality is due to the rotational invariance of the Lebesgue measure on the sphere.

Hence, we obtain (3.10). □

APPENDIX B

SOME SPECIAL FUNCTIONS, OPERATORS AND INTEGRAL TRANSFORMS

B.1 Special Functions

In this section, we collect some facts about well known special functions, such as the gamma function, Gegenbauer (ultraspherical) polynomials and spherical harmonics. More information can be found in e.g. [45, 52, 59].

B.1.1 The Gamma Function

The gamma function $\Gamma(z)$, $Re\ z > 0$, is defined via an absolutely convergent improper integral:

$$\Gamma(z) = \int_0^\infty x^{z-1} e^x \, dx. \tag{B.1}$$

This integral function is extended by analytic continuation to all complex numbers except the non-positive integers (where the function has simple poles), as a meromorphic function.

The following formulas are known:

$$\Gamma(n) = (n-1)! \quad \text{(n is a positive integer)}, \tag{B.2}$$

$$\Gamma(2z) = \pi^{-1/2} 2^{2z-1} \Gamma(z)\Gamma(z+1/2) \quad \text{(the duplication formula)}, \tag{B.3}$$

$$|\mathbb{S}^{n-1}| = \frac{2\pi^{n/2}}{\Gamma(n/2)} \quad \text{(area formula for the n-sphere).} \tag{B.4}$$

B.1.2 Gegenbauer Poynomials

The Gegenbauer poynomials $P_l^\lambda(t)$, $\lambda \geq -1/2$, of degree l are defined as the orthogonal polynomials on $[-1, 1]$ with weight function $(1-x^2)^{\lambda-1/2}$. They generalize Legendre polynomials and Chebyshev polynomials, and are special cases of Jacobi polynomials. We normalize $P_l^\lambda(t)$ by requiring $P_l^\lambda(1) = 1$. We then have

$$\int_{-1}^{1} P_l^\lambda(t) P_m^\lambda(t)(1-x^2)^{\lambda-1/2}\, dx = \begin{cases} 0, & l \neq m, \\ \dfrac{2^{2\lambda-1}(\Gamma(\lambda+\frac{1}{2}))^2 l!}{(l+\lambda)\Gamma(l+2\lambda)}, & l = m. \end{cases} \tag{B.5}$$

Gegenbauer polynomials are particular solutions of the Gegenbauer differential equation

$$(1-t^2)y'' - (n-1)ty' + l(l+2\lambda)y = 0. \tag{B.6}$$

B.1.3 Spherical Harmonics

A homogeneous polynomial of degree l satisfying the Laplace equation is called a *homogeneous harmonic polynomial* of degree l. A *spherical harmonic* Y_l of degree l is the restriction to $\mathbb{S}^{n-1}$ of a homogeneous harmonic polynomial of degree l on $\mathbb{R}^n$. There are

$$N(n, l) = (n + 2l - 2)\frac{(n+l-3)!}{l!(n-2)!} \tag{B.7}$$

linearly independent spherical harmonics of degree l, and spherical harmonics of different degree are orthogonal on $\mathbb{S}^{n-1}$:

$$\int_{\mathbb{S}^{n-1}} Y_l^m(\omega) Y_k^p(\omega)\, d\omega = \begin{cases} 0, & l \neq k, m \neq p \\ 1, & l = k, m = p. \end{cases} \tag{B.8}$$

The system

$$\{Y_l^m(\omega)\}, \quad l = 0, 1, 2, ..., \quad m = 1, 2, ..., N(n, l)$$

is an orthonormal basis $L^2(\mathbb{S}^{n-1})$. Thus, every integrable function f on $\mathbb{S}^{n-1}$ can be expanded into spherical harmonics:

$$f(\omega) \sim \sum_{l=0}^{\infty} \sum_{m=1}^{N(n,l)} f_{l,m} Y_l^m(\omega) \tag{B.9}$$

where

$$f_{l,m} := (f, Y_l^m) = \int_{\mathbb{S}^{n-1}} f(\omega) Y_l^m(\omega)\, d\omega. \tag{B.10}$$

An important result on spherical harmonics is the Funk-Hecke Formula:

Theorem B.1.1. *Let $f(t)(1-t^2)^{(n-3)/2} \in L^1(-1, 1)$. Then, for every spherical harmonic Y_l of degree l and $\omega \in \mathbb{S}^{n-1}$,*

$$\int_{\mathbb{S}^{n-1}} f(\omega \cdot \sigma) Y_l(\sigma) d\sigma = \lambda_l Y_l(\omega), \tag{B.11}$$

with

$$\lambda_l = |S^{n-2}| \int_{-1}^{1} f(t) P_l^{(n-2)/2}(t)(1-t^2)^{(n-3)/2} dt,$$

where $P_l^{(n-2)/2}(t)$ are the Gegenbauer polynomials.

B.2 The Radon Transform

In this section, we provide the definition, some properties and inversion formulas of the Radon transform. More information can be found in e.g. [26, 36, 46].

The n-dimensional Radon transform R maps a function f on $\mathbb{R}^n$ into the set of its integrals over the hyperplanes of $\mathbb{R}^n$. Namely, if $\omega \in \mathbb{S}^{n-1}$ and $s \in \mathbb{R}$,

$$Rf(\omega, s) = R_\omega f(s) := \int\limits_{x \cdot \omega = s} f(x)dx. \tag{B.12}$$

In this notation, the Radon transform of f is the integral of f over the hyperplane perpendicular to ω at the signed distance s from the origin.

It is immediate from the definition the Radon transform is *even*. That is, for any $\omega \in \mathbb{S}^{n-1}$ and $s \in \mathbb{R}$,

$$Rf(\omega, s) = Rf(-\omega, -s). \tag{B.13}$$

Moreover, it commutes with rigid motions in $\mathbb{R}^n$. Indeed, let T_a be the translation operator in $\mathbb{R}^n$, defined as $T_a f(x) = f(x + a)$ for $a \in \mathbb{R}^n$. We define

$$T_a(Rf)(\omega, s) = Rf(\omega, s + a \cdot \omega).$$

Then,

$$T_a R = R T_a. \tag{B.14}$$

Similarly, let A be an $n \times n$ rotation matrix and $M_A f(x) = f(Ax)$ be the corresponding

rotation operator. We define

$$M_A(Rf)(\omega, s) := Rf(A\omega, s).$$

Then,

$$M_A R = R M_A. \tag{B.15}$$

The Radon transform is invertible on $\mathcal{S}(\mathbb{R}^n)$, namely

$$f = \frac{1}{2}(2\pi)^{1-n} I^{-\alpha} R^{\#} I^{\alpha-n+1} Rf, \qquad \alpha < n. \tag{B.16}$$

Here, $R^{\#}$ is the *backprojection* operator defined as

$$R^{\#} g(x) = \int_{\mathbb{S}^{n-1}} g(\omega, x \cdot \omega) d\omega, \tag{B.17}$$

and I^{α}, $\alpha < n$, is the *Riesz potential* acting on a function $f(u)$ as

$$\widehat{(I^{\alpha} f)}(\xi) = |\xi|^{-\alpha} \hat{f}(\xi),$$

where $\hat{f}$ is the Fourier transform of f. For instance, when n is odd, I^{1-n} is simply the differential operator

$$I^{1-n} = (-\Delta)^{(n-1)/2}$$

with Δ being the Laplacian (see e.g. [15, 26, 46]).

Letting $\alpha = 0$ yields the following version of the Radon inversion formula.

$$f(x) = \frac{(2\pi)^{1-n}}{2} \begin{cases} (-1)^{(n-1)/2} \int\limits_{\mathbb{S}^{n-1}} (Rf)^{(n-1)}(\omega, x \cdot \omega) d\omega, & \text{if } n \text{ is odd,} \\ (-1)^{(n-2)/2} \int\limits_{\mathbb{S}^{n-1}} \mathcal{H}(Rf)^{(n-1)}(\omega, x \cdot \omega) d\omega, & \text{if } n \text{ is even,} \end{cases} \tag{B.18}$$

where $\mathcal{H}$ is the Hilbert transform in $\mathbb{R}$ defined as the principal value integral

$$\mathcal{H}g(t) = \frac{1}{\pi} p.v. \int\limits_{\mathbb{R}} \frac{g(s)}{t-s} ds \tag{B.19}$$

and

$$(Rf)^{(n-1)}(\omega, s) := \frac{\partial^{n-1}}{\partial s^{n-1}} R(\omega, s).$$

B.3 Funk, Sine and Cosine Transforms

In this section, we collect some facts about auxiliary transforms of integral geometry. More information can be found in [52].

Definition B.3.1. Let $f \in C^2(\mathbb{S}^{n-1})$. The Laplace-Beltrami operator Δ_S on $\mathbb{S}^{n-1}$ is defined by

$$(\Delta_S f)(\frac{x}{|x|}) = |x|^2 (\Delta \tilde{f})(x), \tag{B.20}$$

where $\tilde{f}(x) = f(\frac{x}{|x|})$ is the homogeneous extension of f to $\mathbb{R}^n$, and Δ is the Laplace operator on $\mathbb{R}^n$.

The *Funk transform* integrates a function on the sphere over all great circles (hyperplane sections). The formal definition is given below.

Definition B.3.2. The *Funk transform* of a function $f \in C(\mathbb{S}^{n-1})$ is defined by

$$Ff(\theta) = \int\limits_{\mathbb{S}^{n-1}\cap\theta^{\perp}} f(\sigma)d_{\theta}\sigma = \int\limits_{\{\sigma\in\mathbb{S}^{n-1}:d(\sigma,\theta)=\pi/2\}} f(\sigma)d_{\theta}\sigma. \tag{B.21}$$

Here, $d(\sigma,\theta) = arccos(\sigma\cdot\theta)$ is the geodesic distance between the points σ and θ in $\mathbb{S}^{n-1}$, and $d_{\theta}\sigma$ stands for the $O(n)$-invariant probability measure on the $(n-2)$-dimensional sphere $\mathbb{S}^{n-1}\cap\theta^{\perp}$.

Several inversion formulas for the Funk transform exist in the literature [13, 15, 26, 49, 52]. We use the following inversion formula.

Theorem B.3.3 ([52]). *Let $g = Ff$, $f \in C^{\infty}_{even}(\mathbb{S}^{n-1})$, $n \geq 3$. If n is even, then*

$$f = cP(\Delta_S)Fg, \qquad c = \frac{\sqrt{\pi}}{\Gamma^2((n-1)/2)}, \tag{B.22}$$

where

$$P(\Delta_S) = 4^{1-n/2}\prod_{k=0}^{n/2-2}\left[-\Delta_S + (2k+1)(n-3-2k)\right]. \tag{B.23}$$

If n is odd, then

$$f(\omega) = Q(\Delta_S)\left\{\frac{2^{n-2}\Gamma(\frac{n}{2})}{(n-2)!\pi^{n/2}}\int\limits_{\mathbb{S}^{n-1}} g(\sigma)\log\frac{1}{|\omega\cdot\sigma|}d\sigma\right\} + \frac{\Gamma(\frac{n}{2})}{2\pi^{n/2}}\int\limits_{\mathbb{S}^{n-1}} g(\sigma)d\sigma, \tag{B.24}$$

where

$$Q(\Delta_S) = 4^{(1-n)/2}\prod_{k=0}^{(n-3)/2}\left[-\Delta_S + (2k+1)(n-3-2k)\right]. \tag{B.25}$$

Definition B.3.4. The *cosine transform* of a function $f \in C(\mathbb{S}^{n-1})$ is defined by

$$\mathfrak{C}f(\omega) = \frac{1}{|\mathbb{S}^{n-1}|} \int\limits_{\mathbb{S}^{n-1}} f(\sigma)|\sigma \cdot \omega| d\sigma, \tag{B.26}$$

for all $\omega \in \mathbb{S}^{n-1}$.

The cosine transform is a continuous bijection of $C^{\infty}_{even}(\mathbb{S}^{n-1})$ to itself (see e.g. [14], [52]).

Theorem B.3.5. *[52] Let $g = \mathfrak{C}f$, $f \in C^{\infty}_{even}(\mathbb{S}^{n-1})$. Then, if n is odd,*

$$f(\omega) = P_r(\Delta_S) \left\{ \frac{-2\pi^{(2-n)/2}}{\Gamma(\frac{n}{2})} \int\limits_{\mathbb{S}^{n-1}} g(\sigma) \log \frac{1}{|\omega \cdot \sigma|} d\sigma \right\} + \frac{\Gamma(\frac{n+1}{2})}{\pi^{(n-1)/2}} \int\limits_{\mathbb{S}^{n-1}} g(\sigma) d\sigma, \tag{B.27}$$

with $r = (n+1)/2$, and if n is even,

$$f = cP_r(\Delta_S)Fg, \qquad c = -\frac{\pi 2^{n-1}}{\Gamma(n-1)}, \tag{B.28}$$

with $r = n/2$, where F is the Funk transform and

$$P_r(\Delta_S) = 4^{-r} \prod_{k=0}^{r-1} \left[-\Delta_S + (2k-1)(n-1-2k) \right].$$

The following identity (see [19]) provides a relation between the cosine and Funk transforms.

$$(\Delta_S + n - 1)\mathfrak{C} = F, \tag{B.29}$$

Definition B.3.6. The *sine transform* of a function $f \in C(\mathbb{S}^{n-1})$ is defined by

$$\mathcal{S}f(\omega) = \frac{1}{|\mathbb{S}^{n-1}|} \int\limits_{\mathbb{S}^{n-1}} f(\sigma)(1 - |\sigma \cdot \omega|^2)^{1/2} d\sigma, \tag{B.30}$$

for all $\omega \in \mathbb{S}^{n-1}$.

It is known that (see [52, p. 284, (5.1.17)]),

$$\mathcal{S} = \frac{\pi}{|\mathbb{S}^{n-1}|}\mathfrak{C}F. \tag{B.31}$$